MCDONNELL DOUGLAS
CORPORATION

NASA CR-135004
LMSC-D521581

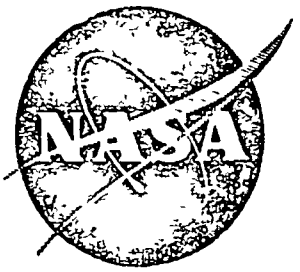

NUMERICAL SIMULATION OF LOW GRAVITY DRAINING

by

G. D. Bizzell and G. E. Crane

LOCKHEED MISSILES & SPACE COMPANY, INC.

Prepared for

NATIONAL AERONAUTICS AND SPACE ADMINISTRATION

NASA Lewis Research Center

Contract NAS3-17798

1 Report No	2. Government Accession No	3 Recipient's Catalog No
NASA CR-135004		

4 Title and Subtitle	5 Report Date
NUMERICAL SIMULATION OF LOW GRAVITY DRAINING	May 1976
	6. Performing Organization Code

7. Author(s)	8. Performing Organization Report No.
G. D. Bizzell and G. E. Crane	LMSC-D521581
	10 Work Unit No

9 Performing Organization Name and Address	11 Contract or Grant No.
Lockheed Missiles and Space Co., Inc. P. O. Box 504 Sunnyvale, CA 94088	NAS3-17798
	13 Type of Report and Period Covered
12 Sponsoring Agency Name and Address	Contractor Report
National Aeronautics and Space Administration Washington, D.C. 20546	14. Sponsoring Agency Code

15 Supplementary Notes

Project Manager, E. P. Symons, Chemical Energy Division,
NASA Lewis Research Center, Cleveland, Ohio 44135

16. Abstract

Assuming that the liquid is inviscid and incompressible, that its motion is irrotational and axisymmetric, and that its solid-liquid contact angle is constant (5^{o}), the initial boundary-value problem is solved numerically. Excessive mesh distortion encountered with strictly Lagrangian or Eulerian kinematics is avoided by introducing an auxiliary kinematic velocity field along the free surface to vary the trajectories used in integrating the ordinary differential equations simulating the moving boundary. The computation of the velocity potential is based upon a nonuniform triangular mesh which is automatically revised to varying depths to accommodate the motion of the free surface. These devices permit calculating draining induced axisymmetric slosh through the many (or fractional) finite amplitude oscillations that may occur depending upon the balance of draining, gravitational, and surface tension forces. Velocity fields, evolution of the free surface with time, and liquid residual volumes are computed for three and one half decades of Weber number and for two Bond numbers, tank fill levels, and drain radii. Comparisons with experimental data are very satisfactory.

17 Key Words (Suggested by Author(s))	18 Distribution Statement
Fluid mechanics Low gravity draining Moving boundary problems Initial boundary value problems	Unclassified-unlimited

19 Security Classif (of this report)	20 Security Classif (of this page)	21 No of Pages	22 Price*
Unclassified	Unclassified		$3.00

* For sale by the National Technical Information Service Springfield Virginia 22151

FOREWORD

This final report, prepared by the Lockheed Missiles and Space Company for the National Aeronautics and Space Administration-Lewis Research Center, documents the technical effort for Contract NAS3-17798, "Numerical Simulation of Low Gravity Draining." (The Contract started on Oct. 9, 1973 and was completed on May 10, 1976.) Mr. E. P. Symons was the NASA Project Manager.

The authors wish to thank Mr. Symons for support throughout the study and, in particular, for supplying Lewis Research Center experimental data for comparison with our analytical and numerical results.

The present study is a continuation of an earlier study, "Low Gravity Draining from Hemispherically Bottomed Cylindrical Tanks," performed by P. Concus, H. M. Satterlee and the authors under Contract NAS3-11526. The problem formulation section of that study, reported in reference 1, is essentially reproduced herein. The authors acknowledge, therefore, the previous contributions of Drs. Concus and Satterlee.

TABLE OF CONTENTS

ABSTRACT

Assuming that the liquid is inviscid and incompressible, that its motion is irrotational and axisymmetric, and that its solid-liquid contact angle is constant (5°), the initial boundary-value problem is solved numerically. Excessive mesh distortion encountered with strictly Lagrangian or Eulerian kinematics is avoided by introducing an auxiliary kinematic velocity field along the free surface to vary the trajectories used in integrating the ordinary differential equations simulating the moving boundary. The computation of the velocity potential is based on a nonuniform triangular mesh, which is automatically revised to varying depths to accommodate the motion of the free surface. These devices permit calculating draining induced axisymmetric slosh through the many (or fractional) finite amplitude oscillations that may occur depending upon the balance of draining, gravitational, and surface tension forces. Velocity fields, evolution of the free surface with time, and liquid residual volumes are computed for three and one half decades of Weber number and for two Bond numbers, tank fill levels, and drain radii. Comparisons with experimental data are very satisfactory.

SUMMARY

The problem is to simulate low gravity draining from a hemispherically bottomed tank over as wide a range of parameters as possible and to compute the residual volume at vapor ingestion (the entrance of the free surface into the drain). Fourteen simulations are presented covering the contractual nondimensional data ranges: two drain radii, 1/30 and 1/10 of a tank radius; two initial volumes, $5\pi/3$ and $8\pi/3$; two Bond numbers (ratio of gravitational to surface tension forces), B=0 and 5; and three and one half decades in Weber number (ratio of draining to surface tension forces), W=.01 through 50. The range in Weber number extends that of experiment by two decades. Simulation agrees very well with experiment; application of qualitative results from this study explains both areas of excellent agreement and regions of divergence in two comparisons with experiments performed at NASA-Lewis Research Center.

Results include plots, in a form suitable for use in design studies, of residual volume and vapor ingestion time against W and W/(1+B), a simple correlation parameter occurring in the transformation between nondimensional time scales for draining and sloshing problems. The S-shape of the residual volume plots is indicative of three draining regimes: (i) a capillary regime with low Weber numbers, low residuals, and many waves having small amplitude; (ii) a draining dominated regime with high Weber numbers, large residuals, and a fractional wave in which much liquid is dynamically trapped on the wall as the center is rapidly withdrawn; and (iii) a transition regime with few waves of large amplitude which may become very irregular in zero gravity. Increasing the Bond number may (i) increase the number of waves and decrease their amplitude, (ii) change the motion from draining dominated to oscillatory, or (iii) reduce the amount of liquid trapped on the wall. Drain radius affects residual volume for $W << 1$ or, at a fixed W, for $B >> 1$. Increasing initial volume when wave motion occurs gives more waves of the same nature; however, increasing it in the draining dominated regime gives gravitational and capillary forces more time, before vapor ingestion, to drain the liquid trapped against the wall into the bulk flow. In a simulation for B=5, W=10, and initial volume $8\pi/3$, the liquid trapped on the wall evolved into a thin wall sheet with the flow rate down the wall less than that in the bulk flow. The program terminated because the separation into two flows had not been anticipated. There may be problems near the boundary of the draining regime for which the validity of the inviscid model may be questioned. However, in a survey program it is appropriate.

The model is based upon the irrotational flow of an incompressible, inviscid fluid. The model assumes that the liquid is initially at rest, includes the static and dynamic effects of surface tension with the solid-liquid contact angle taken as constant (here 5°), retains the nonlinear convective terms in the differential equations derived from the Bernoulli equation, and assumes that, after impulsive opening of the drain, the outflow rate is uniform and constant across the orifice. The mixed initial boundary-value problem resulting from the nondimensionalization and specialization of the model to axisymmetric motion in a hemispherically bottomed circular cylindrical tank is reformulated as an initial value problem for three ordinary differential equations for the coordinates and velocity potential at a point on the moving boundary with the connection to the drain given by the solution of Laplace's equation within the liquid. The reformulation shows that almost all the action in the problem is at the free surface, a fact which motivates the method of numerical solution and the form of the graphical presentation of the data.

A significant result is the demonstration that the method of moving triangular meshes supplemented by the method of variable trajectories, is a practical and economic way to solve this difficult moving boundary problem. A finite difference analog of Laplace's equation is solved on a nonuniform triangular mesh which is revised as needed, deeper and deeper into the liquid, in response to the changing shape of the free surface. Mesh rows are dropped to accommodate outflow. Parts of mesh columns are dropped or added in response to changing thickness of the wall sheet. The method of variable trajectories was developed specifically for this study to deal with the mesh difficulties encountered as the free surface stretches and contracts when either Lagrangian or Eulerian kinematics are used. A small auxiliary kinematic velocity directed along the free surface and chosen to maintain a desired mesh distribution is added to the Lagrangian velocity components at each time step; the differential equation for the velocity potential is appropriately modified to account for the change in direction.

INTRODUCTION

This analytical and numerical study of low gravity draining from hemispherically bottomed, cylindrical tanks is a continuation of an earlier study [1]. The mathematical formulation of the problem, the basic approach to its numerical solution, and much of the computer programming are carried over from the previous to the present work. Successful simulations were obtained in the former for small and moderate fill levels for Weber number one and greater, which, at that time, corresponded to values obtainable in the short draining time available within the period of weightlessness provided by the 2.2- and the 5- to 10-second Zero-Gravity Facility at NASA Lewis Research Center [2-5]. Comparisons of the computed and experimental data available led to the conclusion that a model based upon the irrotational motion of an incompressible, inviscid fluid satisfactorily describes the fluid dynamics of low gravity draining. The model assumes the liquid is initially at rest; includes the static and dynamic effects of surface tension with the solid-liquid contact angle taken as constant (here 5°); and retains the nonlinear convective terms. The drain rate is taken as constant and uniform across the orifice. The mixed initial-boundary value problem resulting from the specialization to axisymmetric motion in a hemispherically bottomed, cylindrical tank is detailed in the next section, which is essentially the nondimensional problem formulation of the previous report repeated for convenience and completeness (cf. Figure 1).

The fundamental goal of the present study was to simulate low gravity draining over as wide a range of parameters as possible to determine residual volume as a function of Weber number, Bond number, fill level, and drain radius. Particular emphasis was directed toward developing the program of the previous study in three areas: low Weber number cases, where draining induced wave motion predominates; high Weber number cases, where development of a sheet along the wall is the dominant feature; and high fill level cases, which require long-time simulation. Only those changes in the numerical scheme or its implementation that directly contribute to achiev-

ing this goal have been made. Details are given in the subsequent section, Numerical Analysis; however, some are sketched here.

Both Eulerian and Lagrangian kinematics on the free surface failed in the previous study by producing large mesh spacings near the wall when a wall sheet developed; and the latter also failed by pushing mesh points too near the axis, thereby exciting instabilities inherent in the singularity of the coordinate system along the axis. To eliminate these difficulties, an auxiliary kinematic velocity directed along the free surface is used to vary the trajectories of the mesh points on the free surface so that the ratio between adjacent mesh intervals remains nearly constant. The Bernoulli equation is modified to accommodate the change in the direction of integration. This method of variable trajectories includes both the Eulerian and the Lagrangian formulation of the problem. The latter was introduced for low gravity reorientation by Moore and Perko [6].

The method of moving triangular meshes, carried over from the previous program, is now capable of carrying a low Weber number problem through many waves and of generating satisfactory meshes for more than 7800 time steps (cf. Figures 2 and 3). It also handles the development and thinning of a wall sheet adequately. The method of truncated direct solution for determining the velocity potential and the representation of the free surface by cubic spline interpolation are carried over from the previous work.

The behavior of the streamlines with time reflects the fact that almost all the action is at the free surface. Well up into the tank, they are fixed; as they approach the free surface, they begin to vibrate; and they reach their maximum amplitude at the free surface. Thus the trajectories of the points in which the free surface meets a fixed set of streamlines is a natural way to present their behavior with time. Moreover, these points are easily determined in the course of computing the normal derivative.

Computer plots are a large part of the report (cf. Figures 4-17): for each case there is a figure with the time history of the free surface and the associated velocity field presented on facing pages. On the first page successive positions of the free surface are shown. The eleven lines cross-

ing the free surfaces are the trajectories of the points in which the free surface meets a fixed set of streamlines (.02, .1, .2, ..., .8, .9, .98). The reader is cautioned that these trajectories are not streamlines. The trajectories do reveal the changes in motion that are taking place underneath the rather smoothly falling free surface. When compared case to case, they show how features of the low gravity draining phenomenon vary with parameter changes. Moreover, the trajectories can be used, with caution, to make statements about the nature of the flow. For example, the central trajectory divides the free surface into two parts, a central disk and an outer annulus, each of which furnishes one half of the flow out the drain. When the central trajectory is far to the right of its nominal position (r=.707...), the average velocity in the outer annulus must exceed that in the central disk. Because the draining free surface is generally lower at the center than at the wall, when a streamline end is moving to the right, a velocity component is probably developing down the free surface; when it is moving to the left, the component along the free surface is being choked off. Examples of streamline plots are included in many figures to illustrate specific points and to provide the reader with a way to check his use of these trajectories. Time histories of the centerline and wall points on the free surface are given on the second page of each figure. A free surface of interest can be associated with a time (or vice versa) by using the height at the centerline or wall as a common entry in the graphs on the facing pages.

The simulations complement the experimental work in low gravity draining at Lewis Research Center [2-5]. Agreement between experiment and simulation is remarkably good in one case with both parameters and initial conditions nearly identical (cf. Figure 18) and is acceptable in another case even though the experimental measurements at the wall are in doubt (cf. Figure 19). The simulations seem to have shorter draining times and, therefore, higher residuals than expected from experiment. Two explanations are proposed. The experimental technique may produce an initial velocity distribution that gives longer draining times than the zero initial velocity distribution of the simulations. The five degree contact angle condition assumed in the simulation may retain enough liquid high up near the wall to account for the discrepancy.

Both hypotheses can be tested numerically; it is possible to materially reduce the contact angle and to simulate one or more full drop tower runs. Five of the fourteen simulations are for Weber numbers .01 and .1 which extend data two orders of magnitude below the experimental range with conservative residuals.

It would be surprising if some evidence of waves did not appear on the wall sheets; Figure 13 (c) and (d) shows such a case. In general these are suppressed by the large mesh spacing used on the free surface. In one long-time simulation a wall sheet develops, begins to fall, thins out, and then begins to neck off when it is nearly a tank radius long and several hundredths of a radius thick. Figure 16 shows this development in detail and the final pages of the figure show a remarkable example of automatic generation of a mesh. This suggests that there may be combinations of Bond number, Weber number, and fill level for which liquid may be trapped on the wall. Further investigation is needed. The fourteen simulations provide information about the fluid dynamics that is difficult to measure or observe in tests and thereby give a basis for developing a qualitative explanation for low gravity draining phenomena.

Computed values of residual volume and vapor ingestion time are given in Table I for the fourteen combinations of Weber number, Bond number, drain size, and initial filling. These data are also plotted as functions of the Weber and Bond number in Figures 21-23. Periods of draining induced waves observed to exist during the draining simulations are presented in Figure 24.

The program for simulating low gravity draining uses two new numerical methods that were developed specifically for it, namely, the method of variable trajectories and the method of moving triangular meshes. It has the property that most of the computation takes place at the free surface. Because cubic spline interpolation is used, few points are needed on the free surface. Although the free surface may more than double its length, no more than twenty-six points have been used. Computing times have varied from twenty minutes to an hour and three quarters, the latter including nearly 8000 time steps, some rerunning, and sixteen oscillations. With additional work, the computing time can be reduced, by perhaps twenty percent.

With little modification the program could simulate the effect of throttling [7] and with some changes the effect of outlet baffles [8] on low gravity draining at lower Weber numbers than can be achieved experimentally. An extension of the idea behind the method of truncated solutions can be used as a basis for three-dimensional draining problems with off-center drains. The program is also adaptable to computing simulations of axisymmetric, surface tension dominated reorientation problems. The methods can be generalized to deal with the inviscid rotational approximation to the Navier-Stokes equations expressed in terms of stream function and vorticity, which is applicable when the vorticity is produced outside the domain and merely conserved within. The methods can also be used for the full axisymmetric Navier-Stokes equations.

The low gravity draining program and its generalizations appear to have the same capabilities as the Marker and Cell family of programs [9]. The distinction between the ranges of applicability lies in the philosophy behind each. The present program is based in classical continuum mechanics with classical mathematical techniques adapted for computer usage and achieves its results with extensive computation on few points. The Marker and Cell family is based upon doing a moderate amount of computation to imitate the physics in each cell and doing this for many cells and time steps. So long as the boundary holds together, or the domain breaks into large pieces, the family derived from the present program probably has an advantage; when the boundary decomposes irregularly, the advantage is to Marker and Cell.

The numerical simulation program and the results obtained from it have interest beyond the field of low gravity draining. The demonstration that the combination of the methods of variable trajectories, truncated direct solution, and moving triangular meshes can solve very difficult moving boundary problems over a wide range of parameters is a significant result to mathematicians interested in moving boundary problems.

PROBLEM FORMULATION

In this section the mathematical formulation of the draining problem is presented. All the variables that appear are dimensionless, unless otherwise designated, and they are defined in the Symbol List, Appendix A, where the relationships to the physical dimensioned variables are given.

Initial Configuration

Consider an axisymmetric vertical container consisting of a right circular cylinder with a hemispherical bottom that has an orifice of circular cross-section centered on the axis (see Figure 1(a)). Let the container be so oriented that the gravitational field is directed parallel to the axis. Prior to the initiation of draining at time $t = 0$, it is assumed that there is sufficient liquid in the container to cover the orifice and that the liquid is at rest.

The equilibrium free surface of the liquid is found by solving the two-point boundary value problem

$$\frac{1}{r}\frac{d}{dr}\left[\frac{r\,dF/dr}{(1+(dF/dr)^2)^{1/2}}\right] - B(F - h_c) = 2H_o, \quad 0 < r < r_w \tag{1}$$

with

$$\frac{dF}{dr} = 0 \qquad \text{at} \quad r = 0 \tag{2}$$

and

$$\left[\frac{dF/dr}{(1+(dF/dr)^2)^{1/2}}\right] = r\cos\Theta - (1-r)^{1/2}\sin\Theta \tag{3}$$

at $r = r_w$

Equation (1) is the requirement that the static liquid pressure at the free surface be in equilibrium with the constant ullage pressure there; (2) is the condition arising from the symmetry of the container; and (3) is the requirement that the free surface meet the container with contact angle Θ. (Computations are carried out in this study for the case where Θ has the value 5^o). Circular cylindrical coordinates are used with origin at the

center of the orifice, and the Bond number B is chosen to be positive when gravity acts vertically downward (see Figure 1(a)).

The volume of the liquid within the tank is

$$V = 2\pi \int_0^{r_w} r\, f(r)\, dr - V_s \tag{4}$$

where, for an orifice of radius r_o,

$$V_s = \frac{\pi}{2} f_w \left(r_w^2 - r_o^2 - 2f_w^2/3\right)$$

is the volume between the hemispherical bottom of the tank and a right circular cylinder of radius r_w with bottom touching the orifice (see Figure 1(b)). By specifying, along with (1), (2), and (3), the initial volume V_o, the height $F(r)$ of the initial equilibrium free surface is determined (and hence the values of h_c, the height of the surface at its center, H_o, the mean curvature there, and r_w, the value of r where the free surface intersects the wall).

Draining

Dynamic Equations. At time $t = 0$, it is assumed that draining is initiated by pumping the fluid out in such a manner that the outflow velocity is directed vertically downward and is uniform over the orifice. This outflow velocity is attained instantaneously and remains constant until the time that the free surface first begins to enter the orifice. It is further assumed that the liquid is incompressible and inviscid and that vortexing and turbulence are absent so that the motion can be taken to be irrotational. In actual practice the effect of a small nonzero viscosity is evidenced by a layer of liquid that remains on the container wall during draining, but such a layer is generally thin enough for problems of interest here that it may be neglected.

Under the above assumptions, one is led to the following initial boundary-value problem for axisymmetric motion from $t = 0$ until free surface

breakthrough.

Velocity Potential. The sign of the velocity potential φ is chosen so that the velocity is given by $\underline{v} = \underline{\nabla}\varphi$. The velocity potential satisfies Laplace's equation,

$$\frac{1}{r}\frac{\partial}{\partial r}\left(r\frac{\partial \varphi}{\partial r}\right) + \frac{\partial^2 \varphi}{\partial z^2} = 0 \tag{5}$$

in the liquid.

Boundary Conditions. The conditions on φ over the fixed portion of the boundary are that on the symmetry axis and container wall the normal velocity be zero

$$\frac{\partial \varphi}{\partial n} = 0 \qquad \text{on} \quad r = 0 \quad \text{and on the wall} \tag{6}$$

and at the orifice the outward-directed normal velocity be $1/r_o^2$

$$\frac{\partial \varphi}{\partial n} = \frac{1}{r_o^2} \qquad \text{for} \quad z = 0,\ 0 < r < r_o \tag{7}$$

On the instantaneous free surface, one has the kinematic condition, which can be expressed either in the form

$$\frac{\partial f}{\partial t} = \frac{\partial \varphi}{\partial z} - \frac{\partial \varphi}{\partial r}\frac{\partial f}{\partial r} \tag{8a}$$

or

$$\frac{dR}{dt} = \frac{\partial \varphi}{\partial r}, \qquad \frac{dZ}{dt} = \frac{\partial \varphi}{\partial z} \tag{8b}$$

and the Bernoulli equation, which can be expressed as either

$$W\frac{\partial \varphi}{\partial t} = 2H - Bf - \frac{W}{2}\left|\underline{\nabla}\varphi\right|^2 + C(t) \tag{9a}$$

or

$$W \frac{d\varphi}{dt} = 2H - BZ + \frac{W}{2} |\underline{\nabla} \varphi|^2 + C(t) \qquad (9b)$$

where

$$2H \equiv \frac{1}{r} \frac{\partial}{\partial r} \left[\frac{r \, \partial f/\partial r}{(1 + (\partial f/\partial r)^2)^{1/2}} \right]$$

is twice the mean curvature of the free surface, $z = f(r,t)$. The first forms (8a) and (9a) are written in Eulerian (partial time derivative) form for points $z = f(r,t)$ on a single valued free surface, whereas the second forms (8b) and (9b) are written in Lagrangian (total time derivative) form for points $r = R(t)$, $z = Z(t)$ on a free surface which may be multiply-valued (with 2H appropriately expressed). The first forms follow the motion of the free surface along fixed values of r, whereas the second follow the actual motion of points on the surface.

The choice of the particular function of integration $C(t)$ that, from theoretical considerations, is the most convenient to use in (9a) and (9b) is the one corresponding to φ being independent of time when the velocity at the free surface is uniform and directed vertically downward. For this case of stationary flow, we have that $\varphi = \text{const.} - z$ near the free surface and $f(r,t) = F(r) - t$, so that setting $\partial\varphi/\partial t = 0$ in (9a) yields, with the use of (1), for $C(t)$ the value,

$$C(t) = -Bt + W/2 - (2H_o - Bh_c) \qquad (10)$$

Finally, the end condition for (9a) and (9b), that the contact angle remain fixed during the motion at its equilibrium value Θ, is

$$\frac{\partial f/\partial r}{(1 + (\partial f/\partial r)^2)^{1/2}} = r \cos \Theta - (1 - r^2)^{1/2} \sin \Theta \quad \text{at} \quad r = r_w \qquad (11)$$

Initial Conditions. Equations (5) - (11) are to be solved subject to the initial conditions at $t = 0$ that the free surface is the equilibrium shape $z = F(r)$ and that the velocity potential is the solution of (5), (6), (7), and the condition that the potential vanish on the free surface,

$$\varphi = 0 \qquad \text{on } z = F(r) \tag{12}$$

That the free surface is initially an equipotential can be observed by examining the nature of the discontinuity in the Bernoulli equation (9) at $t = 0$ [10]. Take $C(t)$ equal to $-2H_o + Bh_c$ for $t < 0$ and the value given by (10) for $t \geq 0$; then (9) holds for non-positive as well as for positive t with $\varphi \equiv$ const. for $t < 0$. The right-hand side is piecewise continuous with a step discontinuity at $t = 0$ corresponding to the instantaneous change of velocity. Thus the time derivative of φ at the free surface has only a step discontinuity at $t = 0$, and hence φ itself must be continuous there at $t = 0$ and equal to the same constant value it had for $t < 0$. The continuity of φ on the free surface at $t = 0$ corresponds to the condition that the external ullage pressure remain fixed there as draining is initiated [11].

NUMERICAL ANALYSIS

This section begins with a summary of the numerical scheme used for simulating low gravity draining. After reading the first paragraphs in this part, the reader interested in the physical results of this study may jump to the fourth part, which discusses the interpretation of data. The formal details of the new methods are covered in the second part. The third part describes some technical details of the program and includes, retrospectively, sketches of changes that would make the program even more successful. New problems that have arisen through the development of the program and through the consideration of its extension to other applications in low gravity fluid dynamics are also described.

Numerical Scheme

Reformulation of the Mathematical Problem. With the free surface boundary conditions expressed in Lagrangian form, the mixed initial-boundary value problem becomes three sets of ordinary differential equations (8b, 9b) connected by the solution to a mixed boundary value problem (5), (6), and (7), for the velocity potential within the fluid, a domain with a moving boundary. Two of the sets of ordinary differential equations (8b) describe the motion of particles lying on the meridian of the free surface; the third set (9b) describes the change in velocity potential with time along the particle trajectories. Thus the mixed boundary value problem for the velocity potential has given but changing boundary values on the free surface and, with constant drain rate, time-independent normal derivative conditions on the remainder of the boundary (cf. Figure 1). This restatement of the mathematical problem was introduced by Moore and Perko [6, p. 307] in studying reorientation in low gravity.

The restatement implies that almost all the action is at the free surface in the following precise sense. The data at a point on the free surface needed to integrate the ordinary differential equations are the coordinates, the curvature and slope of the meridian, and the velocity potential and its derivatives, tangential and normal; of these only the last requires informa-

tion not on the free surface, and that only in a neighborhood of it. In the nondimensionalization the tank radius is taken as the characteristic length and the characteristic time is chosen so that the nondimensional outflow velocity integrates to π over the drain. Hence equal volumes leave the tank in equal times; and the drain radius remains as a geometric parameter controlling the shape of the flow through the drain. The dimensional outflow rate (and any variation in it) appear in the Weber number, which occurs only at the free surface in the ordinary differential equation for the change of velocity potential with time. (Were the drain rate to vary, the transformation back to dimensional time would vary too.) The mixed boundary value problem has two functions; it transfers information along the free surface and it carries the residual geometric information left after nondimensionalization up to the free surface.

When the fluid is at rest, the initial shape is determined by balance of gravitational and surface tension forces, including the contact angle condition, and the free surface is initially an equipotential, which may be taken as zero. The computational realization of the restated problem has three parts: first, choosing a discrete set of points on the initial free surface as initial conditions from <u>each</u> of which to integrate numerically three ordinary differential equations; second, integrating the equations; and third, at each time step approximating the normal derivative of the velocity potential at the free surface by finding the potential along a line near and "parallel" to the free surface. A cubic spline interpolation gives a numerical representation of the free surface.

<u>The Method of Truncated Direct Solution</u>. The statement, <u>almost all the action is at the free surface</u>, can be taken over to the discrete problem as <u>most of the computation is near the free surface</u> by taking advantage of the properties of the direct block factorization method [12, pp. 52-61] applied to the finite difference equations representing the mixed boundary value problem for the velocity potential. As yet only two restrictions on mesh and finite difference method are needed: first, that the mesh points can be arranged in lines (with those adjacent to the free surface roughly parallel to it), and second, that at each point the finite difference equation in-

volves only points on a few adjacent lines. With these restrictions, the totality of finite difference equations for the velocity potential can be arranged as a matrix equation in block form by lines with the blocks for the line adjacent to the free surface last. When a set of mesh lines adjacent to the free surface is changed, the last block rows (with difference equations involving points in the changed rows) change too. However, because the boundary conditions, except on the free surface, are independent of time, the bulk of the matrix does not change; so the direct matrix does not change; so the direct matrix factorization down to the first changed block row can be saved, reused, and the process restarted there. Furthermore, because only the potential on the line adjacent to the free surface is needed to approximate the normal derivative, the solution may, in general, be truncated after this line. If the vertical mesh spacing is wide enough near the free surface, the moving boundary will not come near the mesh line below it in a time step. Hence in the next time step only the last block row in the matrix equation need be recomputed and refactorized.

Generation of Moving Triangular Meshes. As the simulation continues, it is necessary to revise the mesh lines to accommodate the changing shape of the free surface and the outflow of liquid. Change of shape is accommodated by revising the mesh progressively deeper and deeper into the tank; outflow is dealt with by removing a line from the mesh near the free surface.
To facilitate approximating boundary conditions along curved boundaries, an irregular triangular mesh is used. Along the free surface two mesh triangles meet at the axial point, three meet at a general point, and there is one mesh triangle in the contact angle, in the interior of the liquid, six mesh triangles meet at a mesh point. With these restrictions, a triangular mesh filling the half-axial cross section of the liquid is topologically equivalent to a polygonal domain composed of equilateral triangles, with the image of the free surface being a straight line (cf. Figure 2). The mesh lines within the liquid are the images of the lines parallel to the image of the free surface in the polygonal domain. The generation of the triangular mesh, both initially and in revision, is accomplished by adapting a triangular mesh generator developed at Lawrence Radiation Laboratory, Livermore,

California [13, p. 168] in which only the location of the boundary points need be prescribed.

Finite Difference Equations. Each triangle in the mesh is subdivided into three quadrilaterals bounded by segments of the perpendicular bisectors of the sides when the triangle is acute and by segments of the medians when the triangle is obtuse. Thus each mesh point is surrounded by a polygonal area formed by as many quadrilaterals as there are triangles meeting at the mesh point. The union of these polygonal areas fills the half-axial cross section of the liquid. The finite difference approximation at each mesh point is obtained by integrating the Laplace equation over the mesh region generated by rotating the polygonal area surrounding the mesh point about the axis of symmetry. On one hand, this volume integral vanishes; on the other, it is equal to the integral of the normal derivative of the velocity potential over the bounding surfaces. The normal derivative is approximated by the finite difference quotient between adjacent mesh points, unless it is given by a boundary condition. Thus each finite difference equation involves points on at most three lines. The areas of the bounding surfaces are sums of areas of the frustums of cones generated by the sides of mesh regions. This procedure gives the finite difference equations the weights appropriate to the axial symmetry of the problem while retaining the advantage of calculating mainly in two dimensions. Additional details are given throughout [1] and in [13, p. 151; 14, pp. 181-194].

Computation of the Derivatives. For calculating the curvature and slope of the free surface meridian, its two coordinates are interpolated by cubic splines in chord length along the polygonal free surface. These interpolants have end values implied by the fixed contact angle and the symmetry at the center, pass through the computed values, and have continuous first and second derivatives [15, p. 51]. This permits accurate calculation of the curvature from few mesh points on the free surface and accurate rotation of the normal and tangential derivatives into the derivatives in the coordinate directions. The tangential derivative of the velocity potential is determined from a similar cubic spline interpolation; the end conditions are the zero derivative implied by symmetry at the center and a cubic extrapolation

of the derivative to the wall. At each mesh point on the free surface, the integral of the normal derivative over the bounding surfaces of the corresponding mesh region must vanish. Solving the resulting finite difference approximation for the unknown normal derivative gives the latter as a linear combination of five values of the velocity potential, three on the free surface and two on the mesh line below. Because the contact point must be constrained to move along the wall, its velocity is taken as the derivative of the velocity potential along the chord of the wall.

Normalization of the Potential and Integration. For some cases, particularly those with low Weber number, the potential may become very flat near the contact point. To minimize the loss of significance in forming differences, the arbitrary function of time, $C(t)$, in the Bernoulli equation, (9a) or (9b), is chosen so that throughout the computation the velocity potential is zero at the contact point. Because the derivative of the velocity potential must vanish there, $C(t)$ is the negative of the other terms in the differential equation for the change of velocity potential at the contact point. When the contact point lies on the hemisphere, it is returned to the hemisphere by projection from its center at the end of each time step. The trapezoidal rule is used for the numerical integration of the ordinary differential equations. Time steps are varied slowly, in geometric progressions with ratios near one; the user prescribes the interval for which each ratio holds.

The Auxiliary Potential. The scheme for simulation so far described still has an unresolved numerical and programming problem. Relative to the mesh that is adequate at the free surface and throughout the tank, a fine mesh is needed to compute the flow into the drain. To get reasonable residuals, the free surface must approach, if not enter, this region of fine mesh. Thus it appears that mesh points should be periodically added to the free surface without introducing unwanted oscillations thereon. To avoid this problem, which is probably lengthy but not insoluable, an auxiliary potential is introduced to satisfy the inhomogeneous boundary condition on the velocity potential at the drain. The auxiliary potential is that of the same liquid draining at the same rate from a circumscribing, flat-bottomed, semi-infinite, circular,

cylindrical tank through a circular, axial drain of the same size (cf. Figure 1). When the potential is represented as the sum of the auxiliary potential and a residual potential, the latter satisfies a mixed boundary value problem which has boundary conditions identical in form to those for the full velocity potential except that the normal derivative vanishes in the drain and is a nonzero function on the circular part of the tank meridian. This function represents the negative of the flow into and out of the corner of the cylinder cut off by the tank meridian; it is continuous and slowly varying and matches the zero normal derivatives it meets at its end points. Hence it places no undue restriction on the mesh. Introducing the auxiliary potential transfers the major part of the flow geometry at the drain to the free surface. In spite of its drawbacks, extra computing time and extreme difficulty in evaluating near the drain, the introduction of the auxiliary potential was the key that made possible the realization of the numerical scheme just described in the previous study. The auxiliary potential has been carried over to the present study.

The Method of Variable Trajectories. Adding a small auxiliary velocity to the tangential velocity on the free surface meridian and leaving the normal velocity unchanged result in a small first-order displacement of the computational point along the free surface at the new time step. Repeatedly doing so gives variable integration trajectories. Because the axis and the wall are fixed trajectories, the auxiliary velocity must be restricted to vanish on these lines. Choosing the auxiliary velocity identically zero gives the Lagrangian formulation of the problem; choosing it so that the trajectories lie along the radial coordinate lines results in the Eulerian formulation. Because the free surface stretches and contracts nonuniformly and contains a fixed number of mesh points, the rule used for choosing the auxiliary velocity is one that maintains the ratio between adjacent mesh intervals nearly constant. The differential equation for the change in velocity is simply the total derivative with respect to time along the trajectory, which can be computed from the Bernoulli equation (9a), the sum of the tangential and the auxiliary velocity, and the normal velocity. The introduction of variable trajectories prevents the growth of large mesh spacings during the development of a wall sheet and the movement of mesh points too close to the axis.

The Method of Moving Triangular Meshes. The distance between two mesh lines is directly available only at the centerline and the wall; however, because it is the altitude of mesh triangles touching the two mesh lines, it can be inferred from the area of the triangles, which is always available in the calculation. Mesh triangles touching the free surface are divided into four groups of contiguous triangles, upper and lower bounds for the areas within each group are calculated at each mesh revision, and these bounds are extended to test bounds by multiplying by fractions near one, which may vary from group to group. At each subsequent time step the areas of triangles touching the free surface are tested against group bounds. When the area of a triangle falls outside the test bounds, rezoning is initiated. Thus rezoning takes place when the distance between the free surface and the adjacent mesh line becomes too small or too large. When wave motion is strong, rezoning may be initiated from any group; when a wall sheet is developing, generally it is from the center line group.

The first rezoning is a minor one involving three rows of mesh triangles adjacent to the free surface. At the first minor rezoning, test bounds similar to those used at the free surface are set up for the lowest row. When minor rezoning is again required, the areas in the lowest row are checked against the test bounds. Failure indicates that some part of the top three rows has been compressed (or dilated) to the point where readjustment of the mesh over more rows is necessary. A major rezoning over five or six mesh rows from the top frequently suffices. Again the first time a major rezoning occurs, test bounds are set up for the lowest row of triangles and the sequence of minor rezoning tests is restarted. At the next major rezoning, the areas of the lowest row of triangles are tested against the test bounds. Failure requires a general rezoning deeper into the tank. The test for determining when rezoning is necessary is carried over from the previous study; the analogous tests for determining whether the bottom line of a mesh revision are satisfactory are new. Their failure is a prediction that further rezoning will soon be required and an indication that an immediate rezoning will save time.

The mesh generator requires that the mesh points on the boundary of the region to be rezoned be prescribed. Because the mesh points on the free surface and

lowest mesh line are fixed, the rezoning input reduces to specifying the mesh points on the axis and wall within the region to be rezoned. To insure that the mesh varies smoothly, particularly near the free surface, these points are distributed in geometric progressions whose ratios are determined by the number of intervals, the initial interval, and the length of the rezoning interval. At the wall the first interval is set by making the triangle at the contact point isosceles; at the axis it is a fraction of the adjacent mesh spacing at the free surface.

Before anything else is done, at any stage of rezoning, these ratios are computed and tested against input test bounds which may differ at the wall and the axis and usually become more stringent as rezoning progresses from minor to major to general rezoning. Failure to pass the test bounds is cause to progress to the next stage. Passing the test bounds for minor and major rezonings invokes the area tests described above. In the general case two more mesh rows are rezoned after a failure. After successive failures to satisfy the test bounds, a mesh line is dropped between the free surface and the current fixed mesh line. When the general rezoning reaches the bottom of the tank, the final mesh row is adjusted, if necessary, to meet the ratio requirements along the wall, all switches are reset to restart the rezoning process from the beginning, and the entire mesh is rezoned. Figure 3 shows selections from the sequence of meshes generated for an oscillatory problem.

The rezoning procedure just described is satisfactory so long as a marked wall sheet does not develop. When the fourth mesh point on the free surface, counting the contact point as the first, moves toward the wall across a test bound, .958 has been used, programming is invoked which removes all but the top four triangles in the right-hand diagonal column from the logical diagram and the corresponding partial column from the physical mesh (cf. Figure 2). When the next point on the free surface moves across the test bound toward the wall, the next diagonal column is dropped, except for the top four triangles. The dropping continues so long as mesh points on the free surface cross the test bound. Of course, there is also programming to restore these columns to the mesh as mesh points cross the test bound moving away from the wall. Thus the logical diagram for a developing wall sheet is the union of two parallelo-

grams having a common left boundary with the wider just below the free surface containing two rows of triangles. Mesh points on the right and lower boundaries of the logical diagram map into the tank meridian in the physical mesh. The radial coordinate of the points which lie on the exterior boundary of the top parallelogram is one; their vertical coordinates are the height at the free surface of the corresponding points on the free surface counting from the contact point. The last mesh interval so determined plays the role of the side of the isosceles triangle as the first mesh interval in generating subsequent rezoning boundary points along the wall.

The number of mesh intervals remaining on the right edge of the logical diagram is known. The length of the interval to be filled with a geometric sequence of mesh intervals is determined by assigning the physical mesh point corresponding to the lower right corner of the old logical diagram to the same corner in the new one. Along the arc corresponding to the bottom of the logical diagram, less the intervals mapping into the drain, mesh points are distributed uniformly. Along the axis mesh points are distributed uniformly between free surface and drain to complete the specification of boundary points necessary for a complete rezoning.

As the wall sheet develops, the center falls and mesh lines are dropped. Hence with few mesh lines, the ratio of the geometric sequence along the wall increases and may exceed the upper bound prescribed for a general rezoning. When this occurs, another mesh interval is added on the wall by dropping part of another diagonal mesh column. The lower part of the right boundary of the logical diagram is moved one mesh interval to the left, leaving six mesh triangles unchanged. The logical diagram is now a union of three parallelograms growing wider toward the free surface. The heights of mesh points on the wall that correspond to the exterior boundaries of the top two parallelograms are obtained by projecting the height of the free surface at the corresponding point counting from the contact point along both edges. Mesh intervals between boundary points corresponding to the lower exterior edges of the top parallelograms are extra mesh intervals on the wall, in that they do not correspond to mesh intervals at the axis. The length of the last extra mesh interval is again used as first interval in the geometric sequence below. Complete rezoning as described in the previous paragraph takes place.

The program permits adding extra intervals of either kind as needed. Figure 2 shows a physical mesh and the corresponding logical diagram with seven extra mesh intervals, four generated by motion of mesh points toward the wall and three required to keep the mesh intervals along the wall from becoming too large.

Extra mesh intervals generated by the motion of points on the free surface are retained so long as they lie completely on the vertical tank wall and the corresponding point on the free surface lies to the right of the test bound. When the latter condition fails, for one or more points, the corresponding intervals are removed and the outer boundary of the logical diagram below the second row is moved to the right. When any extra interval begins to escape from the tank wall, it is removed and the corresponding mesh column is completely restored to the logical diagram and the physical mesh. On the occasion of the addition or deletion of an extra mesh interval along the wall, the entire mesh is revised.

Computational Normalizations and Checks. In the program the definitions of the volume, the rate of flow out the drain, and the streamfunction are divided by π. With this modification the streamfunction varies between 0 at the wall and -1 at the axis (or 0 at the axis and 1 at the wall, if the other direction of integration is chosen). Thus the streamlines can be naturally labeled so that a given streamline is the trace in the half-axial cross section of the curved cylinder enclosing the given fraction of the flow out the drain. This labeling facilitates interpreting the plots showing trajectories of streamline ends at the free surface. Another consequence of the renormalization is that the modified rate of flow out the drain is unity and the total modified outflow in a given time is equal to the time. Thus the principle that the sum of the volume in the tank and the volume that has left the tank should equal the original volume translates to the statement that the computed volume plus the time should equal the initial computed volume. Volumes are computed from the cubic spline representation of the meridian of the free surface by Lobatto quadrature of order six.

The value of the streamfunction at the axis is printed at each time step. A drift away or a jump from a very good approximation to -1 indicates diffi-

culty with the mesh or with the computation of the auxiliary potential. As an over-all check of the accuracy of the computation, the sum of the time and the volume is printed at each time step.

Small Amplitude Waves. Because there is no requirement that the free surface be single valued, the method of variable trajectories shares with the Lagrangian formulation the ability to detect waves of small amplitude, particularly along a wall sheet, provided that the mesh spacing is fine enough. (This does occur in Figure 13(c) and (d).) However, using a small mesh not only materially increases computing time but also may lead to computational instabilities that defeat the goal of determining the over-all behavior of low gravity draining.

New Methods

The Method of Variable Trajectories. Here the formal details of the method are given (its use as part of the numerical scheme is described above under the same heading). Throughout the computation, a local coordinate system is used at the free surface. The exterior normal and the tangent vector directed toward the axis are the local unit vectors. The method of variable trajectories moves points on the free surface by adding to the tangential velocity a small incremental velocity, u, also directed along the free surface. For the current problem the function u is required to vanish at the axis and the wall. The equations for the evolution of the free surface, the analogs of the kinematic equations (8b), take the simple form

$$N_t = \varphi_n \quad \text{and} \quad S_t = \varphi_s + u \tag{13}$$

with N(t) and S(t) representing position in local coordinates. The corresponding equation for the evolution of the potential is the total derivative of the potential along the variable trajectory,

$$W \frac{d\varphi}{dt} = 2H - BZ + \frac{W}{2} |\underline{\nabla} \varphi|^2 + u \varphi_s + C(t) \tag{14}$$

where $$2H = (Z_{ss}R_s - Z_s R_{ss}) + Z_s/R \tag{15}$$

is the mean curvature of the free surface [16, pp. 7, 11]. The transformation of (13) from the local coordinates to the global cylindrical coordinates

is accomplished by a rotation through the angle, - arctan (Z_s/R_s), followed by a reflection in the r-coordinate line through the point, which occurs because the tangent vector is directed away from the axis in the global system. The resulting computational equations for the evolution of the free surface

$$\begin{aligned} R_t &= -\varphi_n Z_s - (\varphi_s + u) R_s \\ Z_t &= \varphi_n R_s - (\varphi_s + u) Z_s \end{aligned} \tag{16}$$

differ from their Lagrangian counterparts only in the incremental velocity. Aside from the choice of u, only one multiplication and two additions are added by (14) and (16) at each point. These equations are used in both the predictor and corrector steps of the modified Euler method.

The point obtained by applying only the second equation in (13) over a finite time interval does not lie on the free surface. This observation suggests that a second order auxiliary velocity, based upon the curvature of the free surface (the term in parenthesis on the right of (15)), could be added to the normal velocity to give a second order correction to the trajectories. Although the information needed is available, the first order modification proved adequate for the present applications.

The goal of the choice of u is to maintain the ratio of adjacent mesh intervals in the neighborhood of a fixed input value. Because the number of intervals in the geometric sequence is given, the size of the initial interval varies in response to the stretching and contracting of the free surface. From this information, a geometric sequence of points with the given ratio between adjacent intervals is determined. The difference in chord length along the free surface between the actual mesh point and the corresponding member of the desired geometric sequence is reduced to the velocity, u, by dividing by five times the current time step. The multiplier five, which is arbitrary, and the further restriction that the magnitude of u not exceed that of the tangential velocity are devices, adopted in lieu of a more complicated rule for determining u, to insure that the trajectories near the wall remain within the tank. These modifications are appropriate because continued progress toward the goal is what is needed. In comparison with its effect, the additional work in determining this u is modest; five addi-

tions and four multiplications per point plus the evaluation of a logarithm and an exponential and some overhead are needed.

Experience gained in this study suggests that replacing the auxiliary potential by a finite difference approximation throughout the tank, with many mesh lines running into the drain, may be feasible. In this case mesh points would have to be added to the free surface as it approached the drain. The method of variable trajectories, with an appropriate choice of u, could be used to spread mesh points apart in anticipation of adding a point or points in regions where unwanted instabilities would not develop.

The Method of Moving Triangular Meshes. The application of the method as part of the numerical scheme is described above under the same heading; here further details and some of the underlying principles are discussed. A nonuniform triangular mesh in which six mesh triangles meet in an interior point can be deformed into a regular triangular mesh with a polygonal boundary, the corresponding logical diagram. Frequently, the discussion of the structure, generation, movement, and change of a nonuniform triangular mesh becomes simpler in terms of its logical diagram.

For programming purposes, the polygon in the logical domain should be the union of simple geometric figures composed of mesh triangles, such as triangles, parallelograms, and trapezoids. And it should have a connected interior. The mesh triangles within the polygon between two adjacent mesh lines form a mesh row. The programming is simpler when all the mesh rows in at least one of the three directions are simply connected. At the cost of extra space and some programming, multiply connected domains can be handled with existing coding. For numerical reasons, the mesh generator mapping the logical into the physical mesh should require minimal input, vary the interior mesh smoothly when the mesh on the boundary is smooth, and produce interior triangles that are as nearly regular as possible. The last requirement is to insure that no direction is slighted in the flow of information within the mesh. Obvious violations of these requirements occur in the present study in the neighborhood of the wall sheet and above the drain. Experience has shown that when the free surface is close to the drain,

too little mesh in the vertical direction either produces an oscillation or enlarges a real one. Further numerical experiment with a finer vertical mesh is needed to determine the nature of this oscillation.

In the physical mesh, the free surface is a distinguished curve along which it is desired to keep the mesh structure as uniform as possible. Thus the same number of mesh triangles should meet at each mesh point. Hence the image of this curve in the logical diagram should be a straight line. The method of variable trajectories is designed to enforce a measure of regularity with a fixed number of mesh points, even when the free surface is stretching and contracting. The succession of minor, major, and general rezonings are devices to restore uniformity near the free surface with a minimum of work. Stability of the normal derivative on the free surface at the axis is a continuing problem. Two devices have minimized this problem; first, the number of rows in a minor rezoning was increased from two to three, and second, the axial mesh spacing was made uniform. In major and general rezonings, the aim is to relax the compression and dilation near the free surface progressively further into the mesh. Uniformity along the axis near the free surface is achieved by requiring that the ratio between successive axial mesh intervals be near one for a major rezoning and even nearer for a general rezoning.

In changing the logical diagram to accommodate the development of the wall sheet, the changes were made as far away from the moving boundary as appeared practical. Experience shows that reliable results can be obtained with quite irregular meshes far from the free surface. More mesh points on the free surface are desirable near a base of the thinning wall sheet. In this area there may be an abrupt transition very near the free surface between long thin triangles in the sheet and the fat triangles in the body of the liquid (cf. Figure 16(f)). It would be useful to know under what conditions the cubic spline interpolation could be used to readjust and add mesh points along the free surface without triggering computational instabilities.

The method of moving triangular meshes appears to be applicable to a number of moving boundary problems. Among those in low gravity fluid dynamics are

the investigation of the effect of baffles in the bottom of the tank and various aspects of reorientation including the generation and dissipation of eddies and geysers.

Details of the Program

Only the aspects of the program relevant to the understanding of the present simulations are discussed here. Material not covered here or in the earlier parts of this report is unchanged from [1]. After a description of the present organization, a few specific details are given in the order that they occur in the first pass through the program.

Organization. The program is a special purpose code for numerical simulation of low gravity draining; the experimental nature of the problem requires a highly modular design for ease in modification. Thus the program can be easily adapted for related problems in low gravity fluid dynamics. In complexity it is comparable with members of the Marker and Cell family and with large structural dynamics codes, although it uses only 56,000 words of core storage. It generates six files on auxiliary disk storage, one containing restart points, two for intermediate output, and three for storage of output for future processing, plotting, summary listing, etc. It is designed for a time-sharing computer system which, in the main, charges for the number of operations performed and for the product of the amount of core memory used times the time it is occupied. Therefore, overlays are used insofar as possible; and subcollections are used, with the dimensions of arrays and buffers set only in the final collection of the absolute program.

Generation of the Free Surface. For Bond number 0, an arc of a circle making the given contact angle can be used as an initial free surface meridian for experiments with contact angles less than 5°. To go to contact angle zero would probably require an analytic expression as a patch at the contact point. For higher Bond numbers, the program for integrating (1), (2), and (3) should be revised for smaller contact angles or for fill levels intersecting the wall within the hemisphere. An interesting and perhaps more instructive alternate would be to by pass the generation by simulating a full experimental run including the reorientation phase.

Initial and Restart Input. Two forms of restart are available. One continues with the mesh from the previous part of the run; the other permits the user to improve the mesh. In both cases all control parameters may be modified.

Matrix Generation. Were a reorientation phase to precede the draining phase, the change would come here. At the instant the drain opened, there would be a switch from the zero normal derivative conditions along the entire tank wall and in the drain to the nonzero conditions along the hemisphere representing the residual influence of the auxiliary potential. The impulsive velocity resulting from the opening of the drain would be added to the existing velocity.

Matrix Factorization. The chief reason for using few mesh points is the rapid increase with the number of points of computer time used in matrix factorization together with the solution of the lower triangular system of equations. These two subroutines generally use more computer time than any other part of the program. These routines deal with block-tridiagonal matrices having diagonal blocks of varying size. Inner products are computed in double precision and truncated to single precision to strike a balance between accuracy and storage.

Auxiliary Potential. For purposes of numerical computation, it is convenient to introduce the residual velocity potential φ_2,

$$\varphi_2 = \varphi - \varphi_1 \tag{17}$$

where φ_1 is the auxiliary potential corresponding to the draining problem in a full infinitely-tall cylinder having a flat, rather than hemispherical, bottom. This, in essence, transfers the nonhomogeneous boundary condition on φ at the orifice to one on φ_2 at the free surface, thus obviating the need for an accurate numerical solution near the drain. The potential φ_1 can be expressed as the infinite series

$$\varphi_1 = c - z + \frac{2}{r_o} \sum_{m=1}^{\infty} \frac{J_1(j_{1,m}\, r_o)}{[j_{1,m}\, J_0(j_{1,m})]^2}\, J_0(j_{1,m}\, r)\, \exp(-j_{1,m}\, z) \qquad (18)$$

where J_0 and J_1 are Bessel functions of the first kind and $j_{1,m}$ is the m-th zero of the latter (taking $j_{1,0} = 0$). For computational convenience the additive constant c is initially chosen so that $\varphi_1 = 0$ at the intersection of the equilibrium free surface and the container wall. Substitution of $\varphi_1 + \varphi_2$ for φ into the draining equations yields the desired problem with φ_2, which does not vary rapidly near the orifice, as the unknown. (See Figure 1(b)).

Whenever the mesh is completely rezoned, the additive constant c is redefined so that the auxiliary potential vanishes at the contact point. High in the tank, where z is large, the convergence of the series (18) is enforced by the rapid decrease of the exponential factor. As z decreases, the convergence becomes slower and slower; and the computation of the auxiliary potential becomes a dominant factor in the computing time for low Weber numbers. At the high Weber numbers used in the previous study, the draining time is so short that this fact was obscured. An improved method of calculating the auxiliary potential is needed. A more rewarding alternate would be to eliminate the auxiliary potential altogether. For details of the present calculation see [1, pp. 19-21].

Treatment of the Contact Point. Because the contact point must be constrained to move along the wall, its velocity is taken to be the difference quotient of the potential at the contact point and the mesh point just below on the wall. This choice is consistent with the calculation of the normal derivative at other points on the free surface. It also enforces on the vertical wall the boundary condition that the normal derivative of the potential vanish and provides a reasonable approximation to this condition on the curved wall. The value of 2H used in (14) is computed at the contact point just as at any other point. The condition that the contact angle remain fixed appears in the calculation as an end condition for the cubic spline interpolation. This is the only place where the contact angle condition occurs in the body of the

program. The successful computation with a very thin wall sheet suggests that a smaller contact angle may be feasible. The extrapolated value of the tangential derivative at the contact point is used in the calculation only as an end condition for the cubic spline interpolation. All values used at the contact point can be viewed as interior limits along the free surface or wall.

Integration Control. To achieve stability in a wide range of situations, the modified Euler method is used for the integration of the differential equations for the location of the free surface and the potential thereon. The dependent variables are carried in double precision and the derivatives in single precision. Time steps are taken in geometric series with the ratios and times of ratio change under user control. What is needed here, as in many other problems, is a simple and effective method for automatic time step control for low order methods where the first neglected term may not adequately represent the error.

Mesh Control. One of the achievements of this study is to have demonstrated that the method of moving triangular meshes can be made to work effectively. The controls have already been described in the two preceding parts of this section with the method.

Use of Plots and Data

Plots. Streamline plots presented in this report are truncated after the data for the first ten mesh rows below the free surface has been plotted. As the previous study showed that the streamlines in the middle and bottom of the tank remain fixed [1, pp. 63, 67, 95], continuing the plots beyond the truncation would waste computer time in redetermining information available on plots produced later in the run. Because the integral of the nondimensional outflow velocity over the drain is normalized in the computation to the value +1, the normalized streamfunction varies between 0 and -1 when the direction of integration is from wall to axis. With this normalization the streamlines can be labeled so that -.5 streamline is the trace (in the half-axial cross section of the tank) of the curved circular cylinder that instantaneously separates the flow through the tank and out the drain into two equal

PAGES MISSING FROM AVAILABLE VERSION

using the height at the centerline or wall as a common entry in the two graphs. The columns on the left, headed STEP and TIME, give the time-step number and the time for each free surface included in the plot. Alternate entries in the columns are offset as an aid in counting. Within a simulation run, the time step may vary and the number of time steps between free surface output may either change or be offset at a restart. The free surfaces presented here are an automatic selection from the original data chosen to give readability on a single page; consequently, intervals in step number and time in the lists may be unequal.

In the labels on computer plots, the symbol C1 means Case 1; B and W have their usual meaning; VOL is the nondimensional volume divided by π; and DR stands for the nondimensional drain radius. Labels similar to those on the free surface plots appear at the top of the mesh plots with the corresponding values at the bottom. Small circles at the center of a triangle indicate that it is obtuse (an obtuse triangle at the intersection of the axis with the drain is a digital artifact produced by roundoff).

Termination. In Table I, Summary of Computed Data, the values are from the printed computer listing of the last completed time step. For later simulations, the run was stopped when the free surface fell below .06 at the axis; some of the earlier simulations were terminated higher in the tank when it was clear that a restart would run for only a few more time steps and produce no significant change in the values. The data files (now on magnetic tape) may contain a free surface position from the predictor half of the next time step. This predicted information appears as the last point of the time histories of the centerline and wall heights. An χ on these plots marks the time when the predicted free surface jumped from above .06 to below the orifice of the drain. If the predicted free surface survives the automatic selection process, it gives a linear interpolation of the mesh points on the free surface. The streamline end trajectories are computed and plotted for those time steps at which a complete free surface is not output. As vapor ingestion develops, the trajectories become separate dots near the axis. The dots are computed from the cubic spline interpolation of the free surface and therefore should be connected by a smooth curve perpendicular to the axis.

Determination of the Periods. When the computational phase of the study terminated, the data available for the determination of the periods was a set of computer printouts listing h_c, v_c, h_w, and v_w, the heights and velocities at the centerline and wall. If the centerline were falling at a constant rate and had a purely periodic component $U(t)$ with period λ, then it would have the form $h_c = a+bt+U$ for constants a and b; and the velocity would take the form $v_c = b+U'$, a periodic function displaced by an unknown constant b. With this hypothesis, the maxima and minima of v_c should, separately, occur with period λ. In fact, the strongest maxima and minima of v_c are separated by intervals that tend to cluster about a common value. Some of the zeros of v_c, extrema of h_c, are also separated by values that belong to the cluster. A similar analysis applied to the functions h_w and v_w should yield an overlapping cluster; and this is the case. The values of the periods reported in Table II are averages of estimates determined by this procedure.

The data used in this analysis may be complicated by the special nature of the centerline and wall and certainly are confused by nonlinear wave phenomena and by effects of the hemispherical bottom. Although more elaborate statistical and analytic schemes could be used to determine the periods, their application seems unwarranted until the nonlinear feedback and interference phenomena are better understood. In retrospect it would have been desirable to integrate the Eulerian form of the equations, (8a) and (9a), along several fixed radii. This would increase confidence in the determination of the periods and provide additional data on wave motion. For studying the latter, detailed information on the free surface curvature and the potential and kinetic energy terms of the Bernoulli equation along the free surface would be desirable for selected portions of runs where phenomena of interest have been observed. Plotting trajectories of points on the free surface where these functions have constant value on a graph showing successive positions of the free surface would be a simple way to organize and to begin the analysis of this data.

Nondimensionalization and Normalization. The nondimensionalizing relations used in this study are

$$\bar{X} = aX, \quad \bar{t} = t\pi a^3/Q, \quad \text{and } \bar{\varphi} = \varphi Q/\pi a \tag{19}$$

where the quantities topped by a bar are dimensional, a is the characteristic length (tank radius), Q is the volumetric drain rate, and X is a generic spatial variable. Here the unit of nondimensional time is that time needed to drain a right cylinder of radius a and height a at a given drain rate. This time scale may be inappropriate when draining excites axisymmetric oscillations of the free surface. The nondimensionalizing relations used in previous sloshing work [17, p. 11] are an alternative. They are

$$\bar{X} = aX, \quad \bar{t} = t^* \left|(1+B)\sigma/(\rho a^3)\right|^{-\frac{1}{2}}, \quad \text{and } \bar{\varphi} = \varphi^* \left|(1+B)\sigma a/\rho\right|^{\frac{1}{2}} \tag{20}$$

where t^* and φ^* are nondimensional sloshing time and potential, B is the Bond number, and ρ and σ are the dimensional liquid density and surface tension. The relations connecting the two nondimensionalizations take the form

$$t = t^*K \text{ and } \varphi = \varphi^*/K \text{ with } K = (W/(1+B))^{\frac{1}{2}} \tag{21}$$

and show that the two nondimensionalizations are equivalent when K is one. For values of the ratio K less than one, the principal concern in developing the program for this study, the draining potential is the larger of the two; and the draining time is the smaller. One justification for continuing the draining nondimensionalization from the previous study is that the greater potential range for K less than one facilitates accurate determination of potential differences, a continuing source of difficulty in the program. For values of K greater than one, the draining nondimensionalization was known to be appropriate. However, the sloshing nondimensionalization (20) and its relation to the draining nondimensionalization (21) play an important theoretical role in discussing the results.

Accuracy. The principal check on overall accuracy is the conservation of volume. The average percentage change in volume from start to finish for the last eight cases run is .024% with a spread from .001 to .065. Cases 1 and 2 (see Table I for parameters) have a change of less than .276%, which will be

discussed in the next section. Time does not permit extracting this data from the early runs, Cases 5, 29, 32, and 35; but no cause for concern was observed in earlier analysis. The value of the stream function on the free surface at the axis approximates -1 to four or more digits, except that two or three digits may be acceptable for very long running problems very low in the tank.

Irregularities in the streamlines, over and above those due to digitalization in plotting, are visible in the corners at the free surface and just above the drain. Those at the free surface are the result of poor determination of differences of the potential in regions where it has a small gradient. Those near the drain result from the difficulty in evaluating the auxiliary potential low in the tank and are sometimes compounded by too coarse a mesh.

DISCUSSION OF RESULTS

Simulations of low gravity draining have been computed covering a wide range of parameters: two Bond numbers, 0 and 5; three and one half decades in Weber number, .01 through 50; two initial volumes, $5\pi/3$ and $8\pi/3$ (flat filling in normal gravity to two and three tank radii); and two drain radii, 1/30 and 1/10 of the tank radius. Fourteen simulations have been computed and the data is presented graphically in Figures 4 through 17.

Each figure begins with two facing plots which provide a two-dimensional representation of the three-dimensional time history of the simulation. Subsequent pages may give expanded scale plots or streamline patterns illustrating significant details of the simulation. These data figures are arranged, for ease in cross reference, with those for Bond number 0 preceding those for Bond number 5 and within each group in order of increasing Weber number with the higher fill levels last. Each simulation is identified by a case number; and its parameters are identified by a symbol (B, W, r_o, V_o); so the expression Case 1 (0, .01, 1/10, $5\pi/3$) means that Bond number 0, Weber number .01, drain radius 1/10, and initial volume $5\pi/3$ are parameters for Case 1. Table I contains a list of the case numbers and the corresponding parameters for ready reference.

Because the simulations are solutions of an initial boundary value problem that is well posed both numerically and mathematically, their physical features should vary continuously with the parameters. This principle is the basis for the analysis in this section; however, with fourteen data points widely spread in a four-parameter input matrix, identifying continuous variation is sometimes difficult. This study pinpoints some open questions.

The analysis of low gravity draining phenomena given in the first part of this section is based upon the totality of simulation data; however, it is presented when possible in terms of the graphical data in Figures 4 through 17. Next, two simulations are compared with two experiments performed at NASA-Lewis Research Center. The agreement is excellent; on the basis of the preceding analysis, many common details are revealed.

An analysis of the numerical data, presented in Table I, follows. The liquid residual volume, V_r, is expressed as a fraction of a hemispherical volume; the initial volume, V_o, is expressed throughout this report as nondimensional geometric volume. Liquid residual volume is discussed as a function of the problem parameters and the correlation variable $W/(1+B)$. Graphical summaries of the data from this study and its predecessor [1] are presented in form suitable for engineering use. The final part of this section concerns wave motion. It is shown that the period of the axisymmetric oscillations excited by draining, when normalized to the sloshing time scale, is a constant characteristic of Bond number.

Analysis of the Simulations

As background for analyzing the data presented in Figures 4 through 17, the wall rise and initial transient phenomena are discussed. In the analysis, cases are grouped according to common physical phenomena or a common parameter change. Because there are four continuous parameters to vary, any single classification scheme is unlikely to be satisfactory. However, most schemes would include a capillarity dominated regime characterized by low Weber number, low liquid residuals, and many small waves. (The conditions under which these waves may be described by a small amplitude approximation are an open question.) Only in this regime does drain radius appear to be a significant parameter. The capillary dominated regime merges continuously into another which is characterized by few waves of large amplitude which repeat with small damping. This region is important, first, because it can be reached experimentally and, second, because low gravity phenomena occur on a larger scale than in the capillarity regime and more rapidly than in the draining dominated regime.

For the fill levels considered here, high Weber number cases fall into this regime, which is characterized by a sheet of liquid left behind on the wall as liquid is withdrawn rapidly from the center of the tank. Fill level is an important parameter; with large fills there is more time for the contact point to fall and for liquid retained high on the wall to drain into the bulk of the liquid. The one example of this phenomenon encountered

in this study did not produce geysering but rather a falling, thinning wall sheet. The simulation produced a moving free surface that approaches the wall so closely that, in a corresponding experiment, the liquid would separate, leaving a sheet on the wall, and the bulk of the liquid would continue into the drain. This behavior violates a fundamental assumption in the model: the liquid remains connected. Geysering was provided for; but not separation. The only problem in including separation in the simulation program is an adequate physical description of the separation process.

Because analysis was limited by the time needed to develop the program and learn how to use it to produce the simulations, all data files generated in the simulations have been stored on magnetic tape. Computer assisted re-analyses of existing data is possible. The frequent restart points can be used with the present or an augmented program to complete a simulation or to obtain additional analytic data for selected time intervals from a restart.

During the course of this study a special descriptive terminology was adopted for referring to waves in the streamline end trajectories. A wave begins at the free surface when the trajectories near the contact point are at a maximum displacement to the left; it reaches its maximum when the maximum displacement of the streamline ends to the right reaches the centerline; and it begins again when the maximum displacement to the left begins at the wall. Thus the beginning of a wave corresponds to a hang-up or slowdown at the wall, the maximum to a hang-up or slowdown at the centerline.

The discussion of the data begins in the capillarity dominated regime and moves through the finite amplitude region at Bond number 0 to the development of wall sheets at high Weber number. This is followed by a detailed discussion of the thinning wall sheet case, with recommendations for continuation. The effect of Bond number is discussed next.

The effect of fill level is considered last, because two of the simulations involved are those compared with experiments in the part which follows immediately.

Rises at the Wall. The impulsive opening of the drain sets up instantaneously throughout the liquid, a velocity field directed toward the orifice. Because

the velocity potential satisfies Laplace's equation, the initial streamlines and velocity field are perpendicular to the free surface (cf. Figure 7(c)). For the fill levels considered here, the initial streamlines depend principally on Bond number, are curved near the free surface, are straight lines parallel to the axis in the body of the tank, and form a fan into the drain in the hemisphere (cf. [1], pp. 63, 67, and 95) for full initial streamline plots). Tracing a given initial streamline close to the wall backward from the body of the tank yields first a straight line segment parallel to the wall and then a curve that moves away from the wall to become perpendicular to the free surface. A large volume of liquid is trapped between the initial streamline, the free surface, and the wall. Because the streamlines move very slowly towards the wall and the free surface is hardly changing in this region, the volume just described can be used as an instantaneous test volume (cf. Figures 7(c) through (h)). Because the lower part of the given streamline is essentially fixed and parallel to the wall, liquid is flowing from this region into the drain at a constant rate. (Were a fixed test volume to be used, an insignificant outflow over the boundary within the tank would develop as the streamlines moved toward the wall.) The radial component of the velocity at the free surface crams the upper part of the volume against the wall more rapidly than can be compensated for by the rate at which liquid is being withdrawn into the drain. Hence liquid near the contact point must climb the wall. This effect recurs repeatedly during wave motion whenever the streamlines near the contact point curve away from the wall (cf. Figures 6(f), (g), and (h); and Figures 10(f) and (g)). Frequently, the net result is a marked slowing in the fall of the wall point. The initial rise at the wall, and the tendency to do so thereafter, depends principally upon the curvature of the free surface and the behavior of the streamlines near the contact point. Therefore, the occurrence does not depend upon the contact angle. However, the magnitude of the effect may be affected by the choice of contact angle. (A contact angle smaller than 5°, possibly 0°, can be used in simulation.)

The Initial Transients. In response to the impulsive opening of the drain, the entire free surface falls, everywhere and in every case. At the contact

point for low Weber numbers, this response may be visible only in the initial velocity distribution; at higher Weber numbers the contact point may continue to fall for a time. The magnitude of the fall is so small that, even when it is visible in the time history of the wall point, it appears as an initial straight line segment. Both the magnitude and duration of the fall appear to increase with Weber number and to decrease with Bond number. The geometric tendency to rise at the contact point eventually overcomes the initial downward velocity. At low Weber numbers the rise is small and brief; at large Weber numbers it is larger and may continue to vapor ingestion. The maximum rise height and the time at which it occurs appear almost independent of fill level; both are decreasing functions of Bond number and increasing functions of Weber number.

Meanwhile, the centerline point on the free surface continues its initial fall. Although the downward velocity is decreasing very slowly, the initial segment of the time history of the centerline point plots as a straight line. The "slope" of this initial segment appears to be characteristic of draining at the given Bond number. More precisely, all initial segments at a given Bond number are initially coincident in shape, independent of fill level; the higher and closer together the two Weber numbers in a comparison, the longer the coincidence lasts. A large neighborhood of the centerline point on the free surface appears to retain its initial shape as it falls. This neighborhood is defined as that region of a subsequent streamline plot in which both the free surface and the streamlines can be brought into coincidence with the original free surface and streamlines. As draining progresses, this neighborhood contracts toward the axis. The time at which this contraction reaches the axis appears to be of the order of the length of time that the initial segment of the centerline time history remains coincident with one for higher Weber number. The initial stretching of the free surface takes place between the wall and the neighborhood which still retains its initial shape. Modification of the program to output and process data quantities which are already computed in the course of the simulation would aid in understanding the physical processes behind these observations.

Effect of Drain Radius. Case 1 (0, .01, 1/10, $5\pi/3$), large drain radius, and Case 2 (0, .01, 1/30, $5\pi/3$), small drain radius, were chosen as a pair likely to show the effect of drain radius. There is a small effect; however, it occurs only near the drain. The streamline trajectories in Figures 4(a) and 5(a) are identical throughout most of the simulation and do not begin to diverge until after the centerline height, h_c, has fallen below .3. Then the trajectories in both cases begin to approach the axis, but those for the small drain do so more rapidly than those for the large drain. This is also evident in Figures 4(b) and 5(b). Although the behavior at the wall is identical, the centerline curve for the large drain near termination is flatter than that for the small drain. Figure 20 shows the patterns of streamlines at comparable times very low in the tank and higher in the tank. The plots in this figure have been carefully aligned so that a triangle may be used to verify the position of comparable points. Figure 20(a) shows that, very low in the tank, the streamline pattern for the larger drain lies to the right of that for the smaller drain. Figure 20(b) shows that the streamline pattern for the two drain sizes coincides except near the drain. The two panels on this page are characteristic of the two drain sizes in the following sense: in any simulation when the free surface is well above $h_c = .5$, the lowest part of its streamline pattern will coincide with one of the two panels. This is a consequence of the draining nondimensionalization, which gives all drains the same outflow rate and allows them to differ only in the size of the orifice.

Waves at Low Weber Number and Bottom Effects. Cases 1 and 2 show eight pure capillary waves, excited by draining, before the free surface begins to move toward the drain. Figures 5(c) and (d) show Case 2 on an expanded scale with more detail of the trajectories near the wall. The amplitudes of the excursions of the streamline end trajectories toward the wall are alternately small and large. A similar pattern can be found in the centerline and wall height plots.

Case 29 (5, .01, 1/30, $5\pi/3$) differs from Cases 1 and 2 in that the Bond number has been increased to 5. Figures 10(a) and (b) show 16 draining induced capillary-gravity waves with small amplitude occurring before vapor in-

gestion. Detail near the wall is provided by the expanded scale plots, Figures 10(c) and (d). In contrast with the alternating amplitudes of the pure capillary waves in Case 2, the amplitudes of the capillary-gravity waves in Case 29 steadily decrease and then increase as the base of the vibrating streamlines progresses into the hemisphere.

When the free surface is high in the tank, the streamlines are relatively widely spread throughout the tank at the level at which they begin to vibrate. Figures 6(d), (e), and (f) are examples of this aspect of general streamline patterns. The feature that changes in the complete sequence of streamline plots through the period in which the increase in wave amplitude occurs is that their lower parts are progressively packed by the hemispherical bottom. This is shown in Figures 10(e) and (f). In Figure 10(e), near the maximum of the wave of largest amplitude low in the tank, the streamlines are confined by the wall and packed throughout the tank. At the beginning of the next wave, Figure 10(f), the streamlines remain packed in the center of the cross-section; but because the contact point is still on the vertical wall, the component of velocity along the free surface is choked off with the relaxation of the streamlines at the wall.

When the contact point is on the hemispherical bottom, the streamlines do not relax much at the beginning of the wave, Figure 10(g), and consequently the strong velocity component along the free surface is maintained. This continues until termination, Figure 10(h), and accounts in part for the low residual in this case. Although a considerable velocity component may develop along the free surface when h_c is low in the tank, it may be cut off by wave action so long as the contact point remains on the wall as in Case 2, Figure 20(a).

Cases 1, 2, and 29 are the only simulations in which a considerable portion of the calculations occurred in the region where the evaluation of the auxiliary potential is unsatisfactory. This fact may cause or contribute to numerical oscillations in the derivatives at the centerline, which are exhibited graphically by the muddy terminations of the two streamline trajectories adjacent to the axis in these three cases. Another factor may be the number of vertical mesh spacings used in the final stages of the calculation: 4, 5, and 7

for Cases 1, 2, and 29, respectively. Overall satisfaction with the endings of these three cases increases as the number of mesh spaces used increases. The percentage change between original and final volume is much higher for Cases 1 and 2 (and presumably Case 29), .276%, than the average of .024% for the remainder of the cases. Although these simulations take 6000 (Case 29) or nearly 8000 (Cases 1 and 2) time steps, the length of the run does not seem to be the cause of the loss of accuracy.

Wave Dispersion, Nonlinear Effects. Case 5 (0, .1, 1/30, $5\pi/3$) is an example of capillary wave action with all details clearly visible. Figures 6(a) and (b) have many as yet unexplained features. When the minor oscillations are smoothed out, it becomes clear that the second major wave reproduces the essential features of the first. The central part of the run including the second maximum was repeated with a smaller time step and the quivers in the trajectories were reproduced. This case was chosen as the example of the sequence of meshes used in a simulation (Figure 3) to show that there is no problem with the mesh. The streamline patterns in Figures 6(c) and (d) are typical of the shape at maximum wall rise and at the maximum of a wave. Comparison of Figure 6(e) with Figure 7(c), which is an example of the common initial shape of the free surface for all cases with B=0 and volume $5\pi/3$, shows that the free surface can recover its initial shape in the course of a capillary wave. This occurs just after the maximum of the first wave at the end of a period of especially rapid fall at the centerline. Figure 6(f) shows the streamline adjacent to the wall bent over very far toward the center just after the wall point has started to rise toward its second maximum. It is just before and during this rise that unexpected behavior begins. Figure 6(g) shows the same streamline again far to the left during the rise at the wall just before termination. Figure 6(h) shows that at termination, although there is a component of flow along the free surface toward the axis, the residual is large because the wave action is trapping much liquid high on the wall.

Comparing Case 5 with Case 2 (Figure 5(c)) shows that the gross features of the former are replicated in the latter, but are somewhat smoothed.

Development of Wall Sheets. Case 8 (0, 1, 1/30, 5 π/3) shown in Figures 7(a) and (b) is either a case in which the wave is very spread out, with none of the capillarity features of the previous Bond number zero cases, or a first example of a case with a wall sheet, a draining dominated case. The centerline initially falls at a rate characteristic of Bond number zero and then transits to a second region in which the fall is again approximately constant. The straight line segment in the wall history before the wall point begins to rise is actually an interval in which the wall point falls in response to the initial draining impulse before it begins to rise. The comparison of Figures 7(c) and (d) side by side may be difficult, overlaying shows that although the free surface in the latter has stretched at the wall, it still has its initial spherical shape at the center. Figures 7(e), (f), and (g) are a sequence showing the streamline shapes as the wall sheet develops and the centerline decelerates in response to a component of flow along the free surface. Figure 7(h) shows the streamline pattern just after the wall begins to fall. Note that at this time the center is well into the second interval of constant velocity. Figures 7(i) and (j) show the patterns at the beginning and end of the final acceleration into the drain.

Case 10 (0, 10, 1/10, 5 π/3), Figures 8(a) and (b), Case 19 (0, 10, 1/10, 8 π/3), Figures 9(a) and (b), Case 37 (5, 10, 1/10, 5 π/3), Figures 13(a) and (b), Case 40 (5, 50, 1/10, 5 π/3), Figures 14(a) and (b), and Case 49 (5, 50, 1/10, 8 π/3), Figures 17(a) and (b), are all characterized by the development of a thick wall sheet, a long continued rise at the contact point, and an initial fall of the centerline at the rate appropriate to the Bond number. The two larger fill cases develop a second region of constant fall at the centerline; but the smaller fill cases go immediately from the initial fall into vapor ingestion. In Cases 37 and 49, at Bond number 5, the wall does fall, but very slowly.

The final free surface on Figure 13(a) has a large salient in the wall sheet and has jumped into the drain. The final curve is the result of the predictor step following the time step shown in Figure 13(d). The preceding time step is shown in Figure 13(c). These figures show the top three lines of the mesh, a wave at the base of the wall sheet, and indicate a mesh problem just above

the drain. It is probable that there should be a small wave, as shown, and that it has been magnified to instability as the result of trying to pack too much mesh into the region above the drain. The liquid residual in Table I is computed from the free surface of Figure 13(d). Because the percentage change in volume is .064%, the result is reliable. Moreover, examination of the centerline time history shows that the rerunning of the end of this case would merely result in a miniscule change in the liquid residual and reduction of the percentage change in volume to the general level.

The Thinning Wall Sheet. Case 46 (5, 10, 1/10, $8\pi/3$), Figures 16(a) and (b), behaves initially as a draining dominated case in which the wall point is falling, eventually quite rapidly. The centerline point exhibits a new behavior. It starts falling at the slope characteristic of Bond number 5, then transits to a second constant rate of fall, which also occurs for Case 49, and finally transits to a third (new) constant rate for a shorter period just before it starts to accelerate into the drain. The values for this case in Table I are for the terminal point of the doubtful segment shown in Figure 16(b). When the terminal segment of the centerline time history of Case 37, Figure 13(b), is used to extrapolate the centerline history of Case 46, the resulting estimated volume is at most 3% lower than the value given in Table I (see the following paragraph on Effect of Fill Level).

Comparing Figure 16(c), the streamlines and free surface shape when the computation is running smoothly, with Figure 16(d), the streamlines at the time of the last free surface plotted on Figure 16(a), shows that the wall has fallen, shortened, and thinned considerably. In the last set of streamlines the .02 streamline reaches up into the wall sheet. Thus the wall sheet is providing at least two percent of the flow out the drain and this is going through the neck in the wall sheet. The computer listing shows that the maximum vertical velocity downward on the free surface is at the centerline and that there is a secondary maximum at the mesh point just below the neck. The table below shows the widths of the neck, the local maximum vertical velocity (at the point on the free surface below the neck), the maximum width of the wall sheet, its length (above the neck), and its volume as a percentage of the current volume in the tank.

		Neck		Wall Sheet		
Time Step	Time	Width	Maximum Vertical Velocity	Maximum Width	Length	Volume
685	1.9707	.006	-1.41	.012	.932	2.55%
695	2.0004	.004	-1.66	.012	.941	2.64%
702	2.0213	.002	-2.10	.012	.953	2.66%

The volume within the wall sheet decreases by about 3% during the period covered by the table; while the total volume decreases by about 7%. The minimum vertical velocity on the free surface outside the wall sheet, which is the easily available measure of the bulk velocity in the liquid, increases from -1.12 to -1.55 in this period. The vertical velocity distribution along the free surface above the neck is a uniform decrease in magnitude from the neck to the contact point where it changes from -1.20 to -1.23. Thus both the wall sheet and the bulk of the liquid are speeding up; but the latter more than the former. It appears that the inviscid model is predicting that liquid will separate and the wall sheet will be left flowing down the wall at a slower rate than the bulk of the liquid.

This unexpected behavior was not included in the design of the program; however, it is implicit in the mathematical model, for there is no reason why the dynamics of the problem should not force the free surface against the wall. Were the physics for breaking the domain into two pieces included in the model it would not be difficult to adapt the program to carry on with the lower piece. The fate of the wall sheet could also be determined.

The thinning of the wall sheet brings into question the assumption that viscous effects are negligible. The justification of this assumption is based upon the fact that experimentally observed wall sheets have thicknesses much greater than those predicted by the analysis given in Appendix A of [1] . There an asymptotic expression for the thickness of a viscous wall sheet in a circular cylindrical tank is given as

$$h_o = 1.35\ (\mu \bar{v}_o/\sigma)^{2/3}$$

for zero gravity conditions. In this expression μ is the viscosity, $\bar{v}_o$ is characteristic velocity for the central downward flow in the tank, and h_o is the dimensionless thickness of the wall layer. Recasting this expression into the familiar dimensionless groups, Bond (B), Reynolds (R), and Weber (W) numbers, gives

$$h_o = 1.35\ (W/R)^{2/3}$$

as an equivalent expression. With the assumption of a Reynolds number of 10,000, the values from Case 46, B=5 and W=10, give h_o the value .01. The values for the width of the neck given above indicate that the neglect of viscosity may no longer be strictly justified when the free surface approaches the wall. However, the neglect may be the practical way to solve the problem.

Effect of Bond Number. The most dramatic change with Bond number is the transition at the larger fill level from the draining dominated Case 19 to Case 46 just discussed. At the lower fill level the corresponding Case 10 and Case 37 have essentially the same properties.

The second most dramatic change with Bond number is the jump from Case 8, which is draining dominated, to Case 35(5, 1, 1/30, 5 π/3), Figures 12(a) and (b), which has a single wave of finite amplitude. The combination of draining and gravitational forces suppresses practically all visible capillarity features in the oscillations of the streamline end trajectories in Figure 12(a). Figure 12(b) shows an initial rate of fall at the centerline that is characteristic of all Bond number 5 cases.

In the transition from Case 5 to Case 32 (5, .1, 1/30, 5 π/3), Figures 11(a) and (b), the waves double in number, become relatively smooth, and definitely decrease in amplitude. When Case 32 is compared with Case 29 (Figure 10(c)), some common features emerge: an initial straight drop of the free surface which lasts longer near the axis than at the wall, a jump toward the axis of the streamline end trajectories near the axis just before the maximum of the first wave, and an overshoot of the trajectories near the axis on the recovery from the first wave. These appear to be characteristic of capillary-gravity waves because they occur with very small magnitude in Case 35.

Effect of Fill Level. There are three comparisons between fill levels in the draining dominated regime. The striking feature of all three is that the wall height curve for the smaller fill completely overlays that for the larger. Thus behavior at the wall is independent of fill level so long as wave action does not occur. At the centerline, the initial segment of the smaller fill level overlays that of the larger but breaks away at different times. When large scale free surface and streamline end trajectory plots for the smaller fill are overlaid on the plot for the larger a curious pattern of agreement is revealed. In each of the cases, the streamline end trajectories for the smaller fill are identical with those for the larger for a short distance below the free surface. The area of disagreement spreads toward the axis and wall but never reaches the latter. The height at which the area of disagreement reaches the axis for the lower fill level is about 1.3 for Cases 10 and 19, Figures 8(b) and 9(b), 1.5 for Cases 37 and 46, Figures 13(b) and 16(b), and 1.6 for Cases 40 and 49, Figures 14(b) and 17(b). For each Weber number, the lower ends of the centerline time histories in the figures just cited can be made to coincide. What is more, the lower ends of the centerline time histories for all cases with the same Weber number coincide and the height of coincidence increases with Weber number. This fact was used in estimating how close Case 46 was to vapor ingestion.

Case 43 (5, 1, 1/10, 8 π/3), Figures 15(a) and (b), is a higher fill level analog of Case 35. Even with different scales, the strong resemblance between Figures 15(a) and 12(a) is apparent; not only does the latter resemble the initial segment of the former but it also appears to be the terminal segment. When Figure 12(b) is laid over the initial part of Figure 15(b), the curves for the height at the wall can be made to coincide and the initial part of the curves for the centerline height are identical, diverging only when the curve for Case 35 begins to accelerate toward the drain. When an attempt is made to match Figure 12(b) with the terminal segment of Figure 15(b), the match is remarkable. The following results for Case 43 emerge from the last comparison: the wall is falling at the same rate in both of the nearly straight segments; the rate of fall of the centerline in the second straight segment is approximately the initial rate of fall; and the terminal behavior is only

slightly different. The principal difference between the two waves in Case 43 is that both the wall and centerline curves are flatter in the transition from the second wave to terminal behavior than in the transition between waves. Thus it appears that the effect of increasing the fill and keeping the other parameters fixed is to replicate the wave behavior starting from the beginning. Consequently, the value of the liquid residuals may depend strongly upon the initial fill level.

Comparison with Experimental Data

Data from two experimental runs made at the NASA-Lewis Research Center were supplied for comparison with the simulations. The difference in initial conditions is the principal problem in making such comparisons. The simulations begin with an equilibrium interface with zero velocity. The Lewis Research Center experimental procedure calls for initiation of outflow when the interface centerline reaches its low point in its first pass through equilibrium [2]. A second problem is the difficulty in reading the point at which the interface meets the tank wall. And finally there is the unknown effect replacing the 0° contact angle by the 5° contact angle used in the simulations.

Points from an experimental run with the parameter set (5.0, .905, .10, $5\pi/3$) are compared in Figure 18 with the computed centerline and wall height curves for Case 35 (5, 1, 1/30, $5\pi/3$). The experimental points lie very close to the computed centerline heights; there is agreement in level and trend between the experimental and computed wall heights. At this Bond number, the difference in drain radius should have no effect; however, the experiment with the smaller Weber number should have a longer drain time; and this is observed. At the centerline the initial experimental point is low with respect to the simulation and it initially falls at a rate less than the initial rate characteristic of Bond number 5. This suggests a small upward velocity at the centerline. At the wall the experimental point is low and initially falls. This suggests a downward initial velocity at the wall. The divergence in the initial conditions accounts for the flattening of both experimental curves with respect to the computed curves.

Although it has not been specifically brought out, experience in following waves in streamline end trajectories across the tank suggests that the excess experimental velocity at the wall travels across the tank to the centerline and back to the wall again. When all the excess velocity finally leaves the wall, it falls at the rate characteristic of the basic problem. The excess velocity reaches the centerline just before the maximum of the wave occurs and accounts for the increase in the experimental rate of fall. The excess velocity returning to the wall again contributes to the divergence of the rates of fall at the wall just before vapor ingestion. Examination of Figure 18 suggests that the half period of the wave of excess velocity is about .5; from Table II, the value of the period for Case 43 is .96.

In spite of the difficulty in reading wall points, there is a coincidence of the experimental and computed curves during the time that the wall is falling at the rate characteristic of both Case 35 and Case 43. After the effect of the small initial velocity at the centerline dies out, the experimental centerline point does fall at approximately the initial rate characteristic of Bond number 5 and follows the computed curve through the transition into the maximum of the wave very well. Although the experimental points are lower, both curves fall at similar rates. The chief discrepancy between experiment and simulation is that the latter predicts a slowing down of the wall point just before vapor ingestion, whereas the experimental point continues to fall as a result of the wave of excess velocity. The larger contact angle in the simulation may also contribute to the difference. The agreement in this comparison is excellent.

Points from an experimental run with the parameter set (5.0, .945, .10, $8\pi/3$) are compared in Figure 19 with the computed centerline and wall height curves for Case 43 (5, 1, 1/10, $8\pi/3$). Again the experimental points at the centerline lie close to the computed curve. However, the experimental determination of the wall heights only resembles the computed curve in general slope and lies so much below it that to use the experimental wall heights in constructing a conjectured initial velocity to explain the divergences from the good agreement at the centerline would be unrealistic. The initial centerline point is above the computed point. However, both fall at the rate character-

istic of Bond number 5 for approximately the same length of time. Thus it would appear that the initial experimental interface had the shape of the Bond number 5 equilibrium free surface and a very small residual velocity over a very large part of the tank. The first experimental wave begins about the same time as the computed one reaches its maximum perhaps a bit earlier, and is of much smaller amplitude. Both sets of data return to an approximation of the characteristic rate of fall. Because it is expected, an experimental second wave of small amplitude can be detected at the appropriate time. The smaller experimental Weber number again produces a slightly longer drain time. Although the agreement is not so striking as in the previous comparison, it is good, particularly in the initial centerline detail.

Liquid Residuals

The quantity of liquid left in a tank after vapor ingestion occurs has considerable impact on the design of orbital transfer systems. Residual weight must be accepted as a weight penalty or traded with the weight and other disadvantages of alternate means that reduce residuals below values for a clean tank. Obtaining data on residuals for low gravity draining of hemispherically bottomed, cylindrical tanks was a major objective of this investigation. The data in Table I and the plots in Figures 21 - 23 are useful for design studies and meet this objective. The following paragraphs are a discussion of the relative significance of drain size, initial fill volume, Bond number, and Weber number on the residual volume. Generally, the numerically determined values of residual volume are somewhat larger than those obtained experimentally [2] ; the differences are attributed, primarily to nonequilibrium free surfaces in the experiments at the start of draining and, secondarily to a larger contact angle (5^{o}) used in the calculated cases. The numerically determined values are conservative, however.

Drain Size. Observations regarding the general influence of drain size on the draining solutions are discussed earlier in this section; here specific results are presented regarding the effect of drain size on the residual volume.

From the calculations of [1] , it was concluded that Weber number must be much less than one or that for a given Weber number the Bond number must be

much greater than one to cause appreciable parametric dependence of residual volume on drain size. Cases 1 and 2, in which W = .01 and r_o = 1/10 and 1/30, respectively, were selected to investigate this parameter. (The same values but with B=5 would have shown a greater effect, but data for B=0 were considered particularly desirable.) Review of Figures 4(a), 4(b), 5(a), and 5(b) do not show appreciable differences in draining features between Cases 1 and 2 up to vapor ingestion; this is particularly evident in Figures 20(a) and 20(b) in which streamline patterns are compared. Had a better numerical ending been possible for Case 1 (cf. Figures 4(a) and 4(b)), a larger numerical difference between values of V_r would have been found. The values of V_r for Cases 1 and 2, which are given in Table I, differ by 1.5%. Thus, one must reduce V_r below the values for Case 1 and 2 to obtain appreciable variation of residuals with drain size.

Initial Fill Volume. The initial fill level, h_c, defined as the initial height of the equilibrium free surface at the tank axis, was chosen as a parameter in the survey of draining solutions reported in [1] . The initial fill volume, V_o, is used herein instead. There are advantages in selecting either one, but the data for V_r given in [1] suggest that a survey at fixed values of V_o offers a more consistent and useful grouping of residual volume data when considering the major parameters of Bond number and Weber number. Also, in applications one is interested in a draining efficiency, $1 - V_r/V_o$, so that the best values of Bond and Weber number can be combined to minimize this quantity. Two values of V_o were selected, namely, $5\pi/3$ and $8\pi/3$ (cf. Table I). For fixed values of B, W, and r_o, Figure 8 (Case 10) is compared with Figure 9 (Case 19); Figure 13 (Case 37) with Figure 16 (Case 46); and Figure 14 (Case 40) with Figure 17 (Case 49). Except for Cases 37 and 46, the residual volume increases as V_o increases; evidently that the longer wall layers for the deeper cases cause the larger residual volume. Generally, as W and V_o increase residuals increase, but one must use caution because for some intermediate Weber numbers and nonzero Bond number, such as in Cases 37 and 46, the residual volume decreased instead. For these two cases the wall point starts to move downward quite rapidly, after the characteristic initial delay, and the resulting wave action on the free surface extends the time for

vapor ingestion and thus gives lower residuals. The conclusion that residuals increase with increasing initial fill volume is, therefore, conditioned by saying that the Weber number must be so large that the wall point never has enough time to get started moving downward at an appreciable rate before vapor ingestion occurs.

The most remarkable results obtained from varying initial fill volume are for Cases 35 and 43 (cf. Figures 12(a) and 15(a)). Case 35, where $V_o = 5\pi/3$, appears to duplicate Case 43 once the free surface in the latter reaches a value of $z = 1.7$ to 1.8 at the centerline. From Table I the values of residual volume differ very little suggesting that for W=1 and B=5, the transition has been made (cf. Figure 21). This agreement may be coincidental for the two cases because the residuals will be altered if one has vapor ingestion in different parts of a wave. As the Weber number decreases, this effect should diminish and the dependence on fill level should disappear. Unfortunately, deep cases for B=0 are not available to define the transition, but comparing Case 5, in which $W = 0.1$, and Case 8, in which $W = 1$, suggests that the transition likely occurs at or near $W = 0.1$ for B=0 because the appearance of the wave action in Figure 6(a) is so similar to that in Figure 12(a) for $B = 5$. For Weber numbers much less than one, ample time is available to allow the free surface to oscillate freely, producing the patterns seen in Cases 1, 2, and 29, for example, and eliminate any dependence on V_o.

Weber Number, Bond Number, and W/(1+B). Several cases for $B = 0$ and 5 were computed to define the dependence of residual volume on Weber number. The data reported in Table I and plotted in Figure 21 span three and one-half decades of Weber number. In retrospect, additional computations for even smaller values of W and a complete survey of W at a larger Bond number would have been desirable. However, the existing data, coupled with available experimental measurements for very large Bond number [2] , suffice to define the pattern of the residual volume curves (Figures 21 and 22).

As a function of W, the computed data for residual volume divide into three regimes: one, in which draining forces dominate (W large); two, in which capillary forces dominate (W small); and three, the transition between high

and low W (W of order one). Boundaries between the three regimes are not sharply drawn; but the asymptotic behavior in the large W and small W zones is evident from the S-shaped curves that result (see plots of V_r vs. W in Figure 21) and in the remarkably different character of the simulation plots (Figures 5(a) - 17(a)). The appearance of these regimes stems from the time scaling of a given problem. In one extreme, draining is so rapid that liquid is withdrawn only from the central part of the tank leaving wall layers and a large residual; in the other extreme, capillary and gravity forces have ample time to restore the free surface by forcing draining from the wall region as well as from the central part of the tank. The latter idea is amply demonstrated by the induced wave motion and oscillatory streamlines in Figure 10 (e) - (h).

For engineering calculations in which an estimate of residual volume is required, the graphs in Figure 22 are recommended. Here residual volume is related to the parameter, W/(1+B), suggested in [1] as the simplest combination of W and B that produces the proper limits for B tending to zero and infinity. This parameter dramatically reduces the parametric dependence of V_r on B and permits comparison with high Bond number data. Some parametric spread of the plots in Figure 22 with Bond number is expected because of variations due to low gravity free surface shapes which cannot be normalized with this simple relationship.

All the cases computed in this investigation, as well as in [1], are shown on the plot of t_{vi} vs. W/(1+B) in Figure 23. Using the formula $V_r=3((V_o/\pi)-t_{vi})/2$ one can back out estimates for residuals regardless of initial fill volume, V_o, or fill level, h_c. Earlier work for high gravity draining resulted in simple expressions for computing a critical height defined as the liquid level at the incipience of vapor ingestion (see [2], [17], and [18]). This concept for large B is very useful for predicting residuals because the shape of the free surface is essentially flat; for low-to-intermediate values of B this approach is not accurate and the substitution of estimates based on Figures 22 and 23 is recommended.

Wave Motion

Cases with $W/(1+B) < 1$ (Cases 1, 2, 5, 29, 32, 35, and 43) developed axisymmetric slosh at the free surface. For these cases the draining time is long enough to observe one or more periods of the wave motion. From the listings of the solutions, tabulations of the periods were made for those cycles not immediately altered by the rapid acceleration of the free surface into the drain. The values were averaged and the results tabulated as λ_{d_1} in Table II. Further, these wave periods were plotted against $(W/(1+B))^{\frac{1}{2}}$, the ratio of the sloshing and draining time scales (Figure 24). The straight lines in Figure 24 and their 45° slope suggest that the periods measured in the time scale of the draining nondimensionalization should be rescaled in terms of the sloshing time unit, $(\rho a^3/\sigma(1+B))^{\frac{1}{2}}$, introduced in [17] and discussed in Numerical Analysis as an alternate to the draining time unit, $\pi a^3/Q$. This was done and the results tabulated as λ^* in Table II. The values of λ^* are constant for the two Bond numbers; dispersions are attributed to the crude calculations used to obtain λ_d.

These results suggest that the periods of draining induced oscillations cluster about a constant value for each Bond number if Weber number is less than or equal to one. At higher values of Weber number the waves are still present but not easily observed because of short drain times compared to the period λ_d. For large Weber numbers and very deep cases which would prolong the drain time, one could expect large amplitude slosh with potential geysering at the centerline. In this case the dynamics would be nonlinear and λ^* would likely exhibit considerable deviation from the values in Table II.

In [1; Figure 12, pp. 95-99], wave motion is simulated for $B = 19.32$, $W = 3.41$, and $h_c = 2.0$. The value of λ_d is estimated to fall in the range 1.2 - 1.3 and, as a result, λ^* in 2.9 - 3.2. Used in conjunction with the values for $B = 0$ and 5 in Table II, λ^* generally increases with Bond number.

The investigation of Saad and Oliver [10] demonstrated the existence of draining-initiated waves by a linear analysis in which the low-gravity liquid-vapor interface was assumed flat (90° - contact angle or a sufficiently large Bond number). Their work did not require the velocity-squared term in

the Bernoulli equation to obtain linearized wave action. For W/(1+B) small enough and small contact angle, an analysis similar to that of Saad and Oliver would provide results similar to those given herein because the simulated wave amplitudes are small. For W/(1+B) of order one or greater and with arbitrarily deep initial fills, a full simulation is required to follow the finite amplitude motion; but additional simulations with the present computer program would be needed to define completely the transition regime between these two extremes.

SUMMARY OF RESULTS

The basic results of the Numerical Simulation of Low Gravity Draining study are fourteen simulations and a computer program using new techniques.

(1) Fourteen nondimensional simulations cover three and a half decades in Weber number, W = .01 through 50, two Bond numbers, B = 0 and 5, two drain radii, 1/30 and 1/10 of the tank radius, and two initial volumes, $5\pi/3$ and $8\pi/3$.

(2) The computer program solves the difficult, but well posed, initial boundary-value problem over a wide range of parameters and forms of solutions. The continuity of the solutions as a function of the parameters is a fundamental tool used in the analysis to bridge gaps between widely spaced data points.

(3) Two simulations are compared with two similar NASA-Lewis Research Center experiments. Agreement is excellent.

(4) The range of simulation in Weber number extends that of experiment by two decades.

(5) A principal goal of the study was to determine the liquid residual, V_r, for a wide parameter range. Together with values from earlier Lockheed computations, V_r is plotted against W and W/(1+B). The latter is the simplest parameter that connects somewhat similar cases and occurs in the transformation between the time scales used for nondimensionalizing draining and sloshing problems.

(6) For design studies, the recommended way to determine V_r is to use the equation $V_r = 3((V_o/\pi) - t_{vi})/2$, where V_o is initial nondimensional volume and t_{vi} is vapor ingestion time given by the plot of t_{vi} against W/(1+B).

(7) The S-shaped curves of V_r against W suggest three regimes: (i) a capillary regime, characterized by low Weber numbers, low residuals, and many small waves, in which capillary and gravitational forces have time to drain liquid repeatedly away from the wall; (ii) a

draining regime, characterized by high Weber number, large residuals, and the development of a wall sheet, in which the draining simply draws liquid from the center of the tank with the wall sheet left behind; and (iii) a transition region between the two extremes, where there are few waves of large amplitude.

(8) Drain radius has a significant influence on residual volume for Weber numbers much less than one or, at a fixed Weber number, for Bond numbers much greater than one.

(9) The periods of the waves become a constant, characteristic of the Bond number, when normalized to the sloshing time scale.

(10) Fill level is a very important parameter in the draining dominated regime. What happens at very high fill levels when there is time for the wall sheet to reorient is an open question.

(11) Increasing the Bond number may (i) introduce more waves of smaller amplitude in the capillary regime, (ii) change the nature of the problem from one in the draining regime to one with waves, or (iii) simply reduce the time scale in the draining regime, that is, permit the wall sheet to thin more.

(12) Control of mesh spacing along the stretching and contracting free surface was achieved by the method of variable trajectories in which a small auxiliary kinematic velocity is added to the Lagrangian velocity components at each time step to insure that the computational points maintain a desired distribution. The Bernoulli equation at the computational points is modified to account for the change in direction. This new method was developed specifically for this problem.

(13) The success of these simulations has demonstrated the utility of the method of moving triangular meshes, in which parts of the mesh are revised periodically and parts of mesh rows and columns are dropped and added to accommodate the motion of the free surface.

(14) A simulation for B = 5, W = 10, and an initial fill of $8\pi/3$ predicts on the basis of the inviscid, irrotational model that the liquid in a very thin falling wall sheet may separate and be left on the wall, while the bulk of the liquid continues down the drain. This simulation shows the power of the program; it continues the solution until the neck is .002 of a tank radius in width. It also suggests that there is a region near the boundary of the transition regime where the neglect of viscosity may be questioned.

PAGES MISSING FROM AVAILABLE VERSION

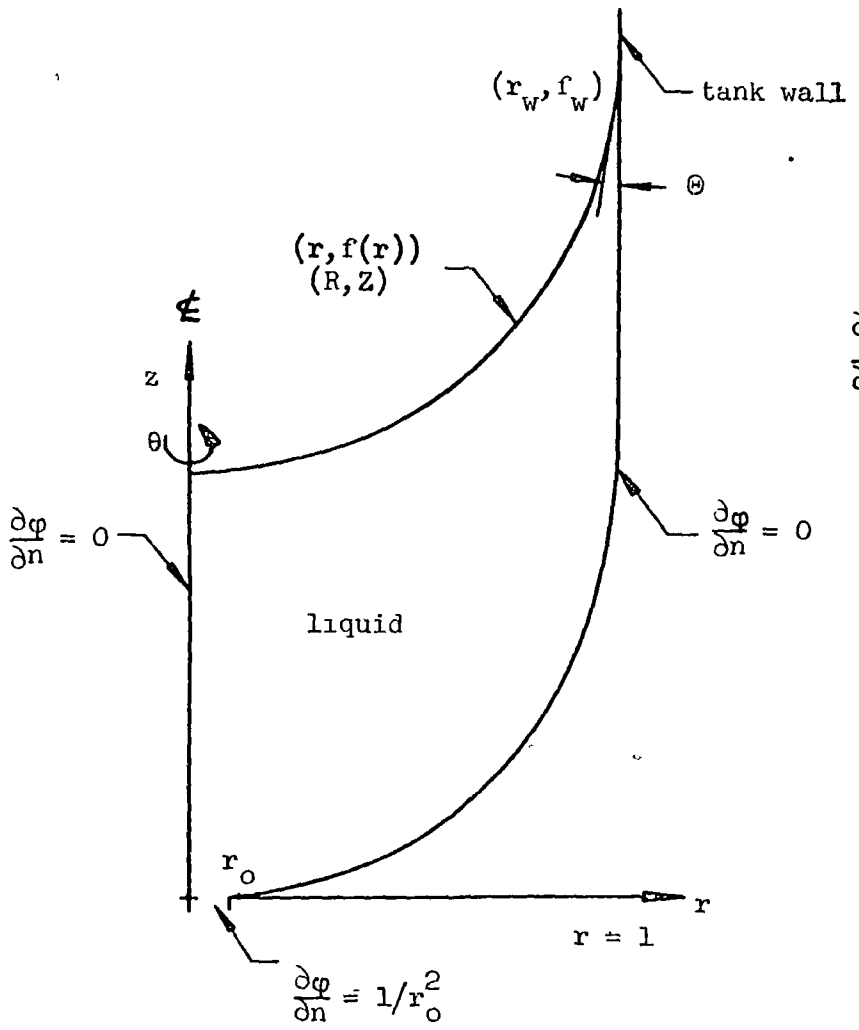

(a) Potential φ.

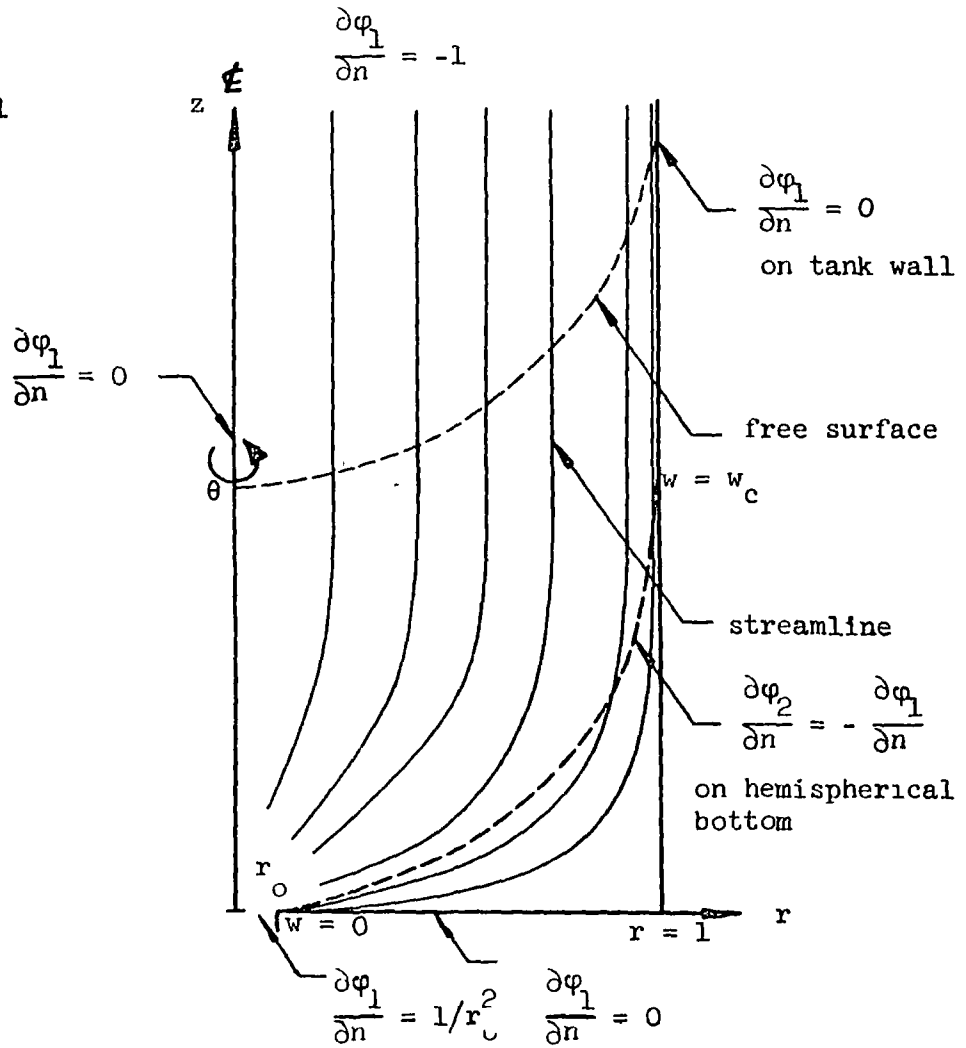

(b) Auxiliary potential φ_1.

Figure 1. Definition of geometry and coordinate system for the draining problem.

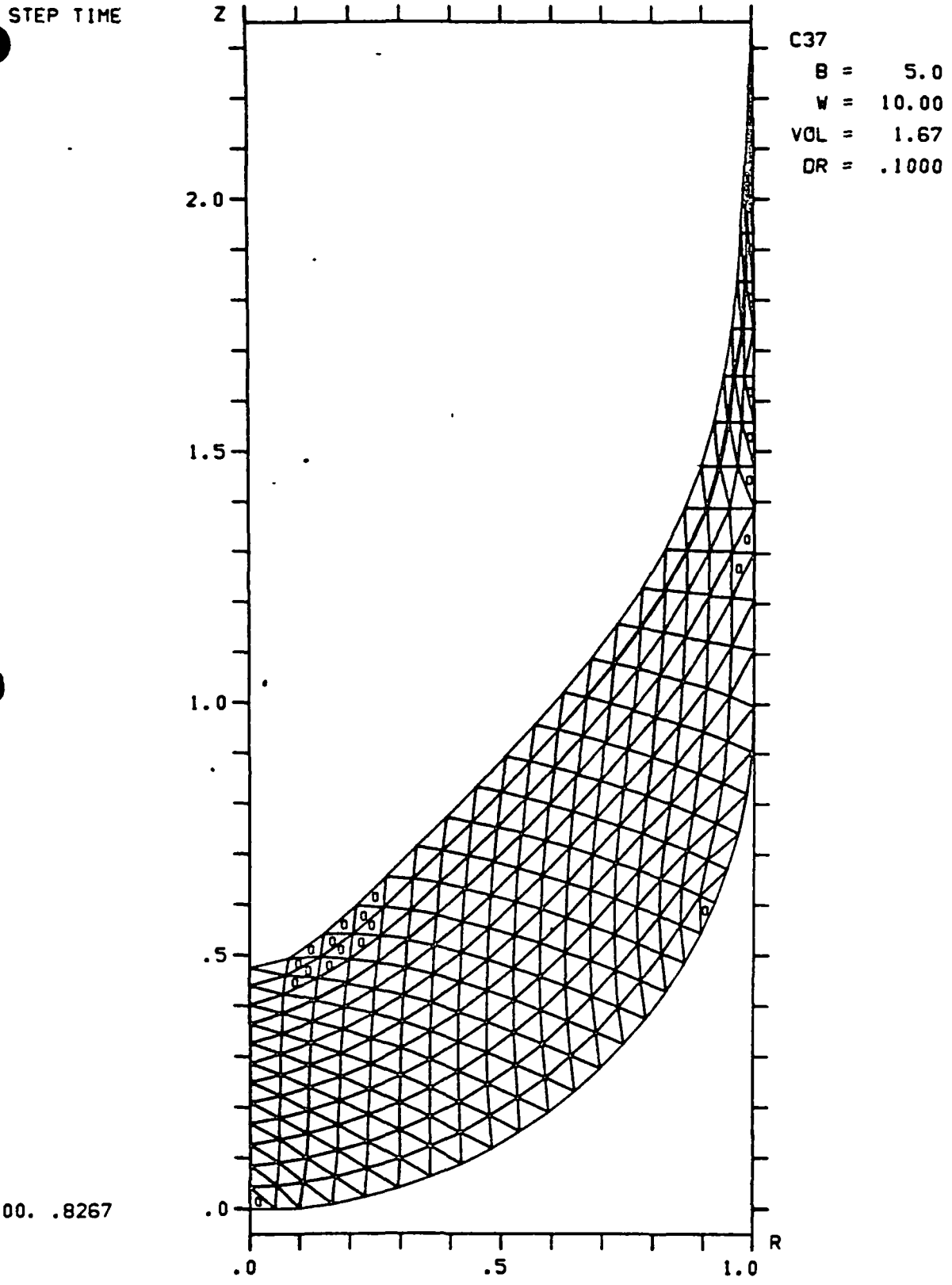

(a) Physical mesh at t=.8267.

Figure 2. Triangular mesh generated for Case 37; $(B, W, r_o, V_o)=(5, 10, 1/10, 5\pi/3)$.

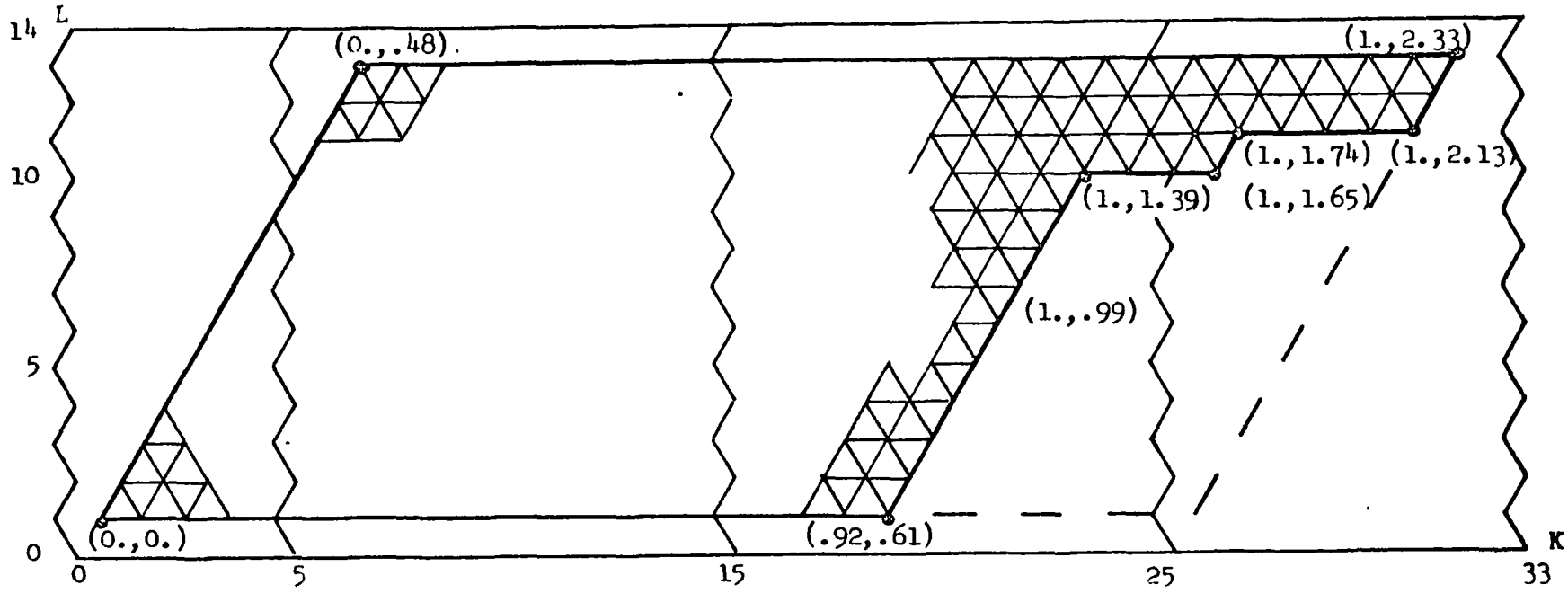

(b) Logical diagram at t = .8267. The triangular mesh in Figure 2(a) can be deformed into the regular triangular mesh in the interior of the polygon (heavy solid lines). Boundary points of the physical mesh given in parentheses map into the adjacent, dotted (.) points by the polygon. The lower parts of seven mesh columns have been dropped from the bottom of the original logical diagram (dashed lines) to accommodate the developing wall sheet.

Figure 2 (cont). Triangular mesh generated for Case 37; $(B, W, r_o, V_o) = (5, 10, 1/10, 5\pi/3)$.

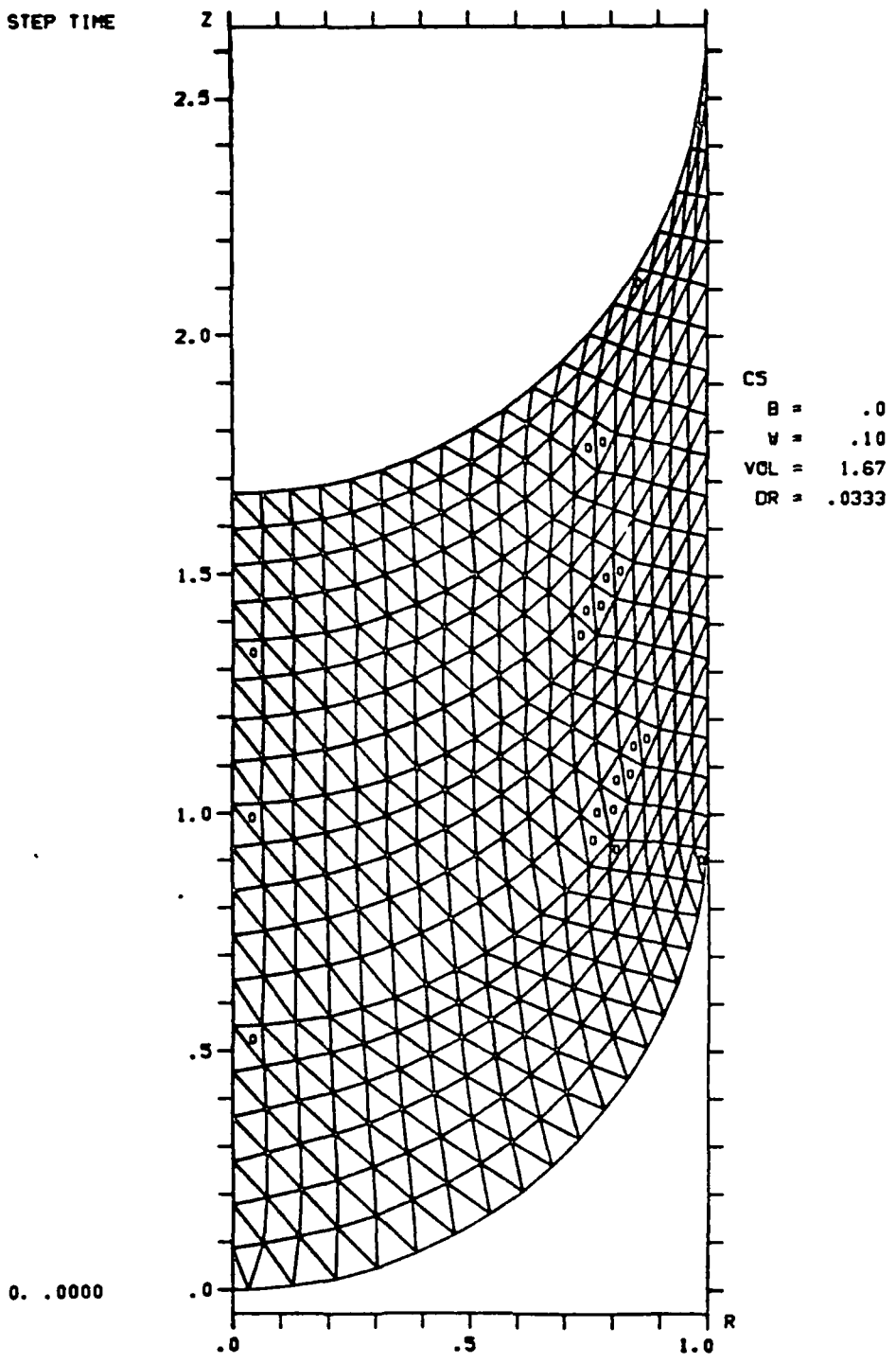

(a) Initial mesh used for B=0 cases.

Figure 3. Evolution of computing mesh for Case 5; $(B, W, r_o, V_o)=(0, .1, 1/10, 5\pi/3)$.

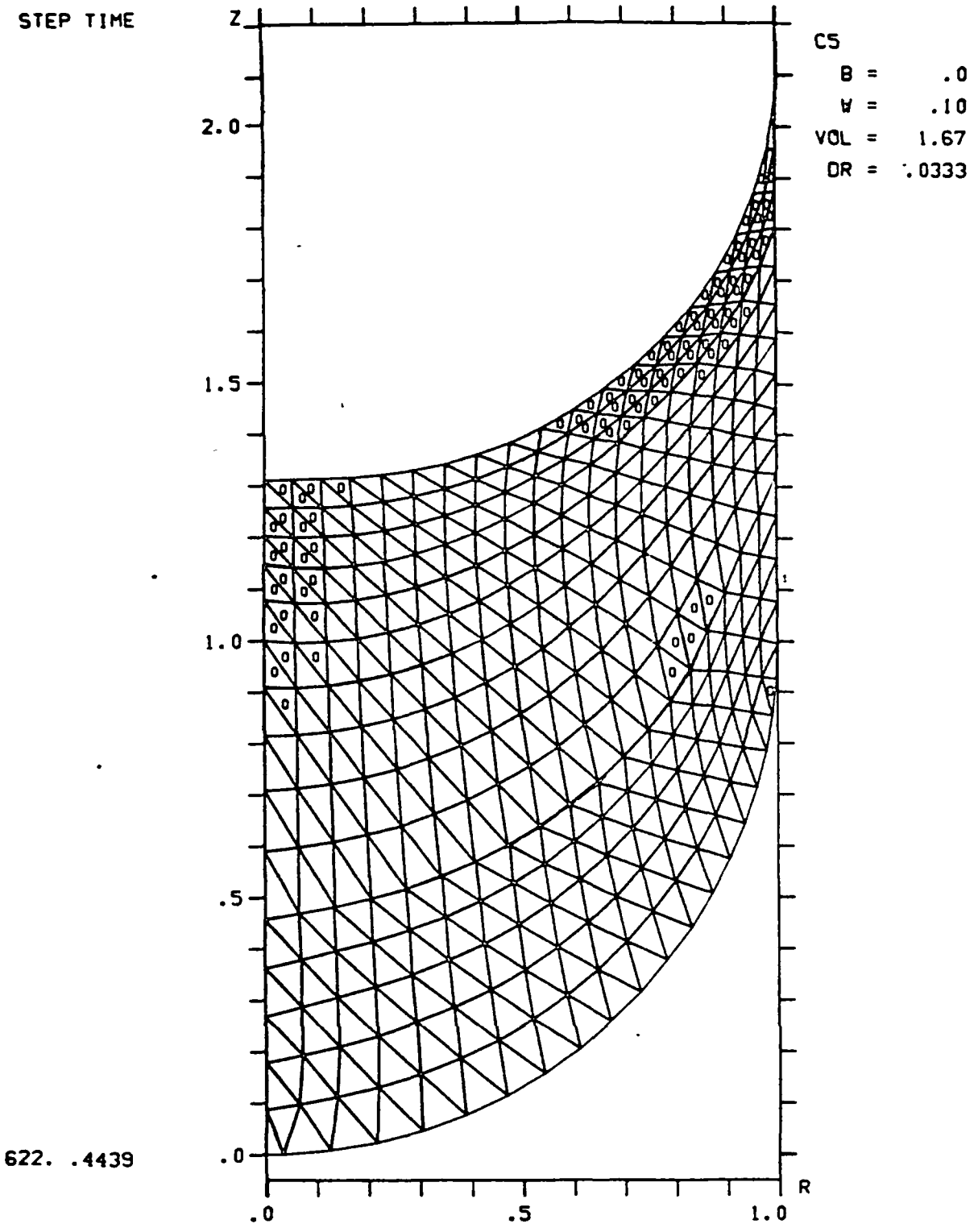

(b) Mesh at t=.4439.

Figure 3 (cont). Evolution of computing mesh for Case 5; $(B, W, r_o, V_o)=(0, .1, 1/10, 5\pi/3)$.

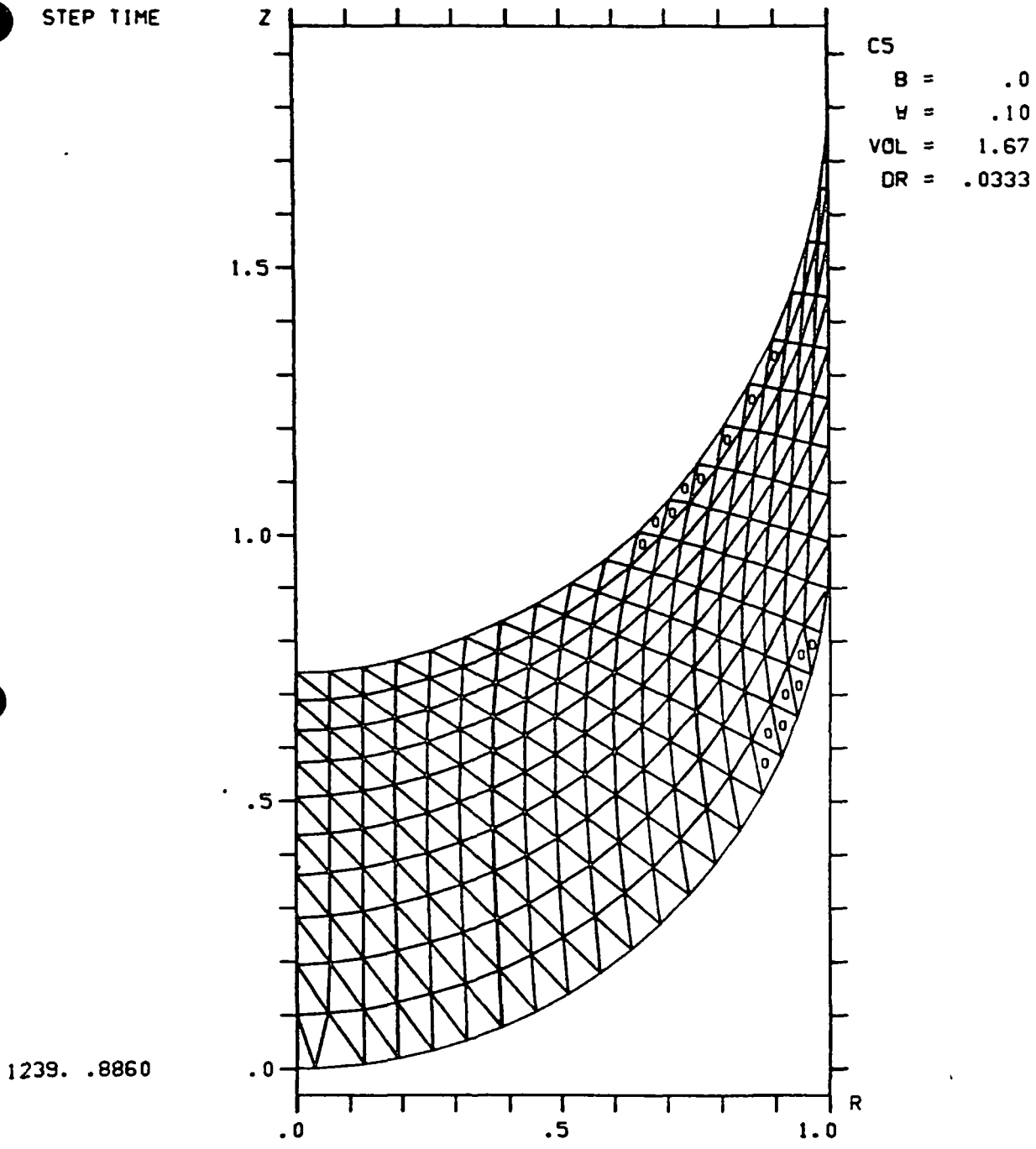

(c) Mesh at t=.8860.

Figure 3 (cont). Evolution of computing mesh for Case 5; $(B, W, r_o, V_o)=(0, .1, 1/10, 5\pi/3)$.

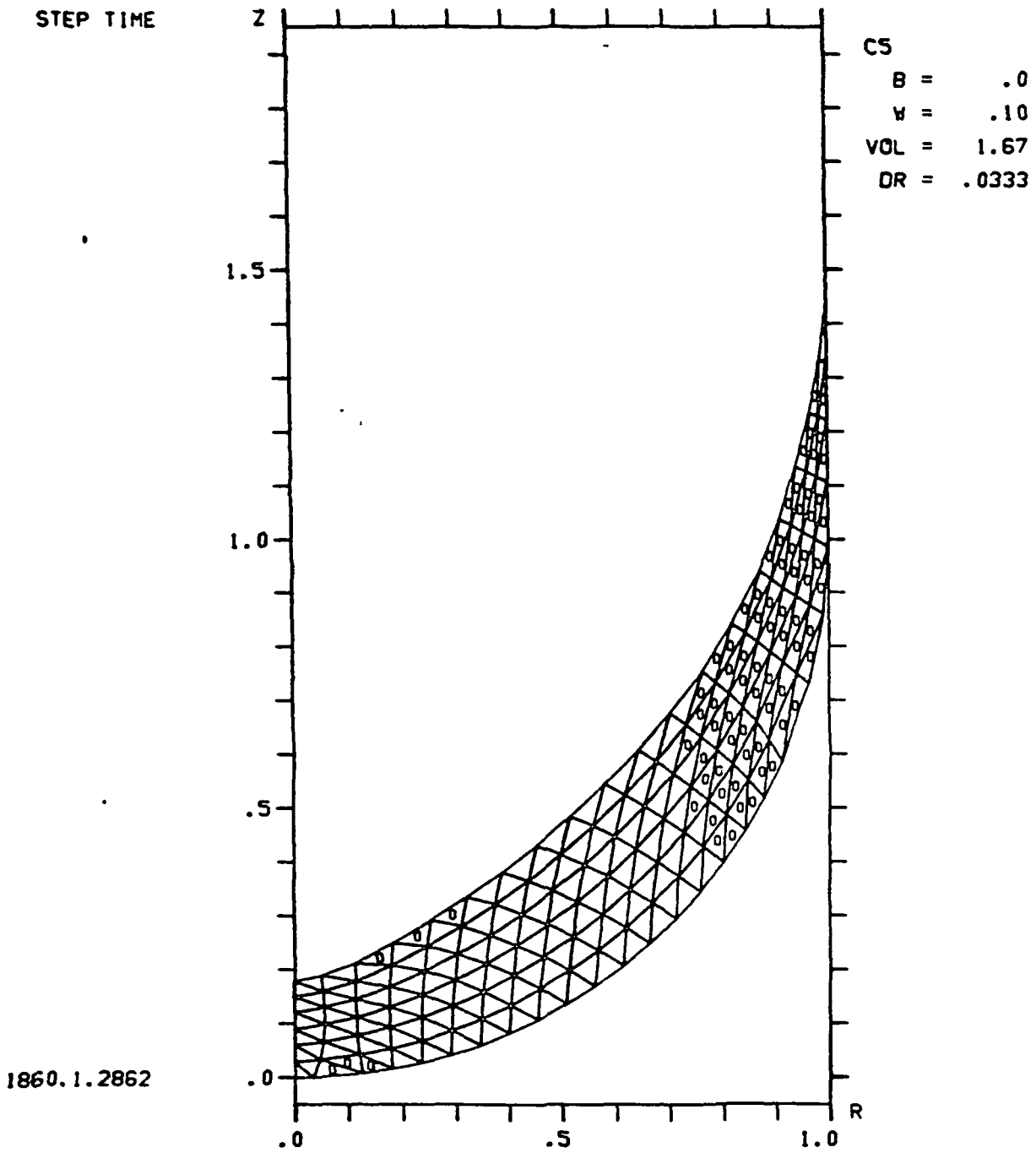

(d) Mesh at t=1.2862.

Figure 3 (cont). Evolution of computing mesh for Case 5; $(B, W, r_o, V_o) = (0, .1, 1/10, 5\pi/3)$.

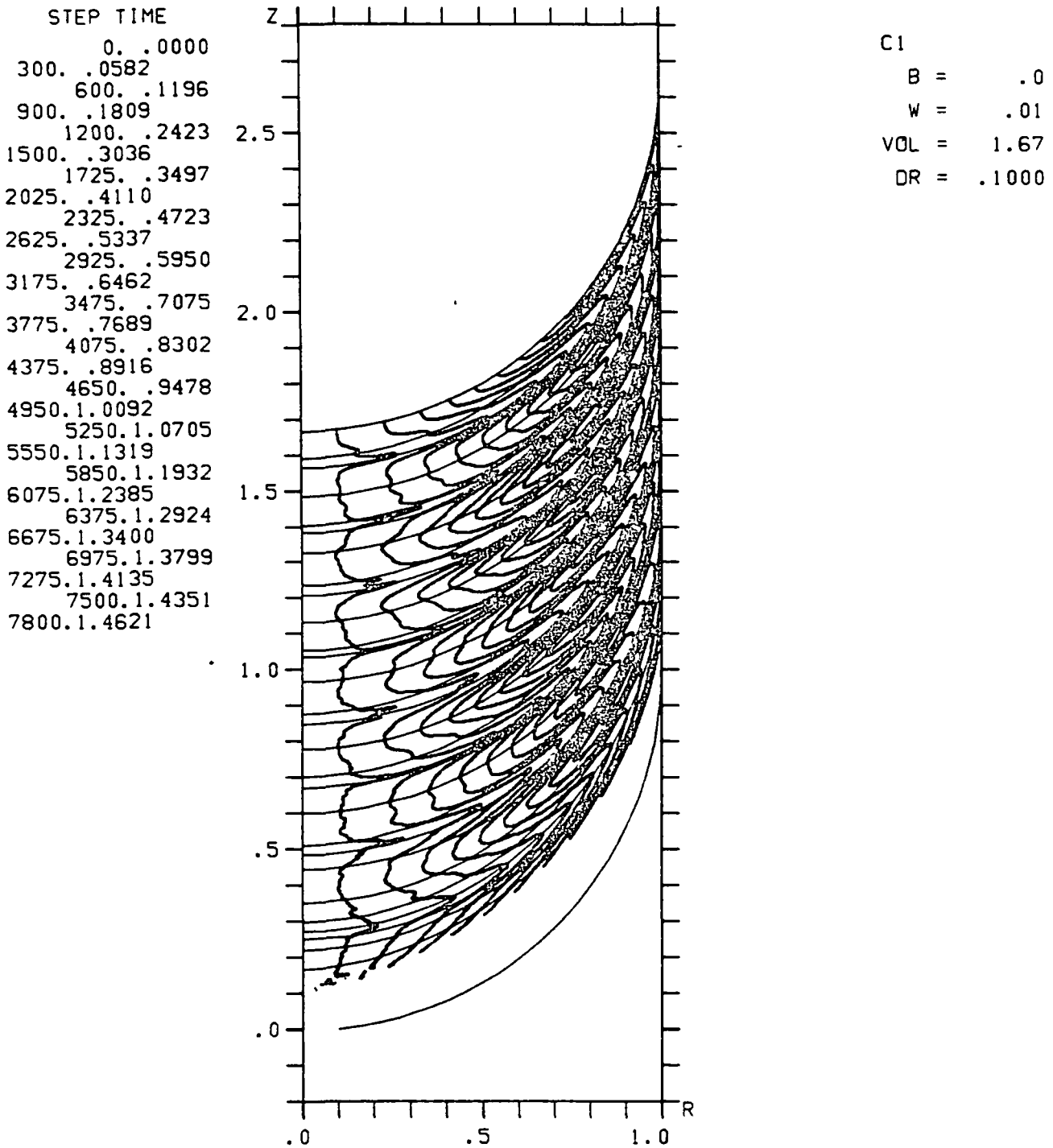

(a) Free surfaces and trajectories of free surface and streamline intersections.

Figure 4. Draining characteristics for Case 1; $(B, W, r_o, V_o)=(0, .01, 1/10, 5\pi/3)$.

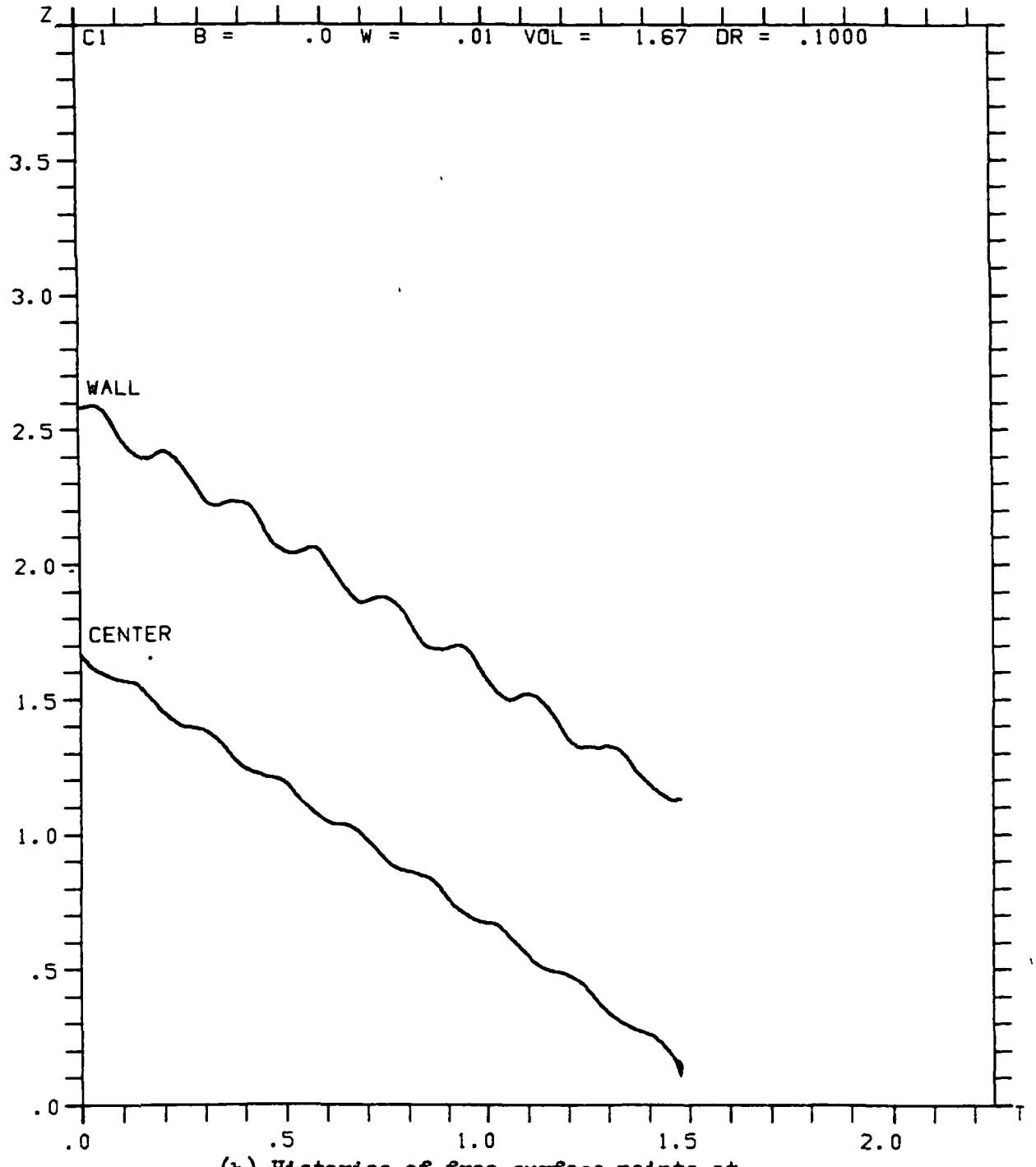

(b) Histories of free surface points at centerline and wall.

Figure 4 (cont). Draining characteristics for Case 1; $(B, W, r_o, V_o)=(0, .01, 1/10, 5\pi/3)$.

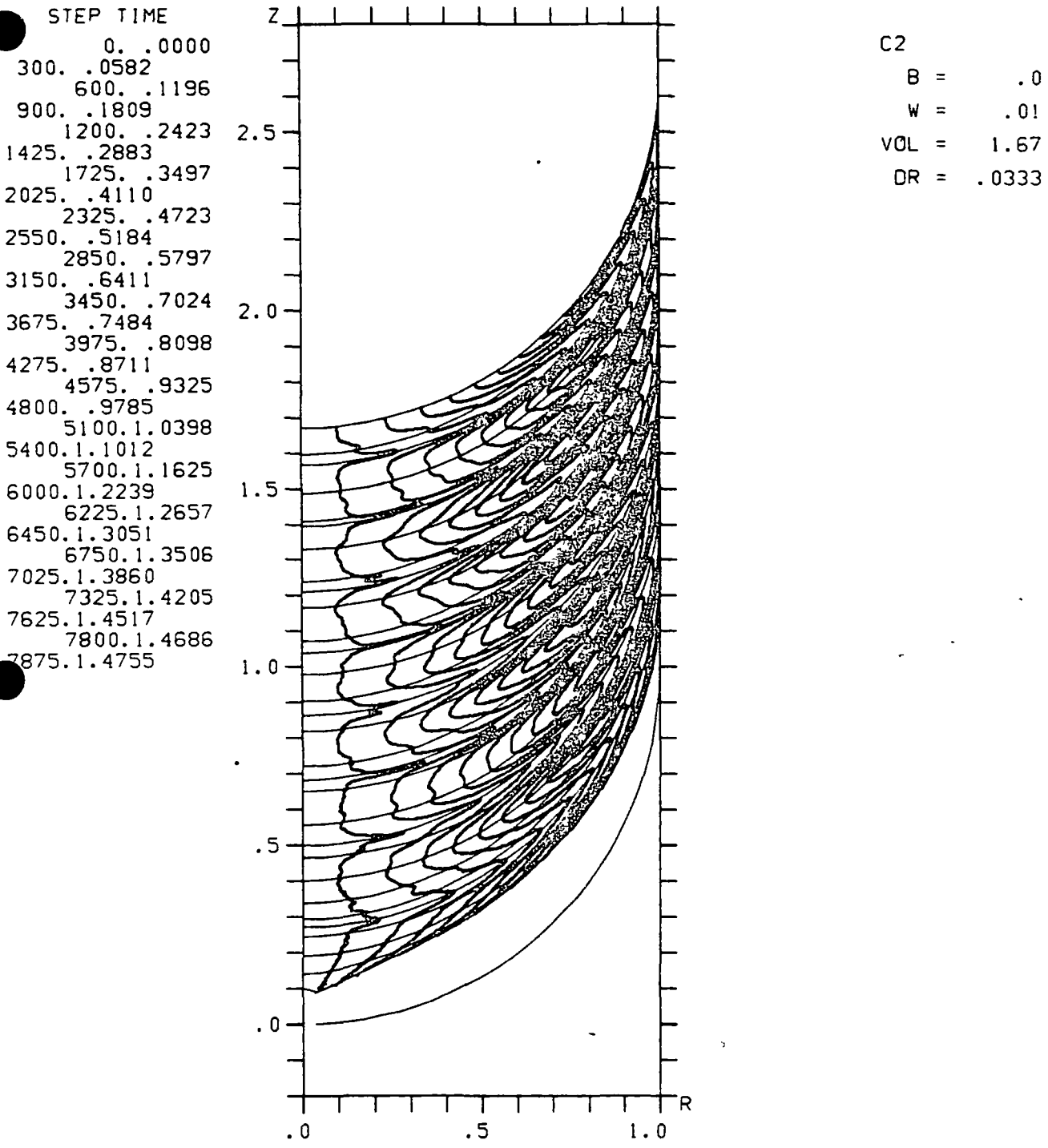

(a) Free surfaces and trajectories of free surface and streamline intersections.

Figure 5. Draining characteristics for Case 2; $(B, W, r_o, V_o) = (0, .01, 1/30, 5\pi/3)$.

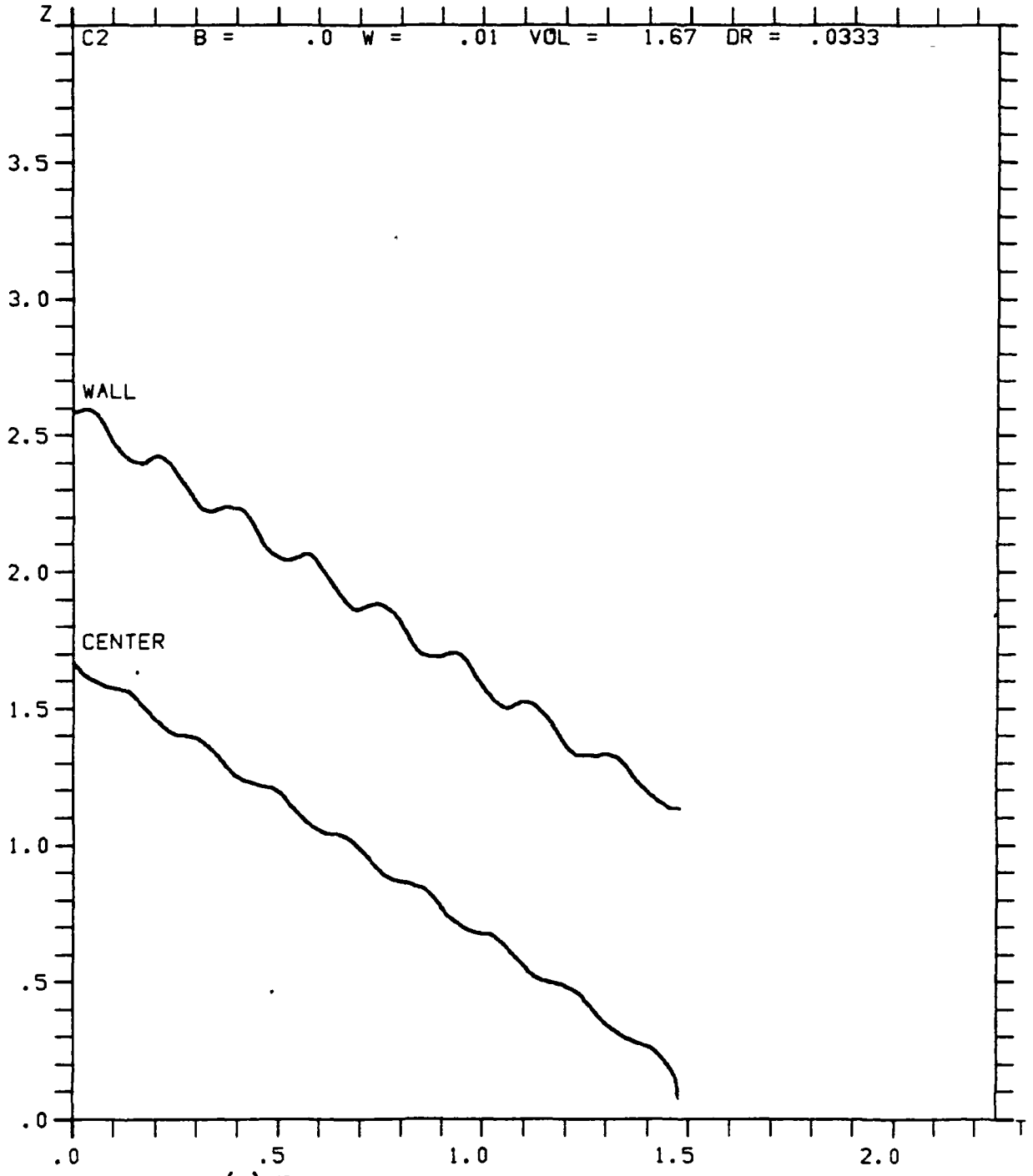

(b) Histories of free surface points at centerline and wall.

Figure 5 (cont). Draining characteristics for Case 2; $(B,W,r_o,V_o)=(0,.01,1/30,5\pi/3)$.

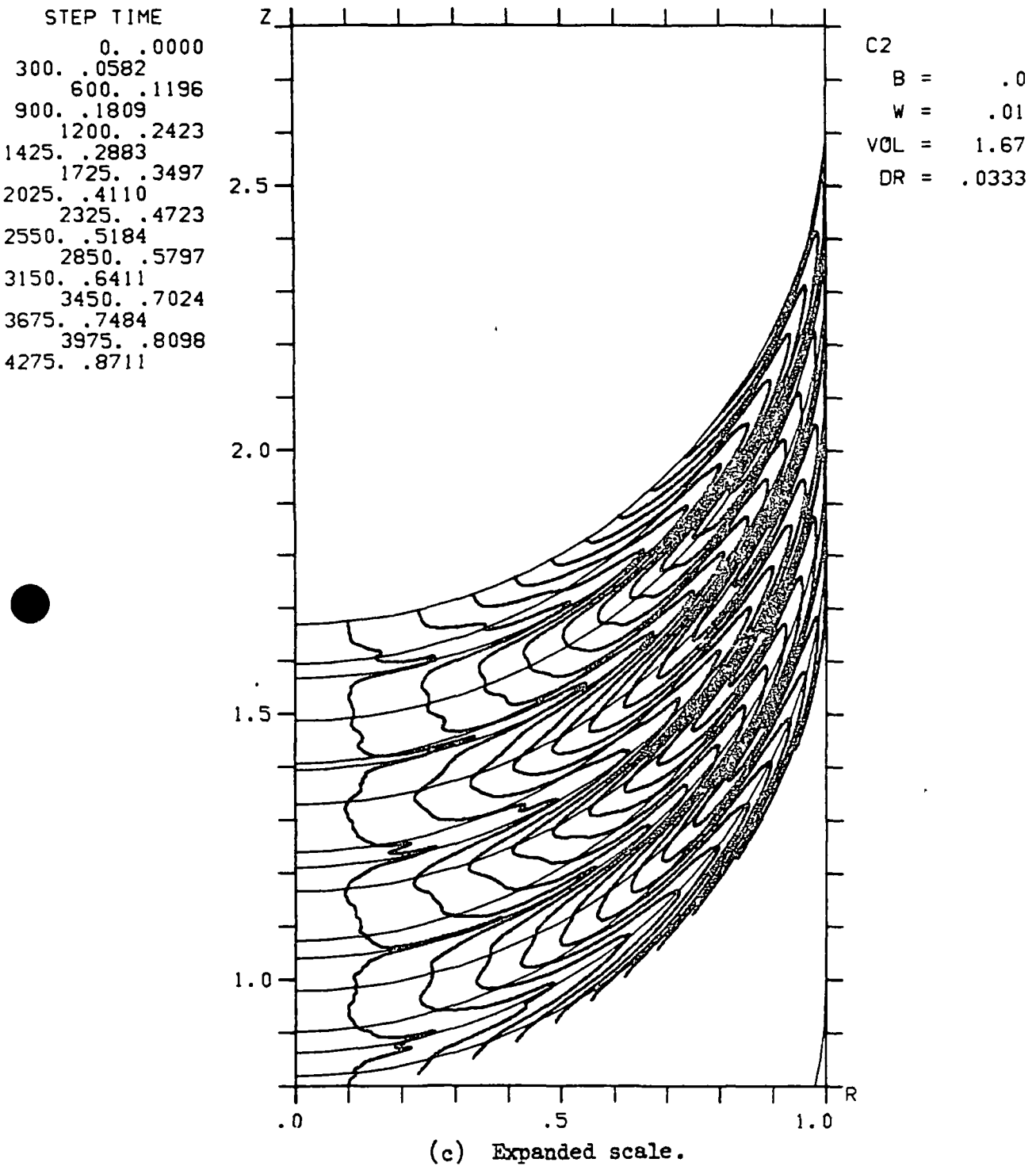

(c) Expanded scale.

Figure 5 (cont). Draining characteristics for Case 2; $(B, W, r_o, V_o) = (0, .01, 1/30, 5\pi/3)$.

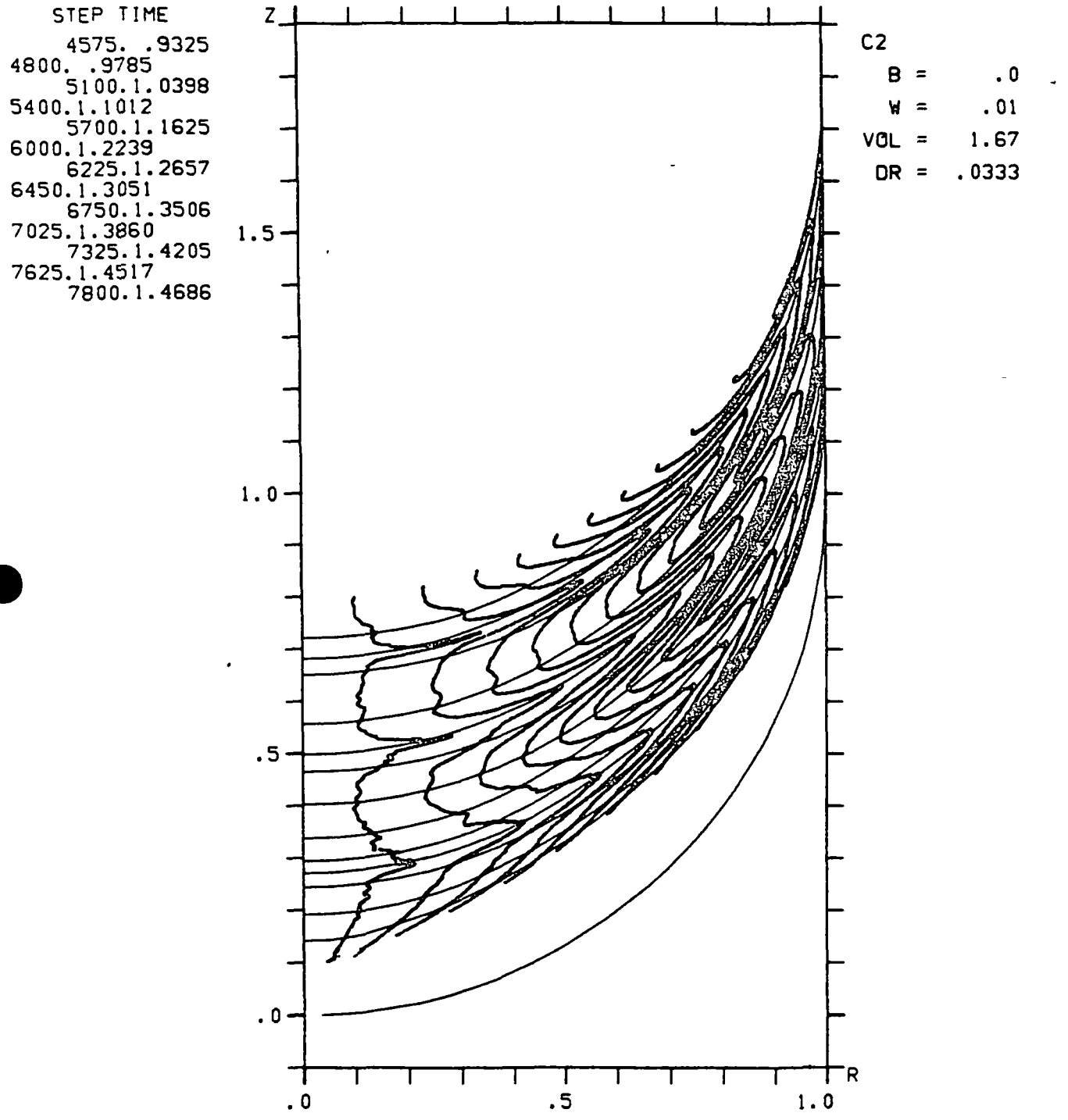

(d) Expanded scale.

Figure 5 (cont). Draining characteristics for Case 2; $(B, W, r_o, V_o) = (0, .01, 1/30, 5\pi/3)$.

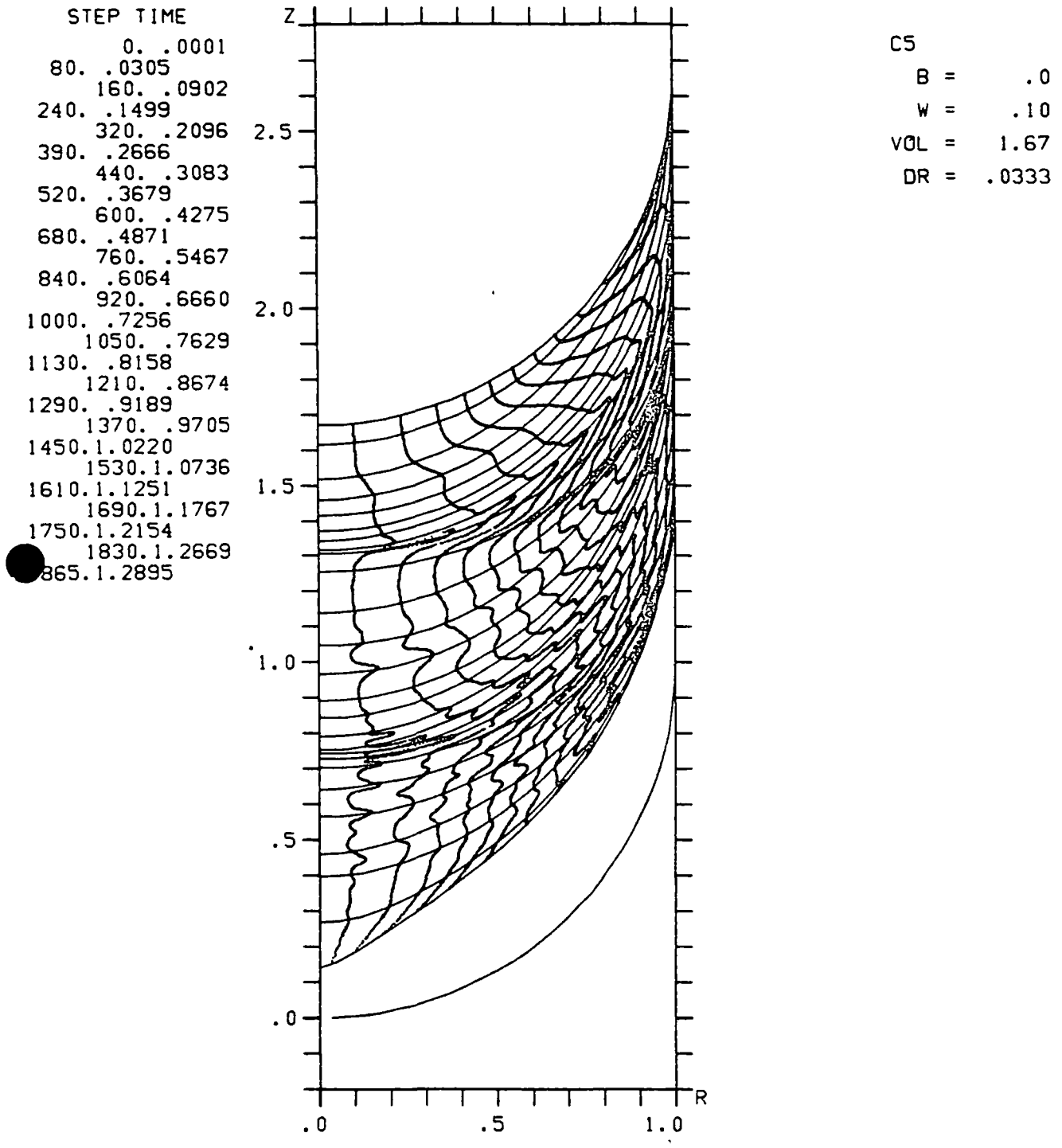

(a) Free surfaces and trajectories of free surface and streamline intersections.

Figure 6. Draining characteristics for Case 5; $(B, W, r_o, V_o) = (0, .1, 1/30, 5\pi/3)$.

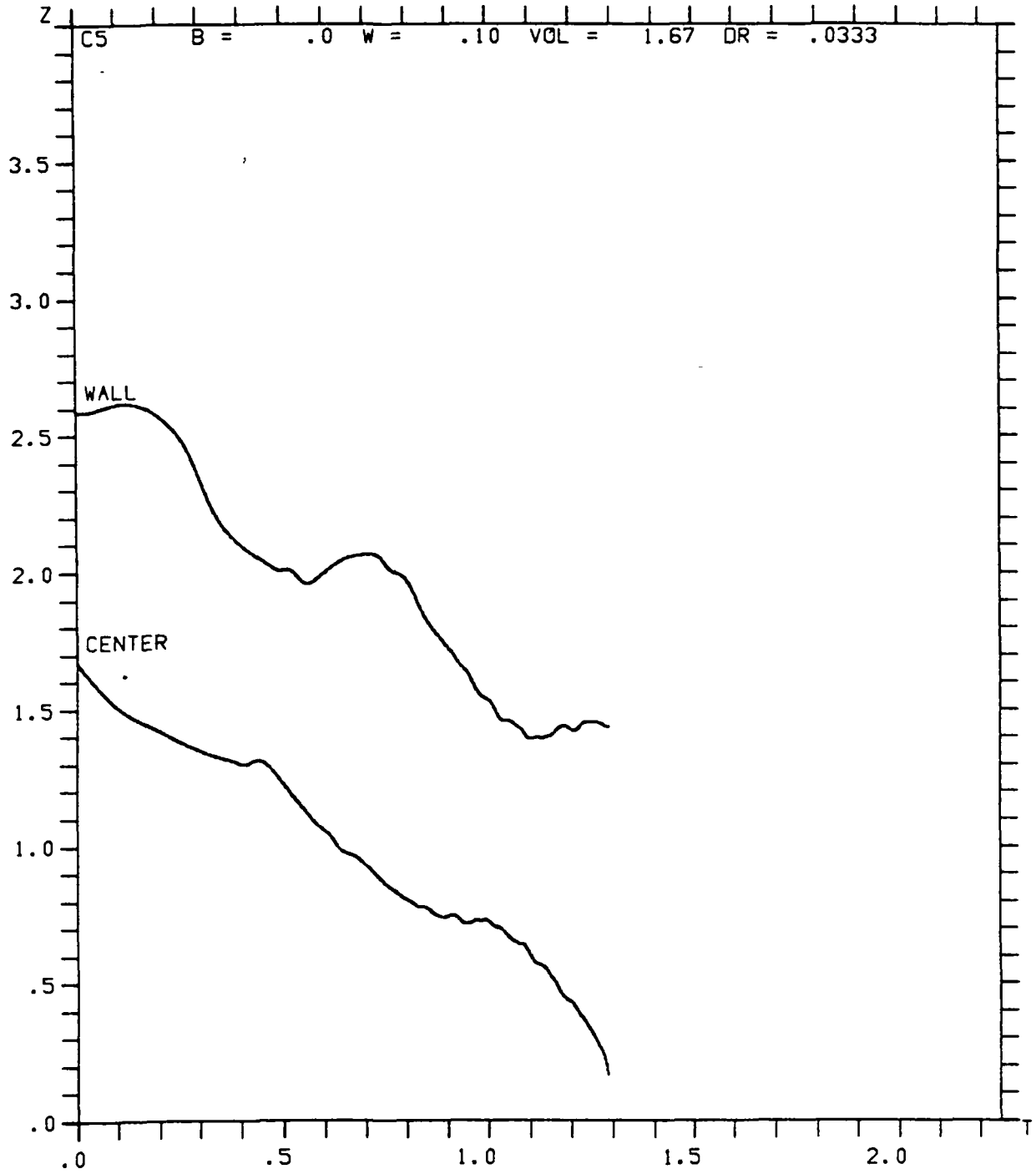

(b) Histories of free surface points at centerline and wall.

Figure 6 (cont). Draining characteristics for Case 5; $(B, W, r_o, V_o) = (0, .1, 1/30, 5\pi/3)$.

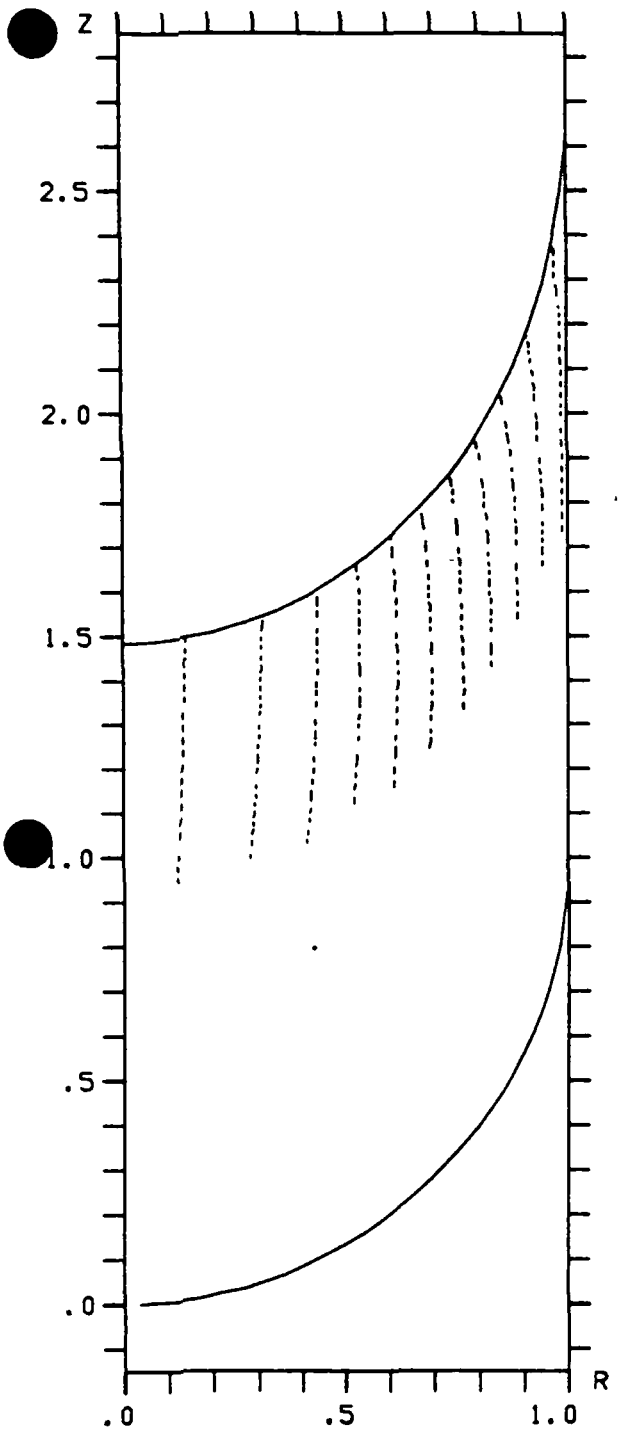

(c) Streamlines at t=.1201 showing maximum rise at wall.

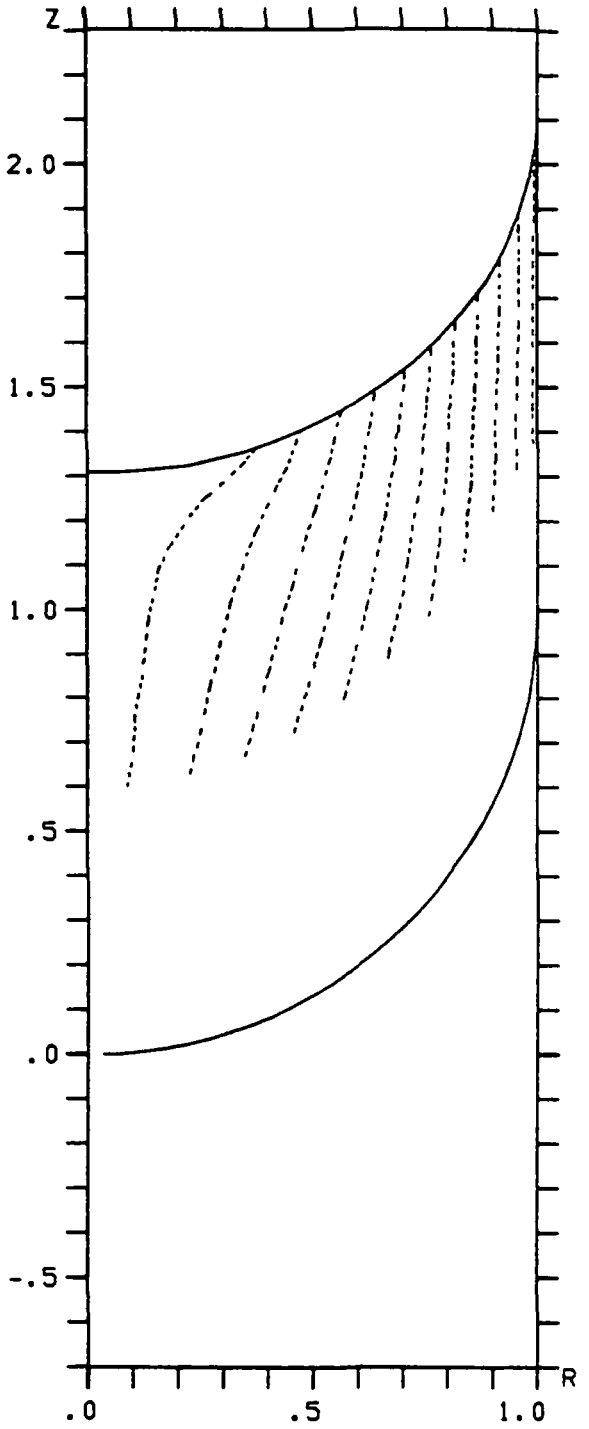

(d) Streamlines at t=.4275 near maximum of first major wave showing large excursion of the .98 streamline and continued acceleration along the remainder of free surface.

Figure 6 (cont). Draining characteristics for Case 5; $(B, W, r_o, V_o)=(0, .1, 1/30, 5\pi/3)$.

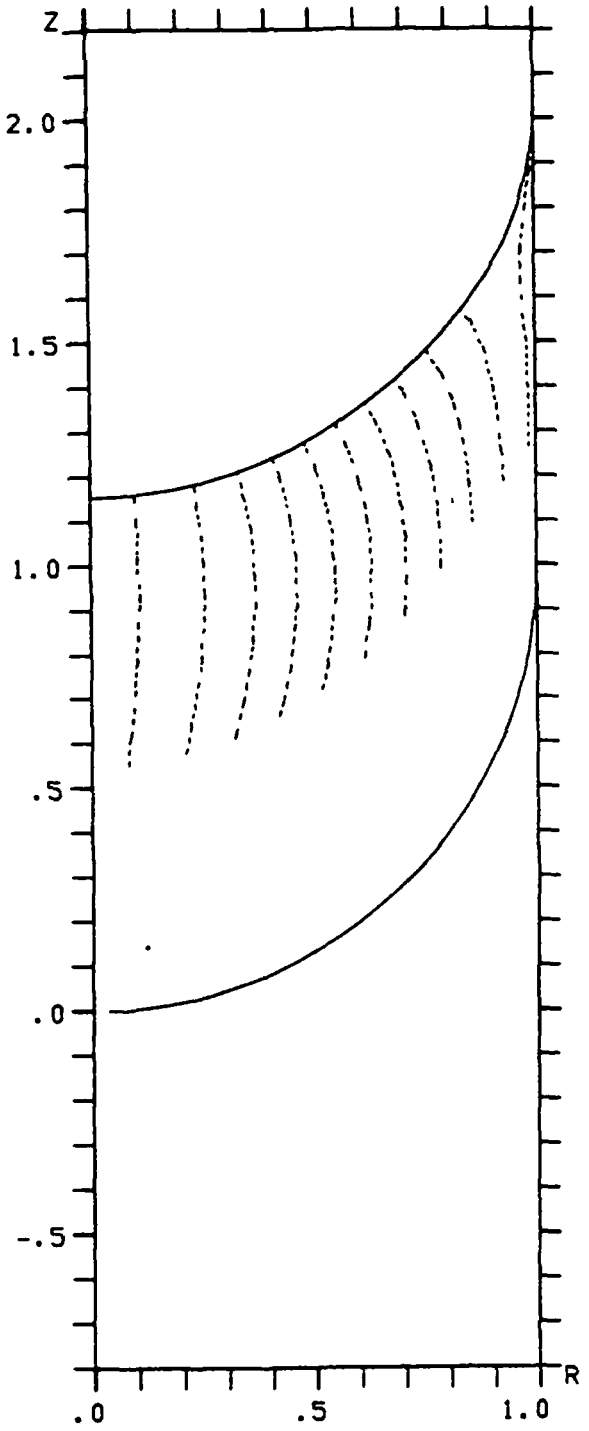

(e) Streamlines at t=.5393 resembling initial conditions (cf. Figure 7(c)) except at the wall.

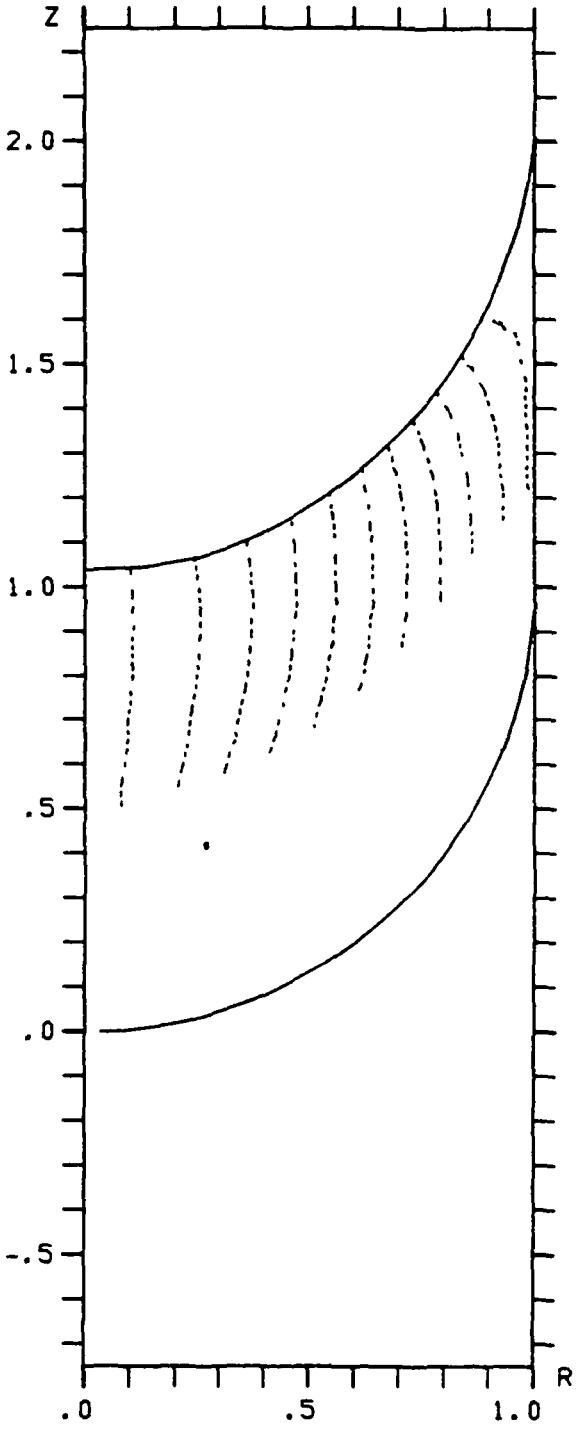

(f) Streamlines at t=.6138 near beginning of second wave showing the .02 streamline with curvature exceeding its initial curvature (cf. Figure 7(c)).

Figure 6 (cont). Draining characteristics for Case 5; $(B, W, r_o, V_o) = (0, .1, 1/30, 5\pi/3)$.

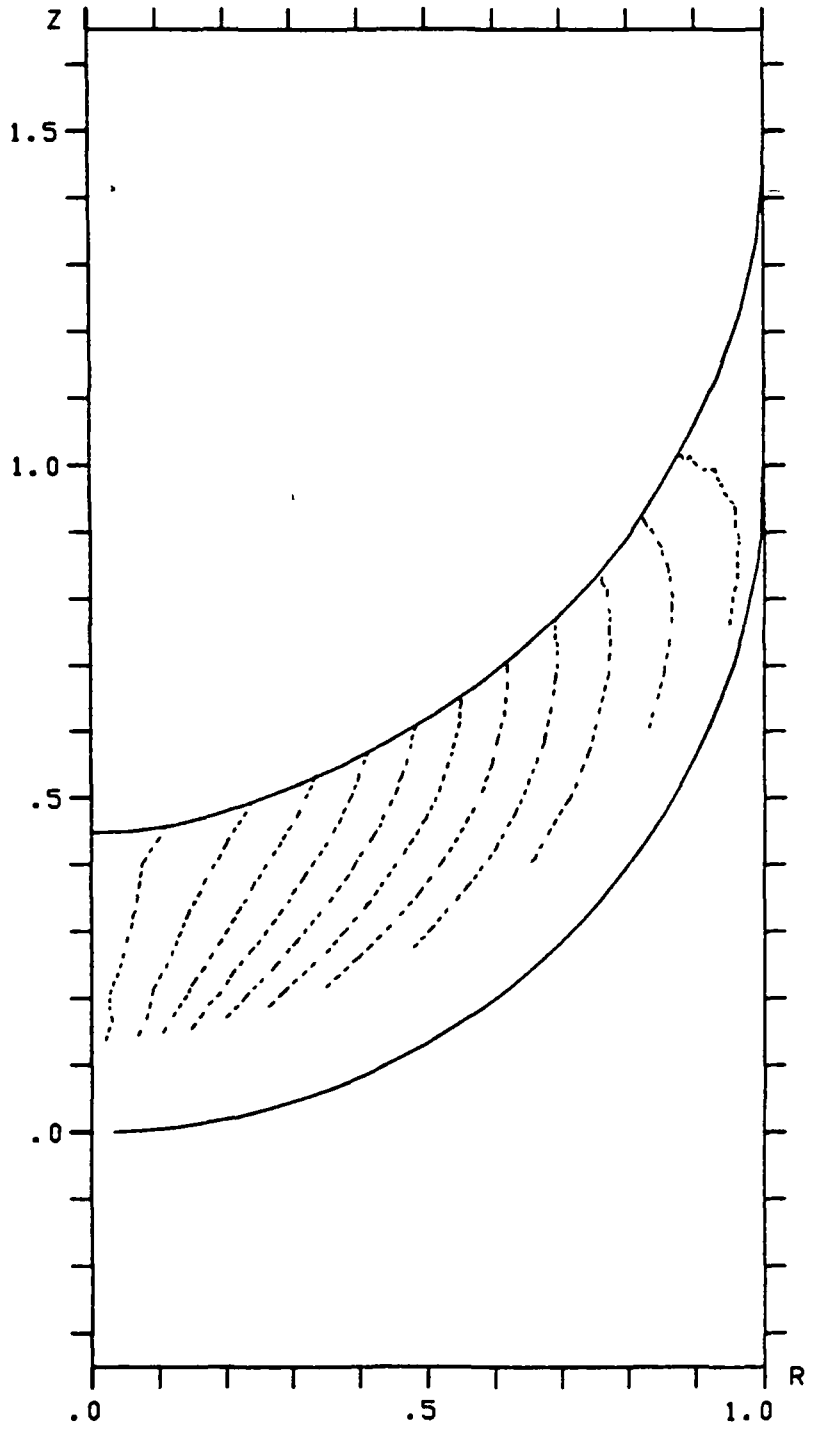

(g) Streamlines at t=1.1831 near possible beginning of third major wave showing very curved streamlines adjacent to wall (cf. Figure 6(f)).

Figure 6 (cont). Draining characteristics for Case 5; $(B, W, r_o, V_o)=(0, .1, 1/30, 5\pi/3)$.

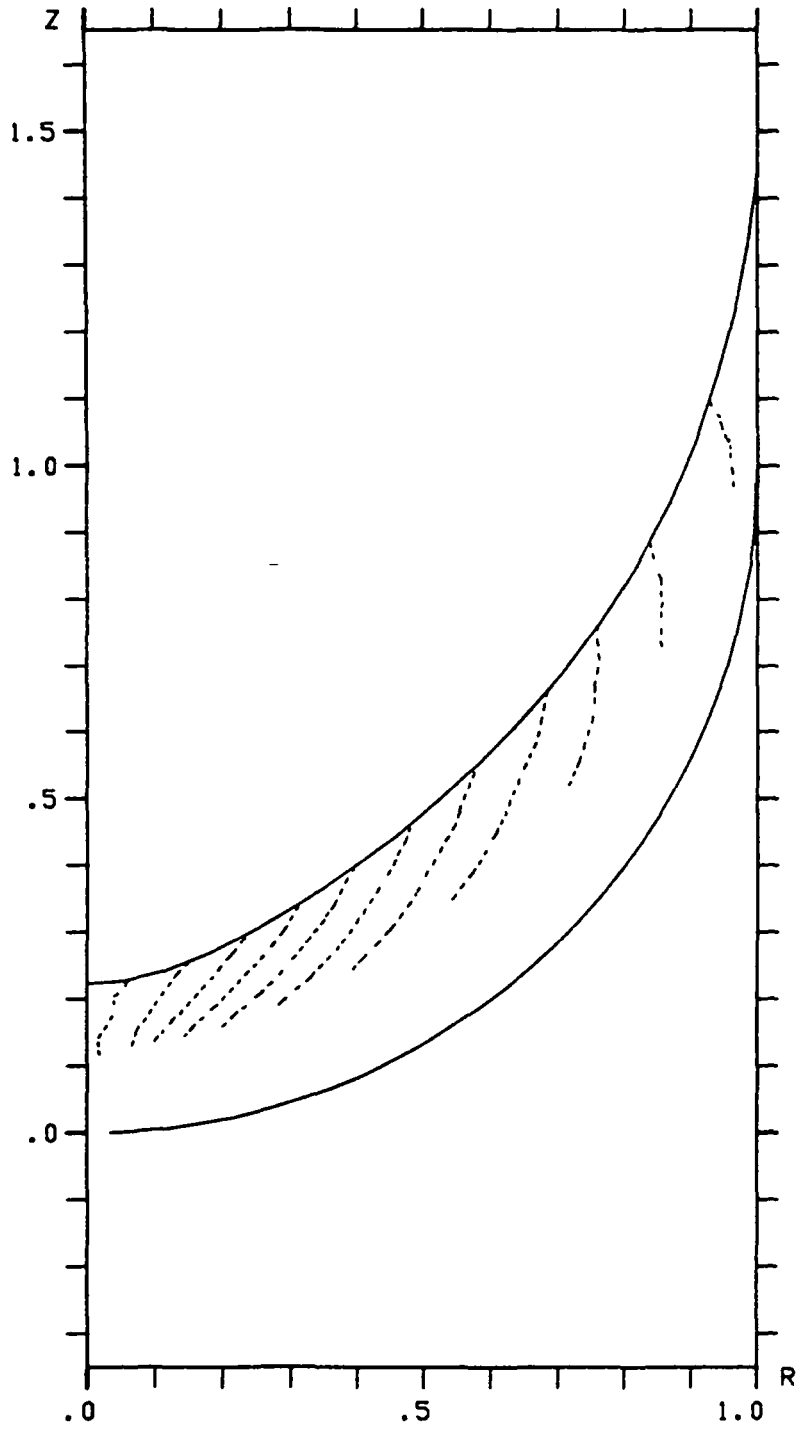

(h) Terminal streamline pattern at t=1.2798.

Figure 6 (cont). Draining characteristics for Case 5; $(B, W, r_o, V_o)=(0, .1, 1/30, 5\pi/3)$.

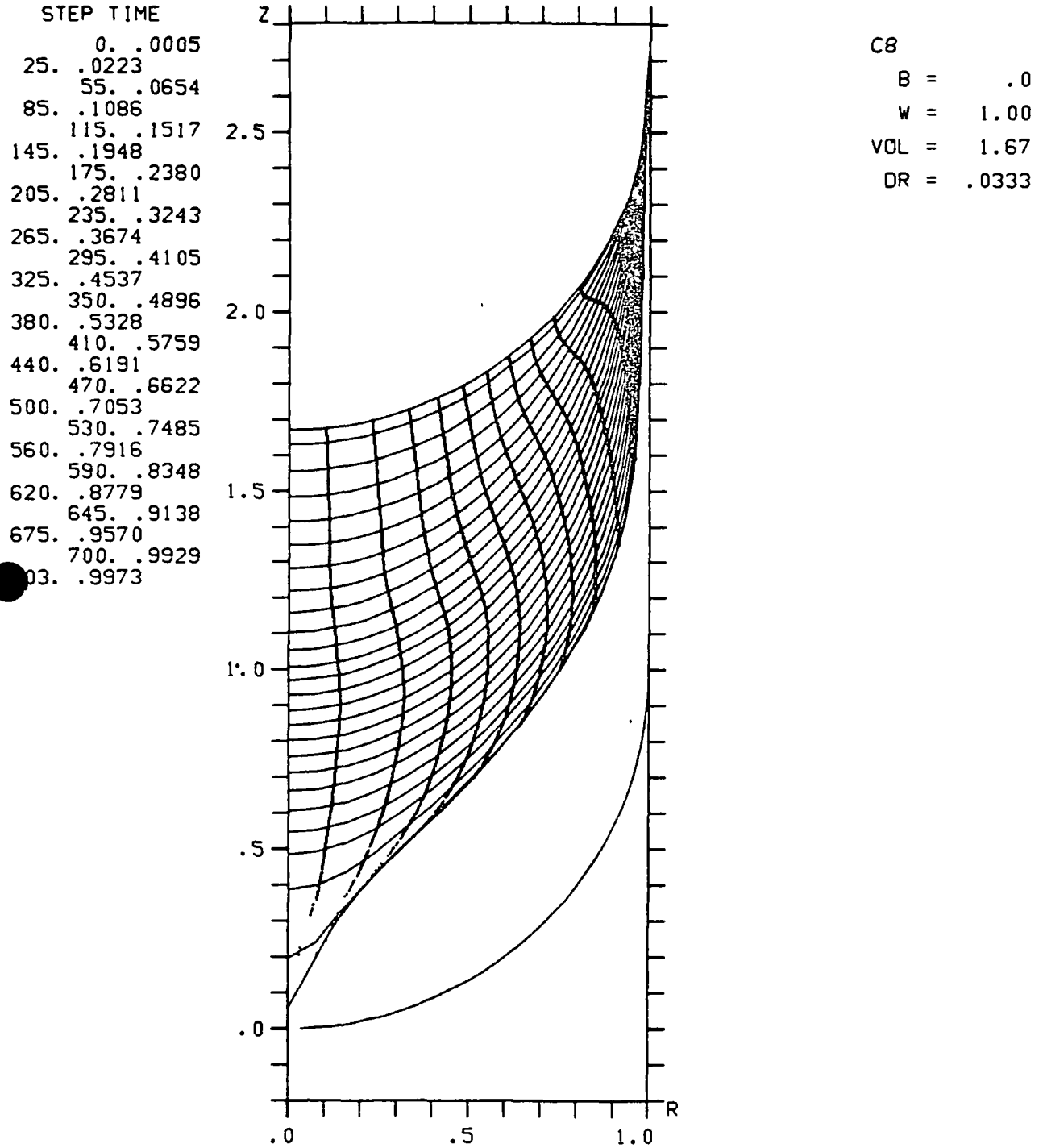

(a) Free surfaces and trajectories of free surface and streamline intersections.

Figure 7. Draining characteristics for Case 8; $(B, W, r_o, V_o) = (0, 1, 1/30, 5\pi/3)$.

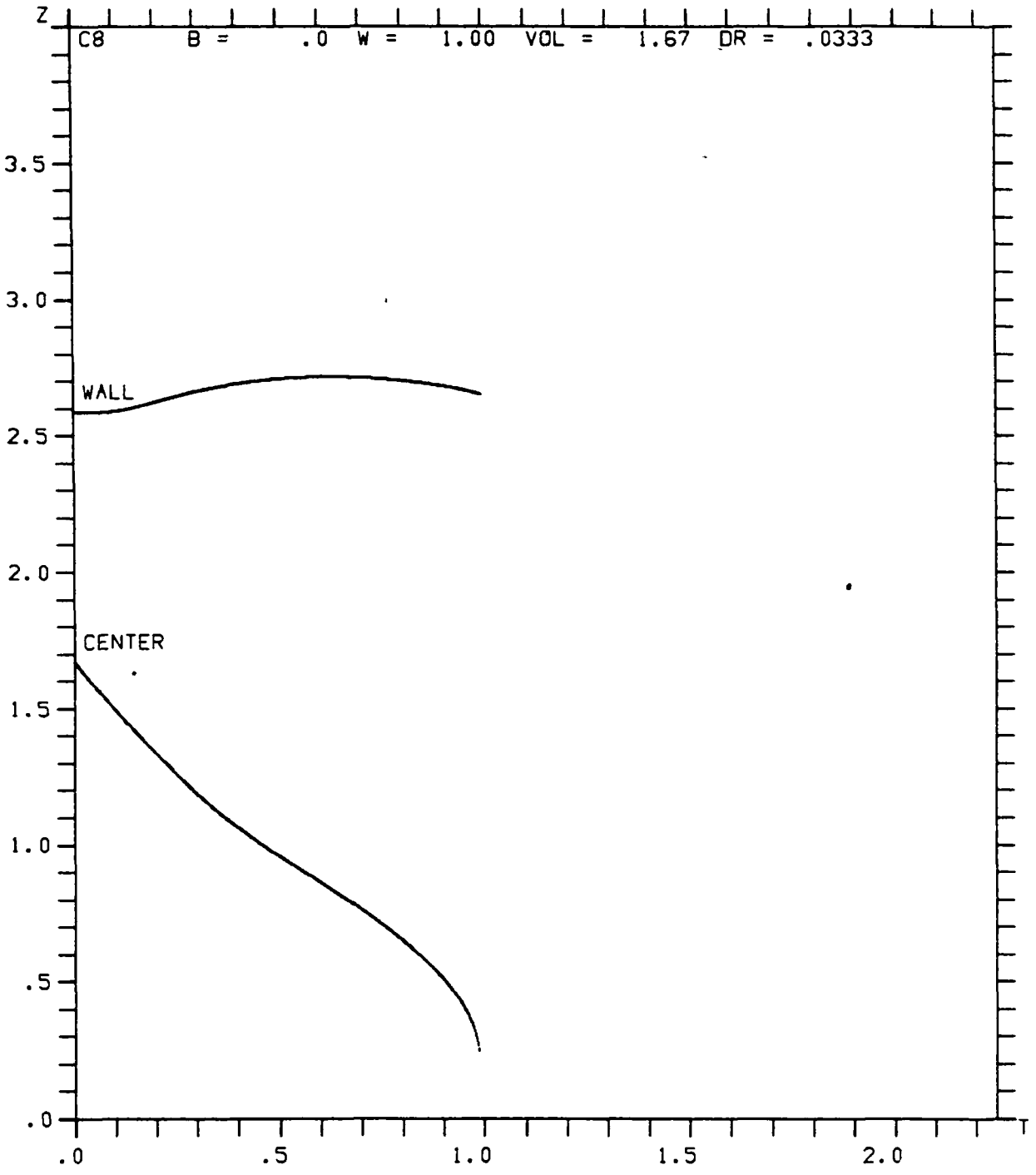

(b) Histories of free surface points at centerline and wall.

Figure 7 (cont). Draining characteristics for Case 8; $(B, W, r_o, V_o) = (0, 1, 1/30, 5\pi/3)$.

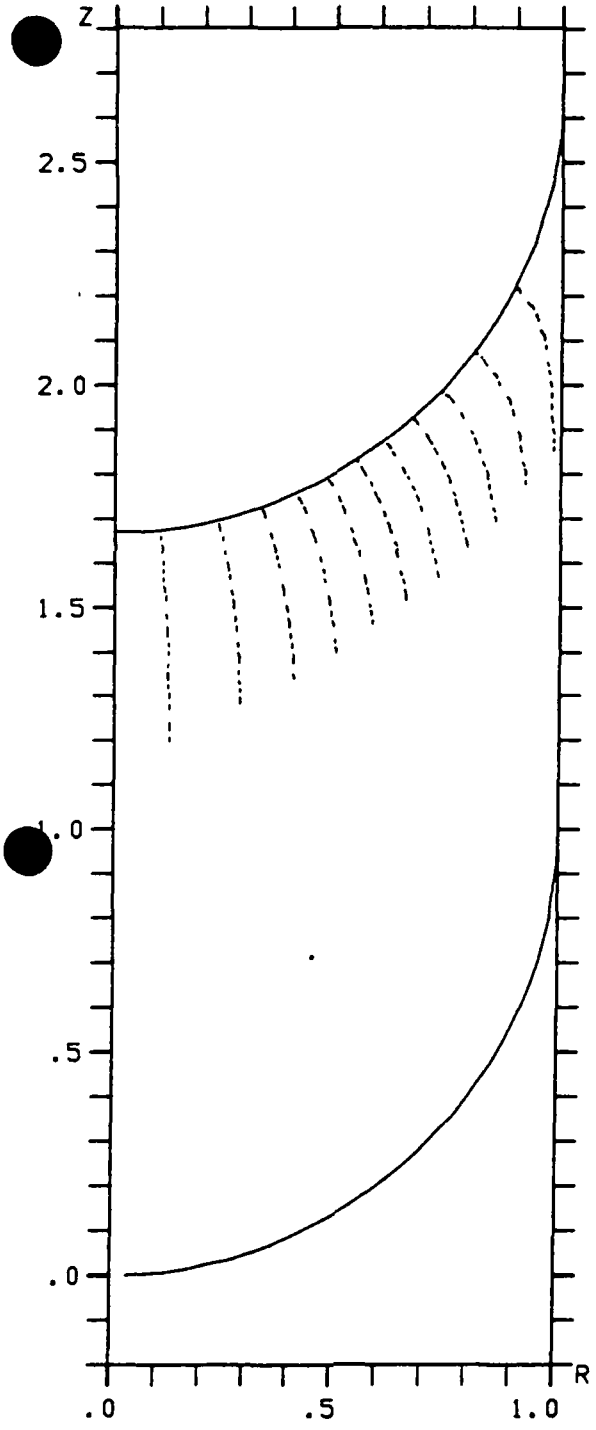

(c) Initial streamlines and spherical free surface.

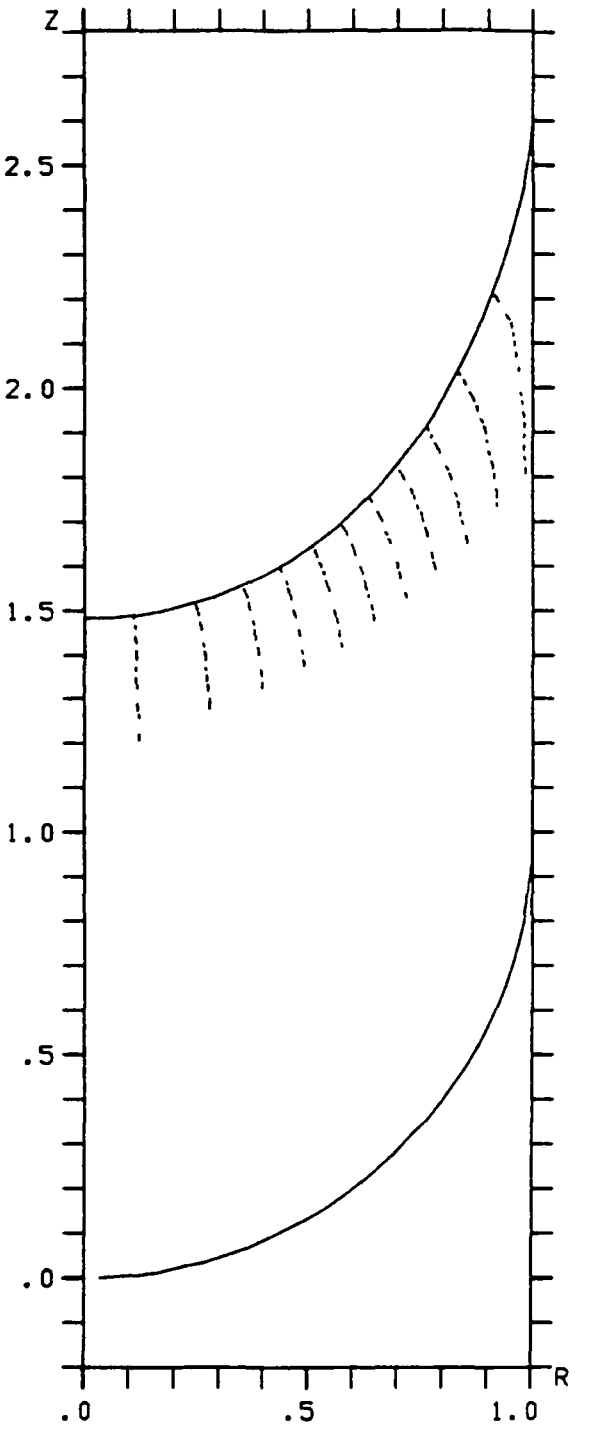

(d) Streamlines at t=.1086, when free surface is dropping at initial rate (cf. Figure 7(b)), showing that center is still spherical.

Figure 7 (cont). Draining characteristics for Case 8; $(B, W, r_o, V_o) = (0, 1, 1/30, 5\pi/3)$.

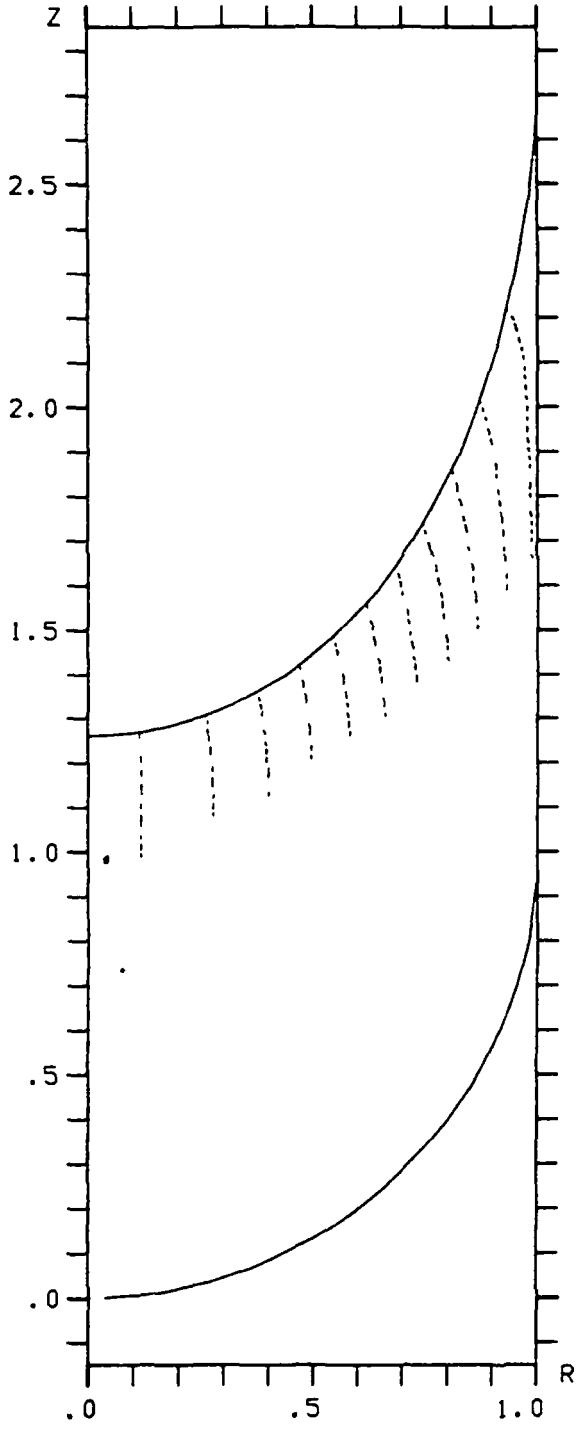

(e) Streamlines at t=.2524 as center begins to decelerate.

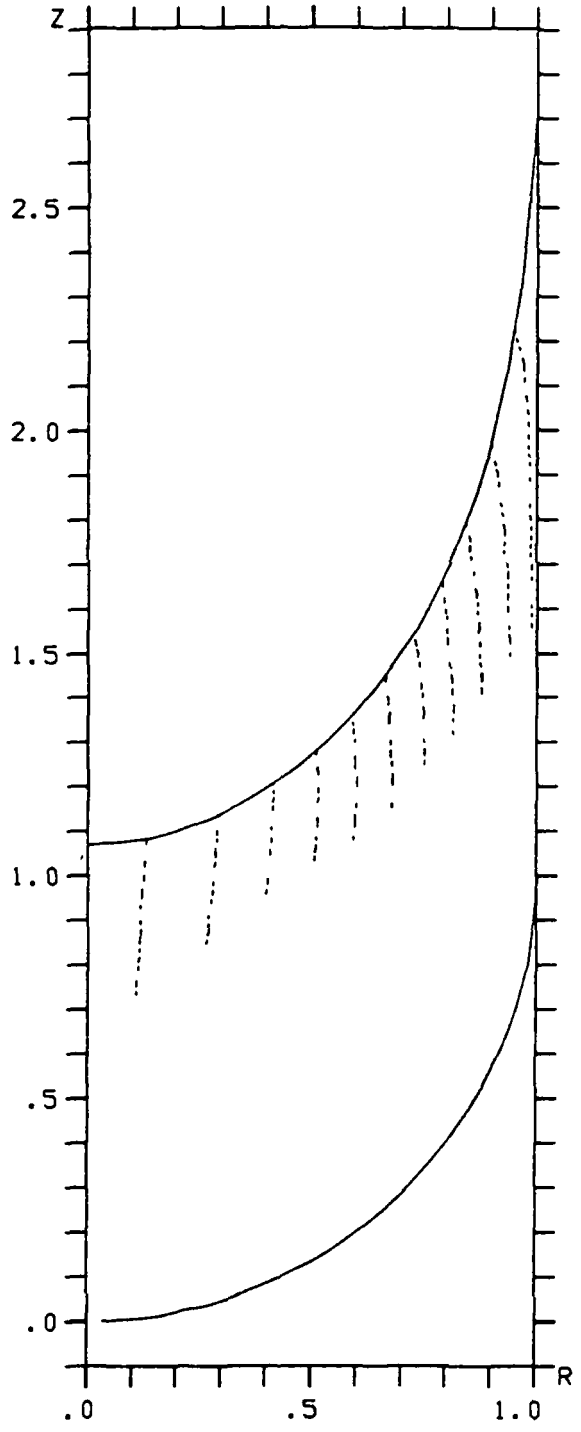

(f) Streamlines at t=.3962 showing developing velocity component along free surface.

Figure 7 (cont). Draining characteristics for Case 8; $(B, W, r_o, V_o)=(0, 1, 1/30, 5\pi/3)$.

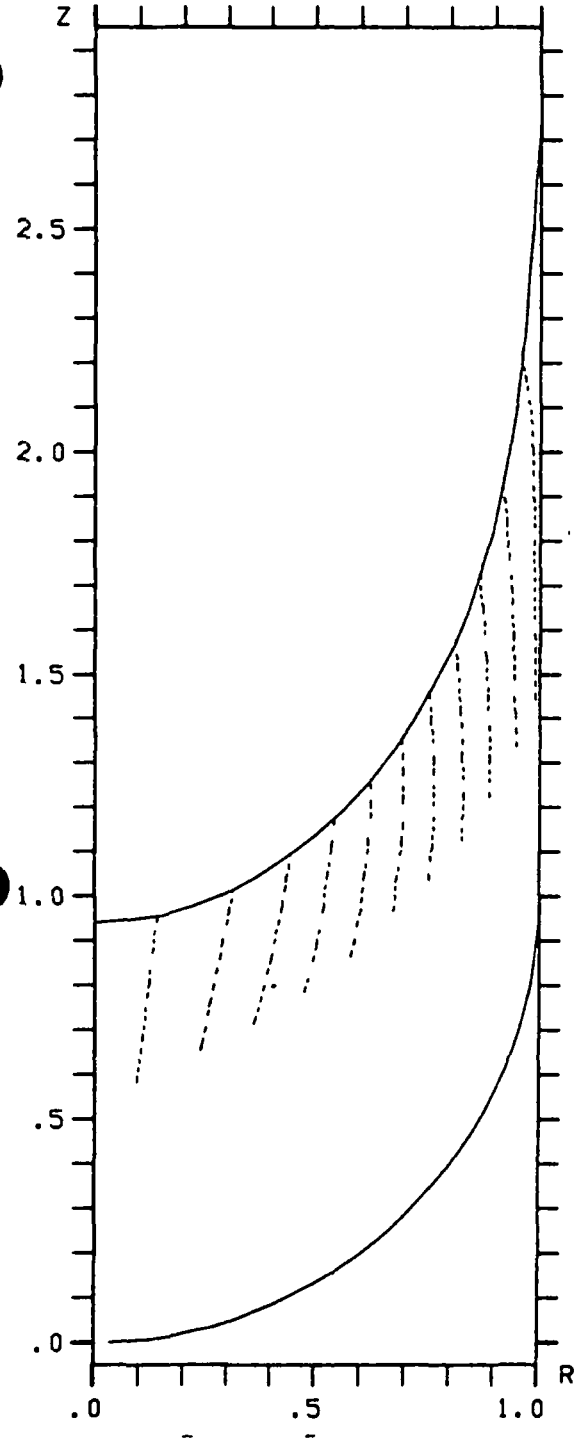

(g) Streamlines at t=.5184 near maximum of wave.

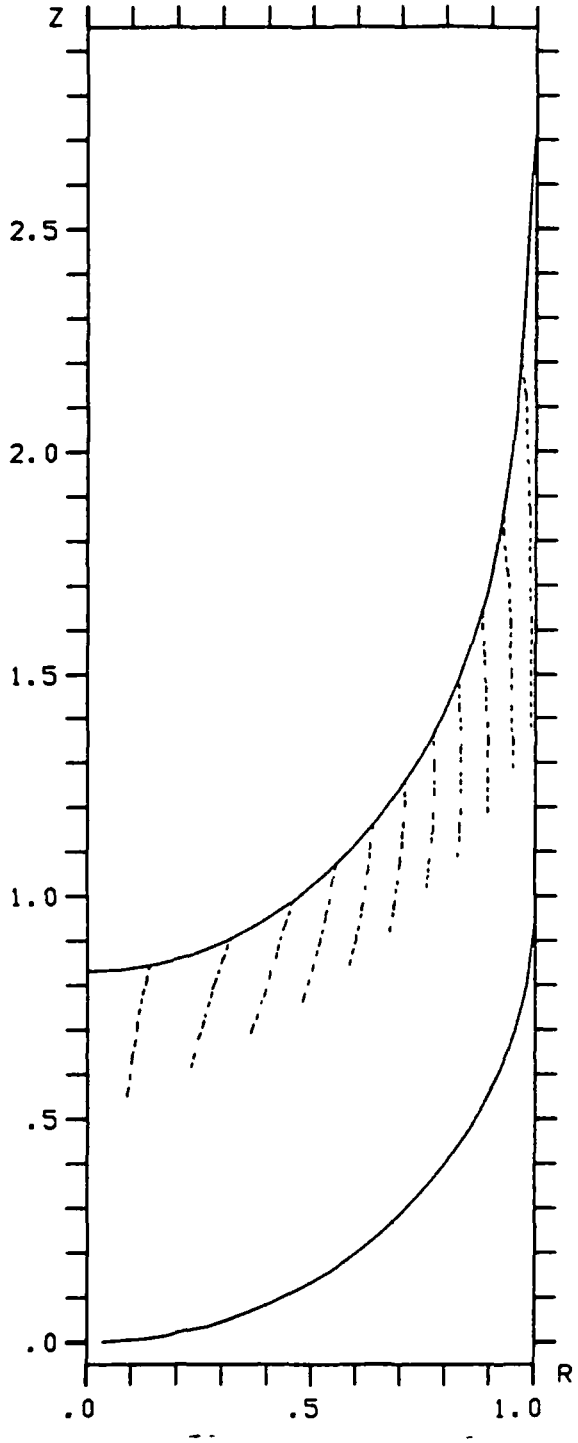

(h) Streamlines at t=.6334 just after wall begins to fall. Center line velocity is again nearly constant (cf. Figure 7(b)).

Figure 7 (cont). Draining characteristics for Case 8; $(B, W, r_o, V_o) = (0, 1, 1/30, 5\pi/3)$.

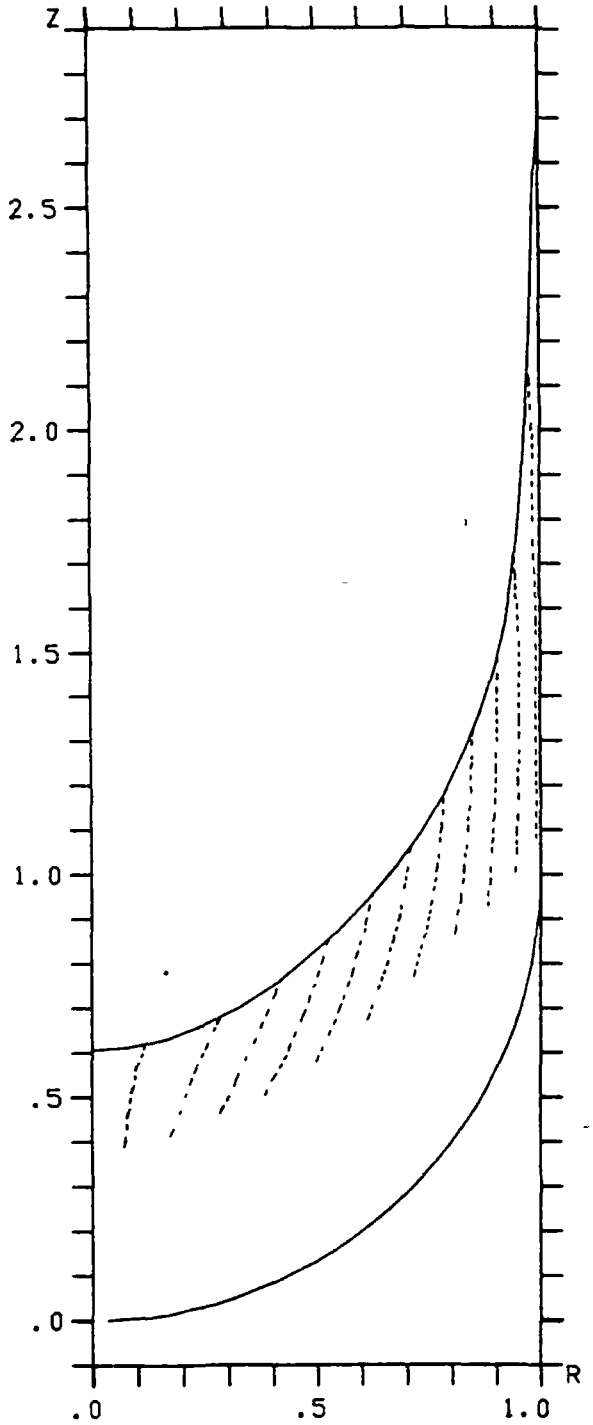

(i) Streamlines at t=.8348 as center line begins to accelerate (cf. Figure 7(b)).

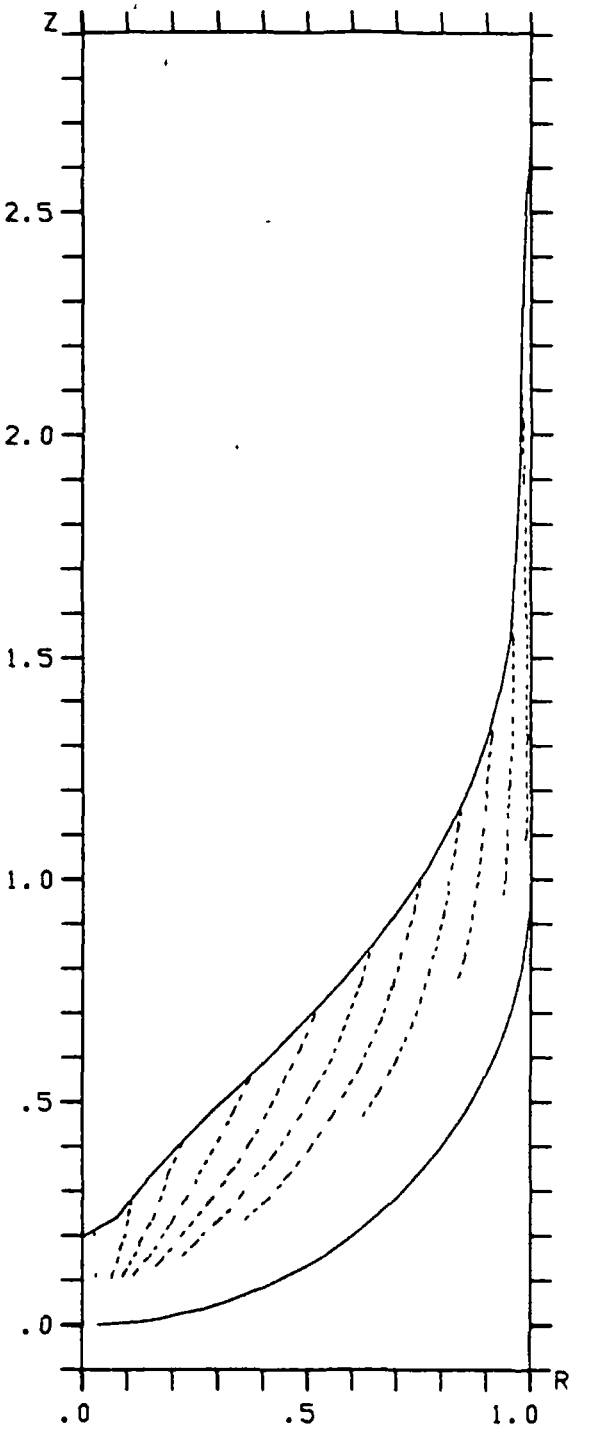

(j) Terminal streamline pattern at t=.9929.

Figure 7 (cont). Draining characteristics for Case 8; $(B, W, r_o, V_o)=(0, 1, 1/30, 5\pi/3)$.

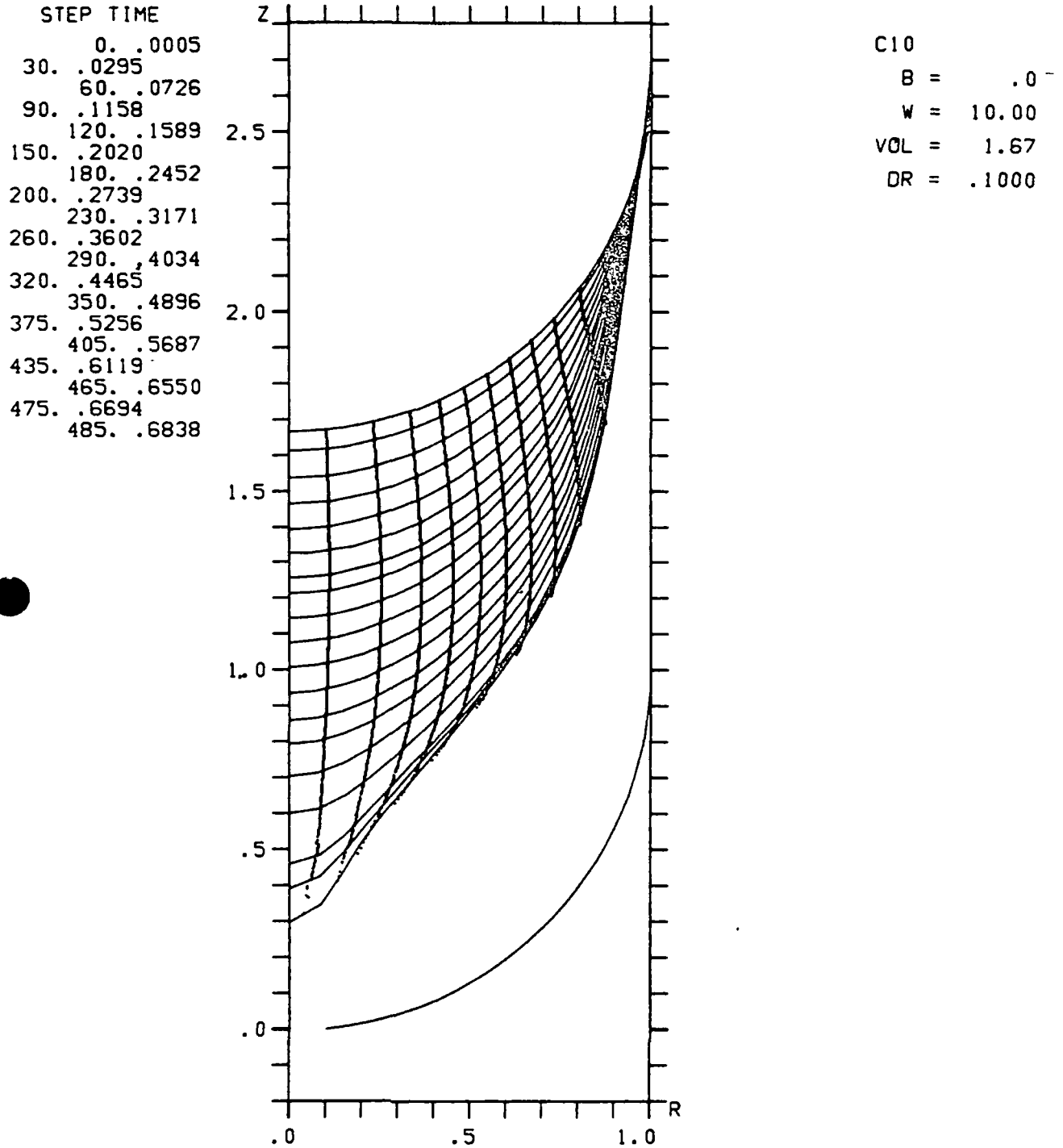

(a) Free surfaces and trajectories of free surface and streamline intersections.

Figure 8. Draining characteristics for Case 10; $(B, W, r_o, V_o) = (0, 10, 1/10, 5\pi/3)$.

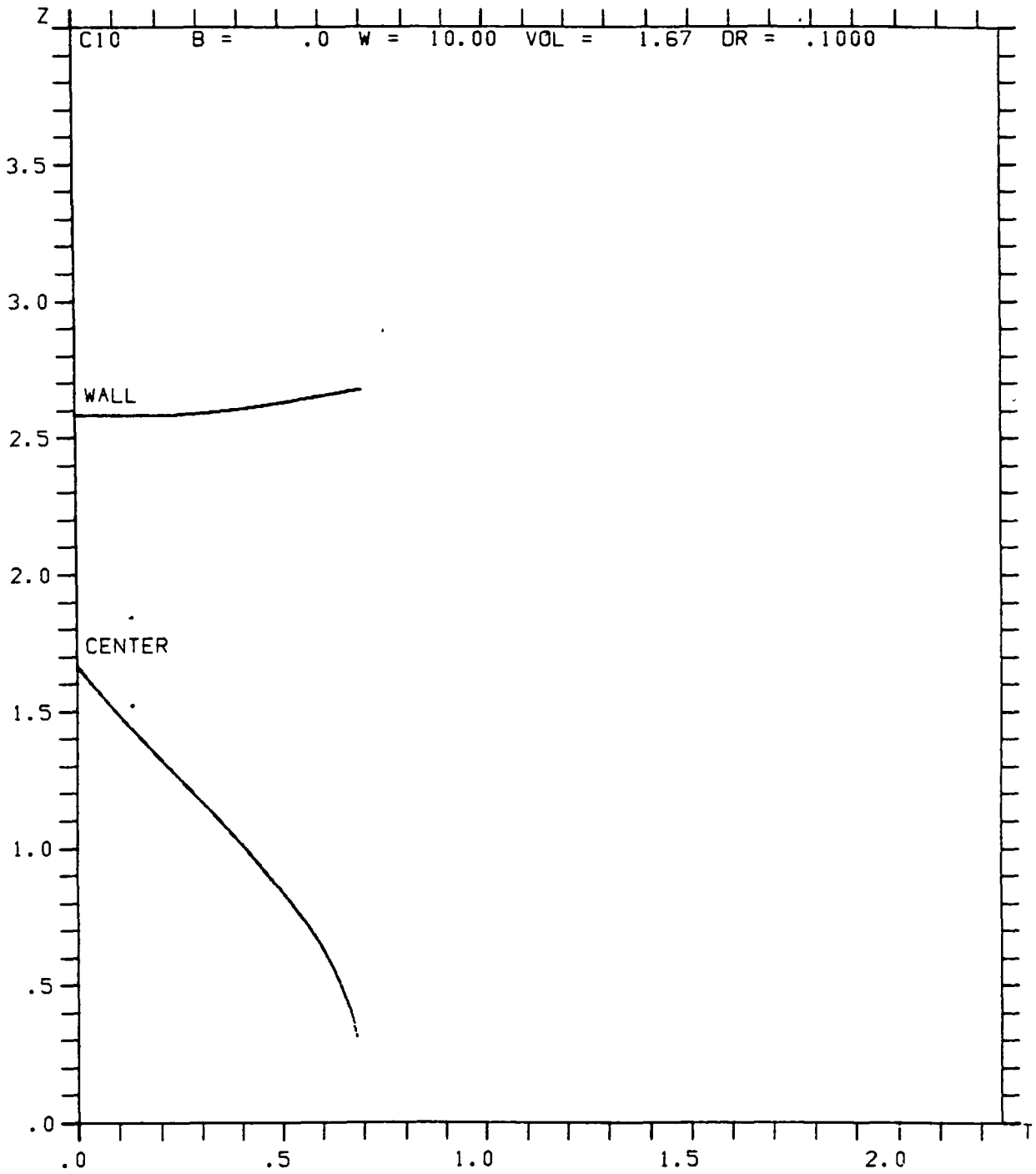

(b) Histories of free surface points at centerline and wall.

Figure 8 (cont). Draining characteristics for Case 10; $(B, W, r_o, V_o)=(0, 10, 1/10, 5\pi/3)$.

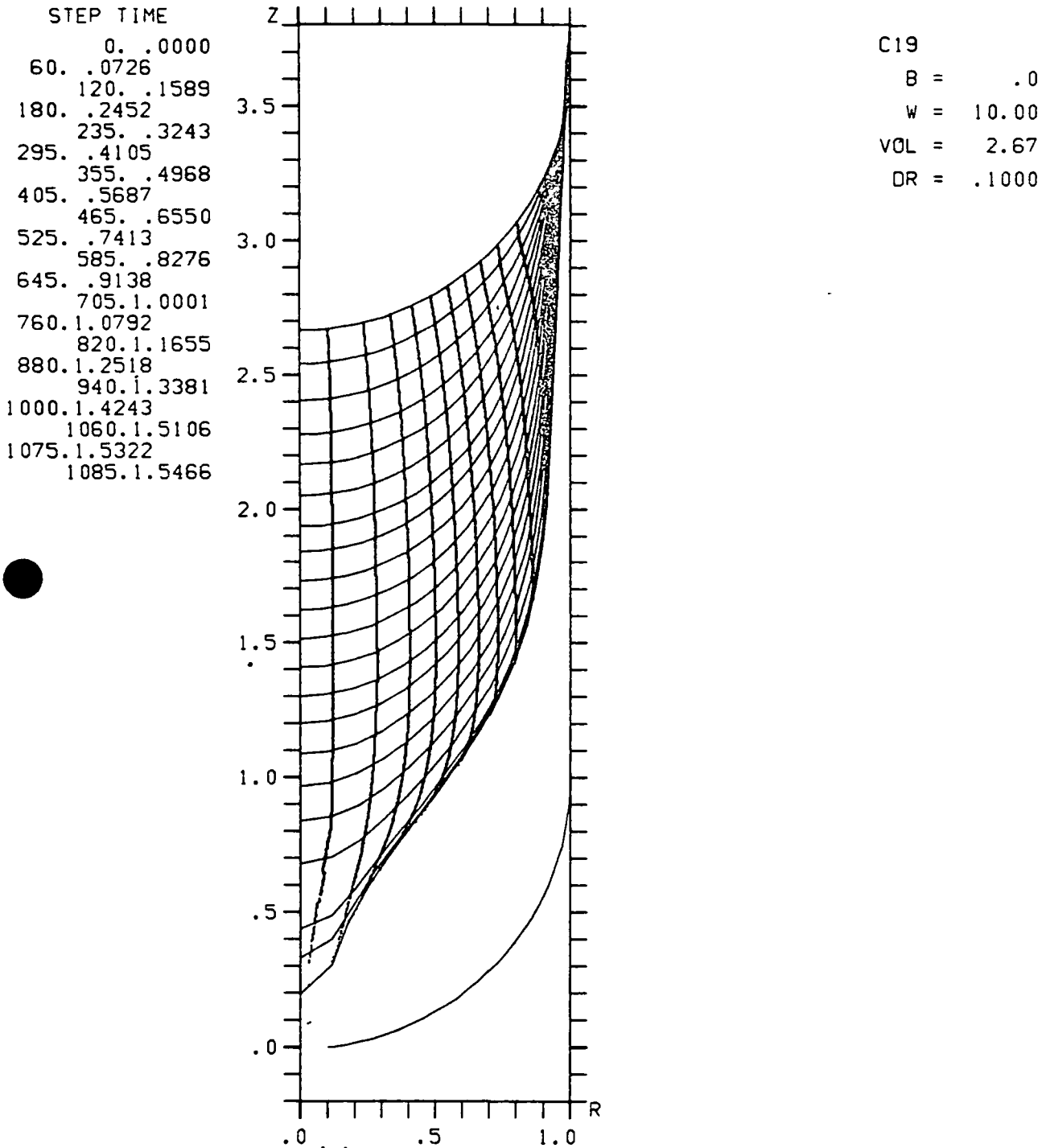

(a) Free surfaces and trajectories of free surface and streamline intersections.

Figure 9. Draining characteristics for Case 19; $(B, W, r_o, V_o) = (0, 10, 1/10, 8\pi/3)$.

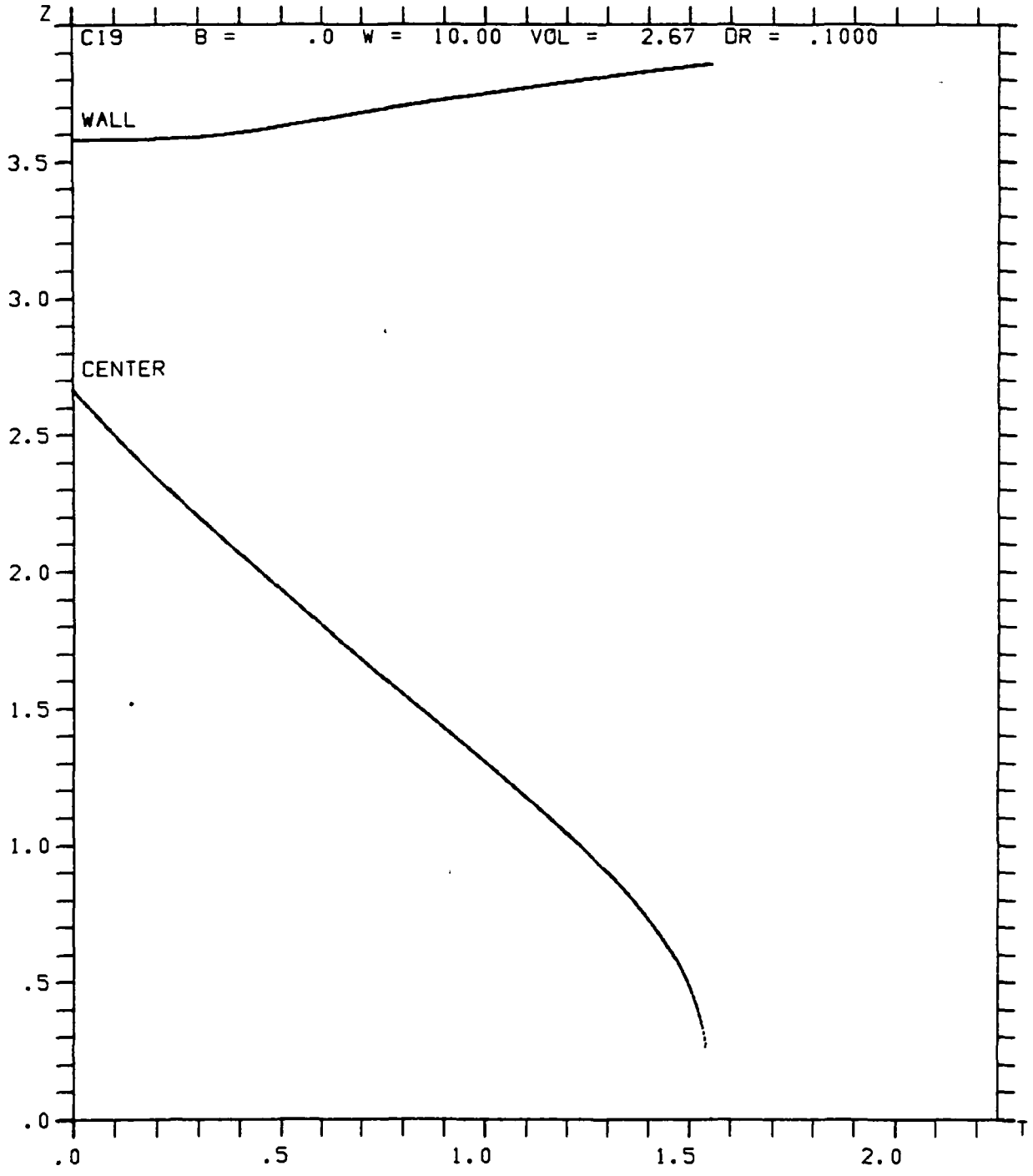

(b) Histories of free surface points at centerline and wall.

Figure 9 (cont). Draining characteristics for Case 19; $(B, W, r_o, V_o)=(0, 10, 1/10, 8\pi/3)$.

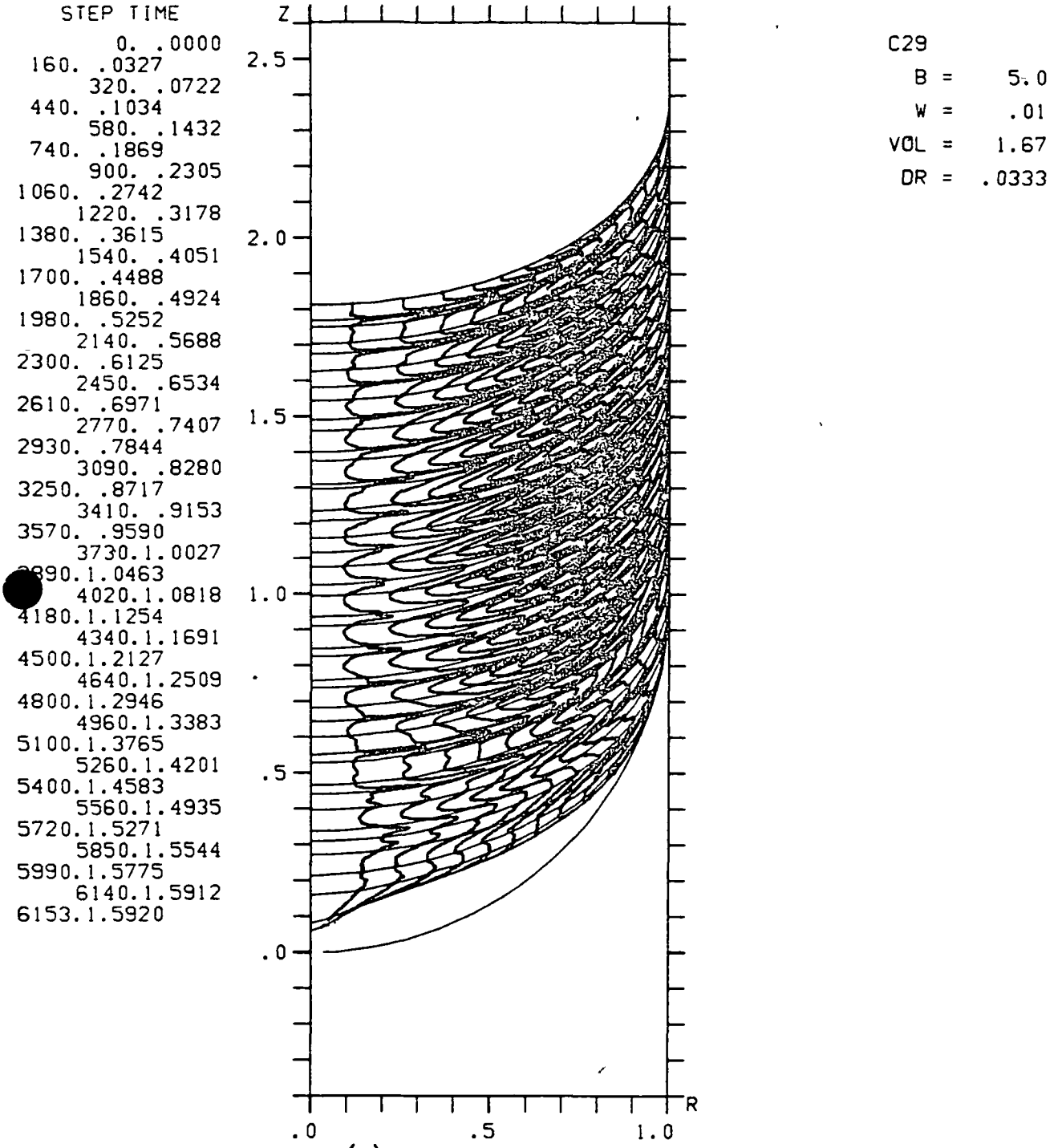

(a) Free surfaces and trajectories of free surface and streamline intersections.

Figure 10. Draining characteristics for Case 29; $(B, W, r_o, V_o)=(5, .01, 1/30, 5\pi/3)$.

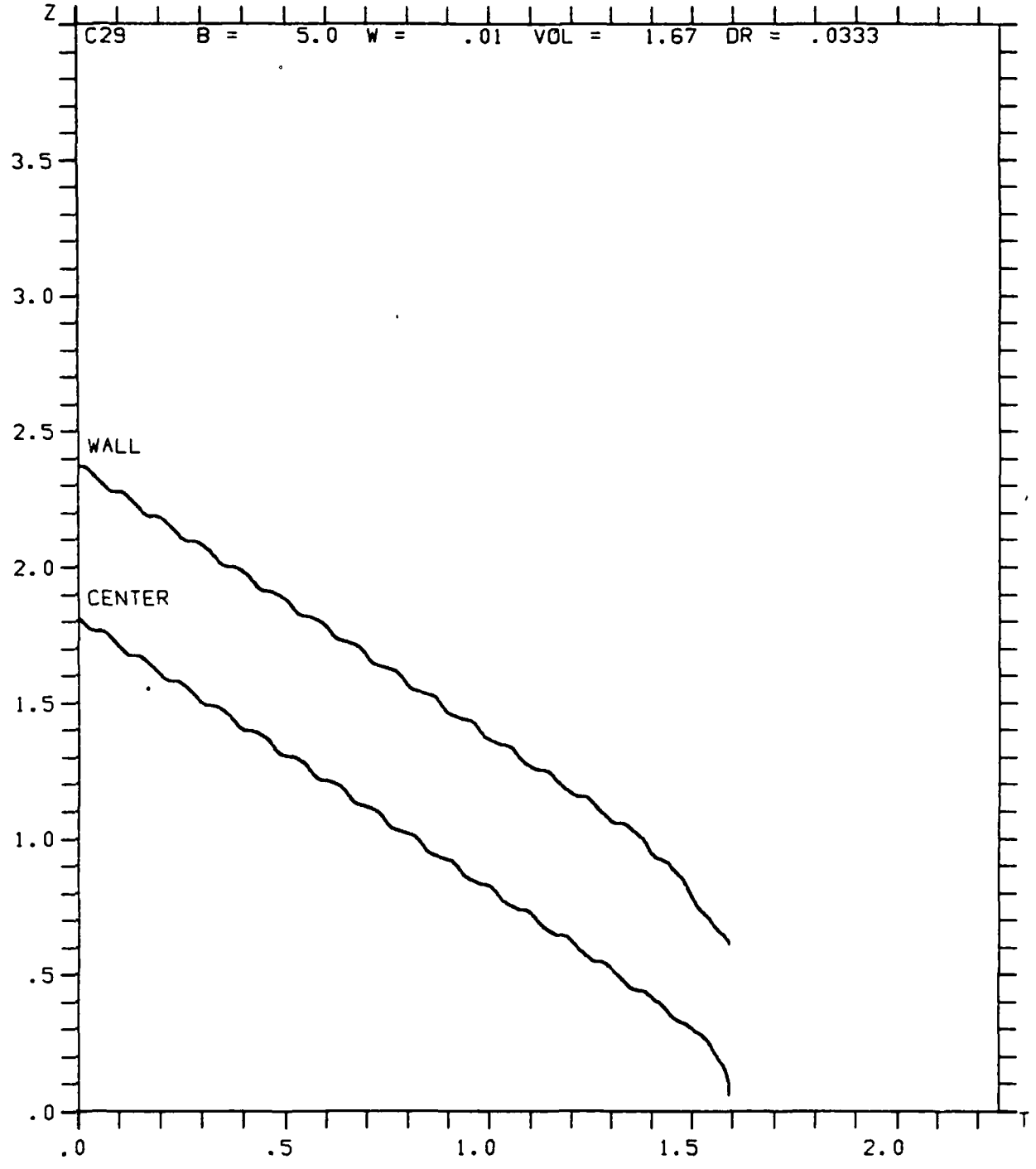

(b) Histories of free surface points at centerline and wall.

Figure 10 (cont). Draining characteristics for Case 29; $(B, W, r_o, V_o) = (5, .01, 1/30, 5\pi/3)$.

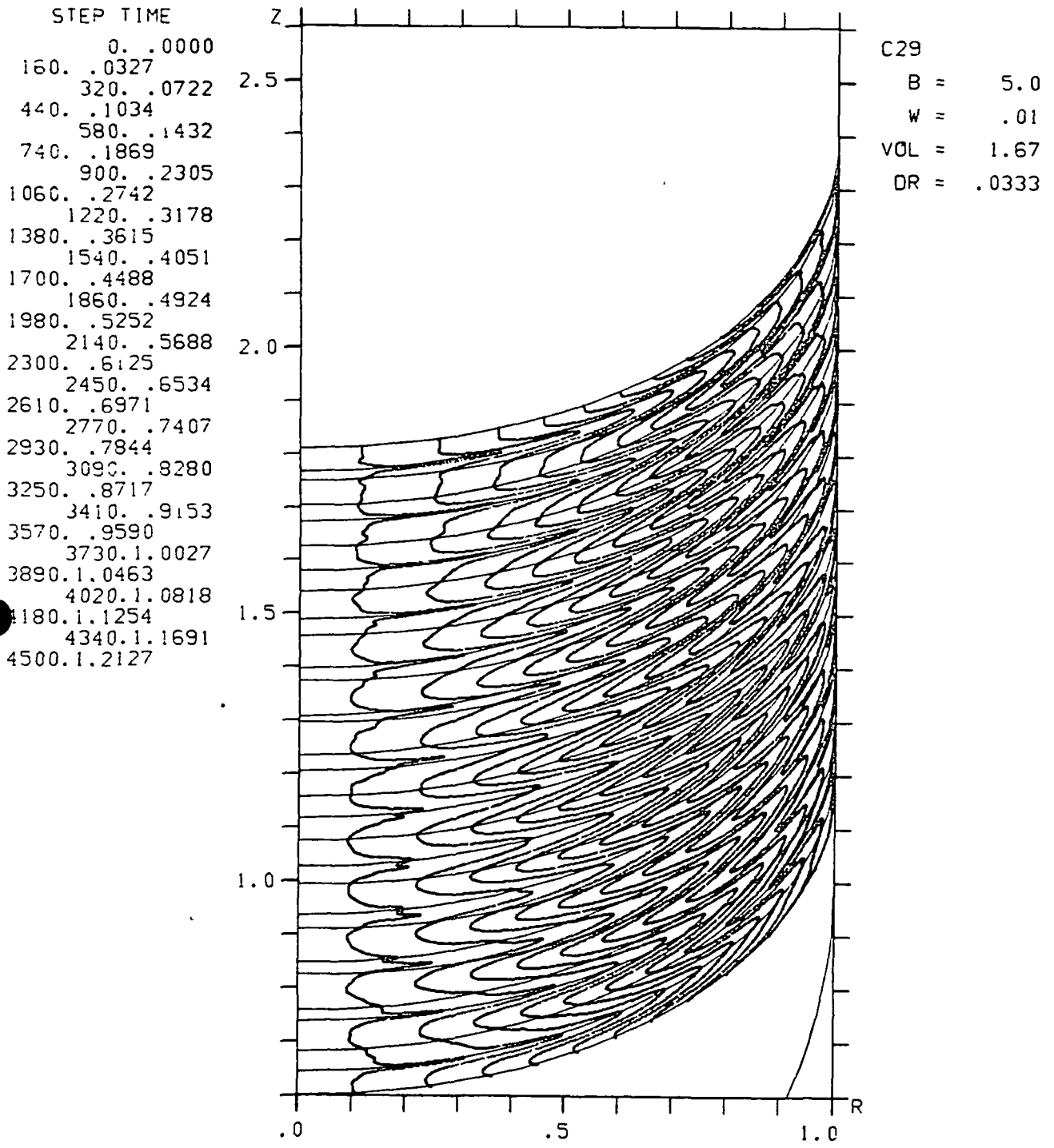

(c) Expanded scale.

Figure 10 (cont). Draining characteristics for Case 29; $(B, W, r_o, V_o)=(5, .01, 1/30, 5\pi/3)$.

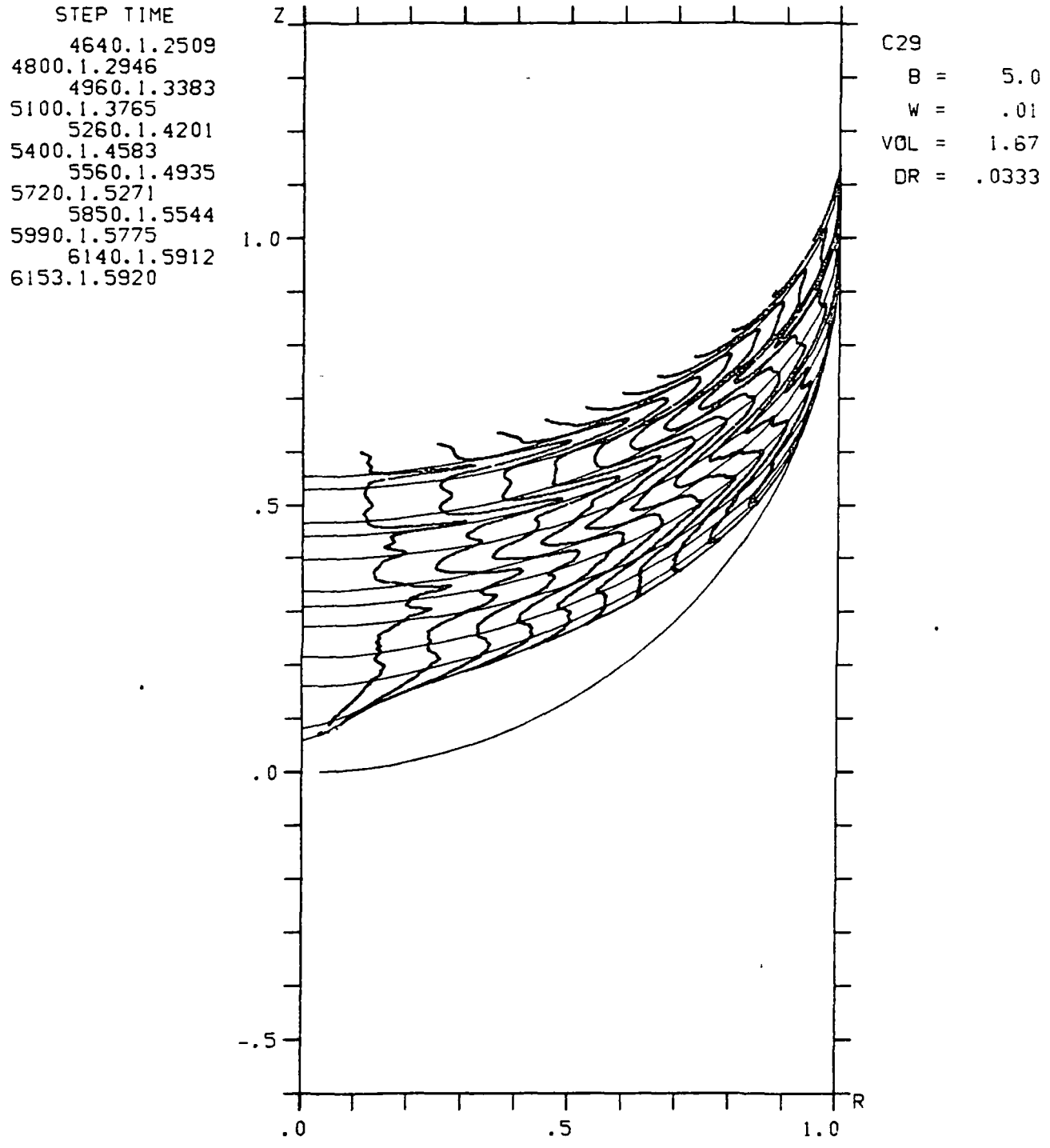

(d) Expanded scale.

Figure 10 (cont). Draining characteristics for Case 29; $(B, W, r_o, V_o) = (5, .01, 1/30, 5\pi/3)$.

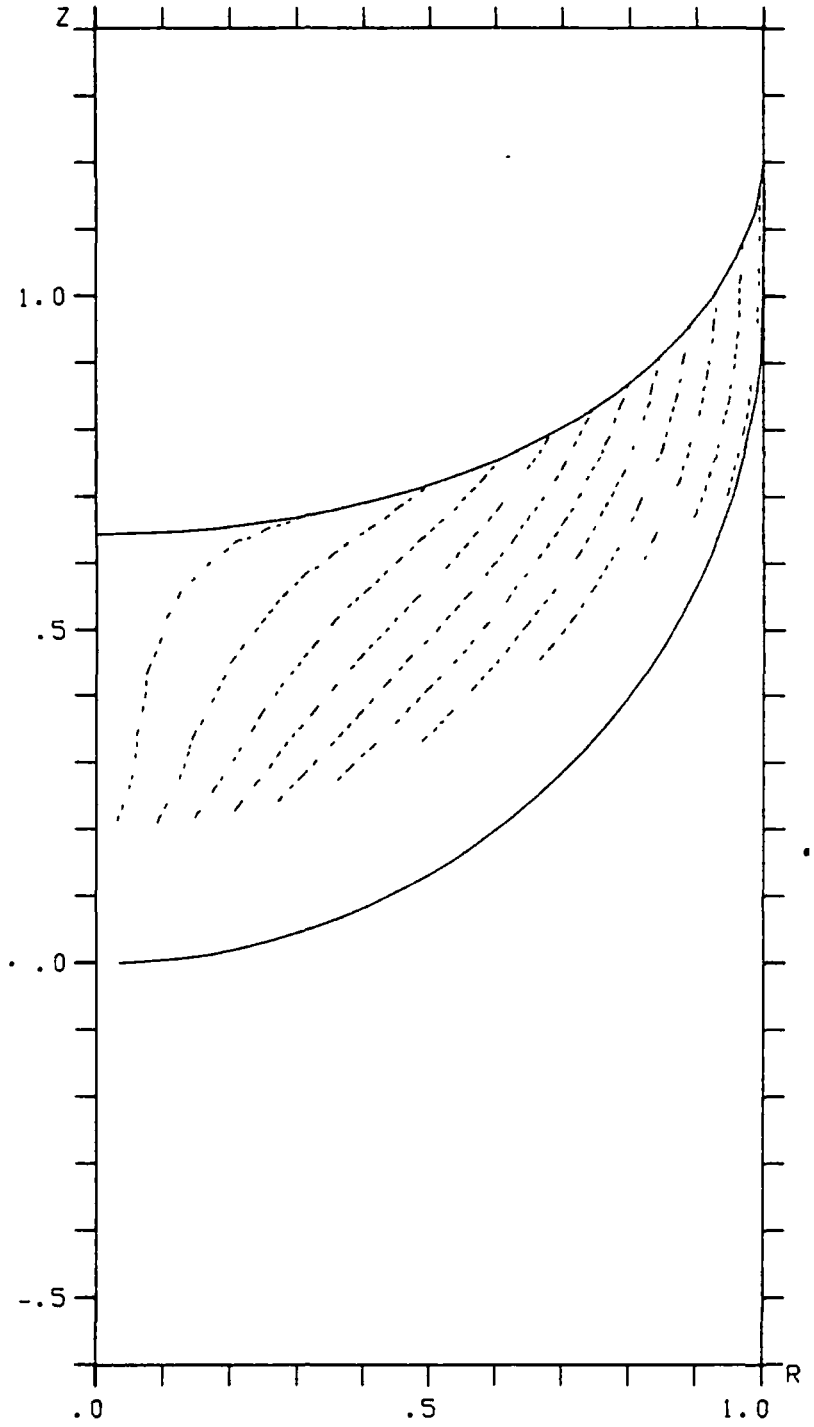

(e) Streamlines at t=1.1718 near maximum of wave with amplitude enhanced by approach to hemispherical bottom.

Figure 10 (cont). Draining characteristics for Case 29; $(B, W, r_o, V_o)=(5, .01, 1/30, 5\pi/3)$.

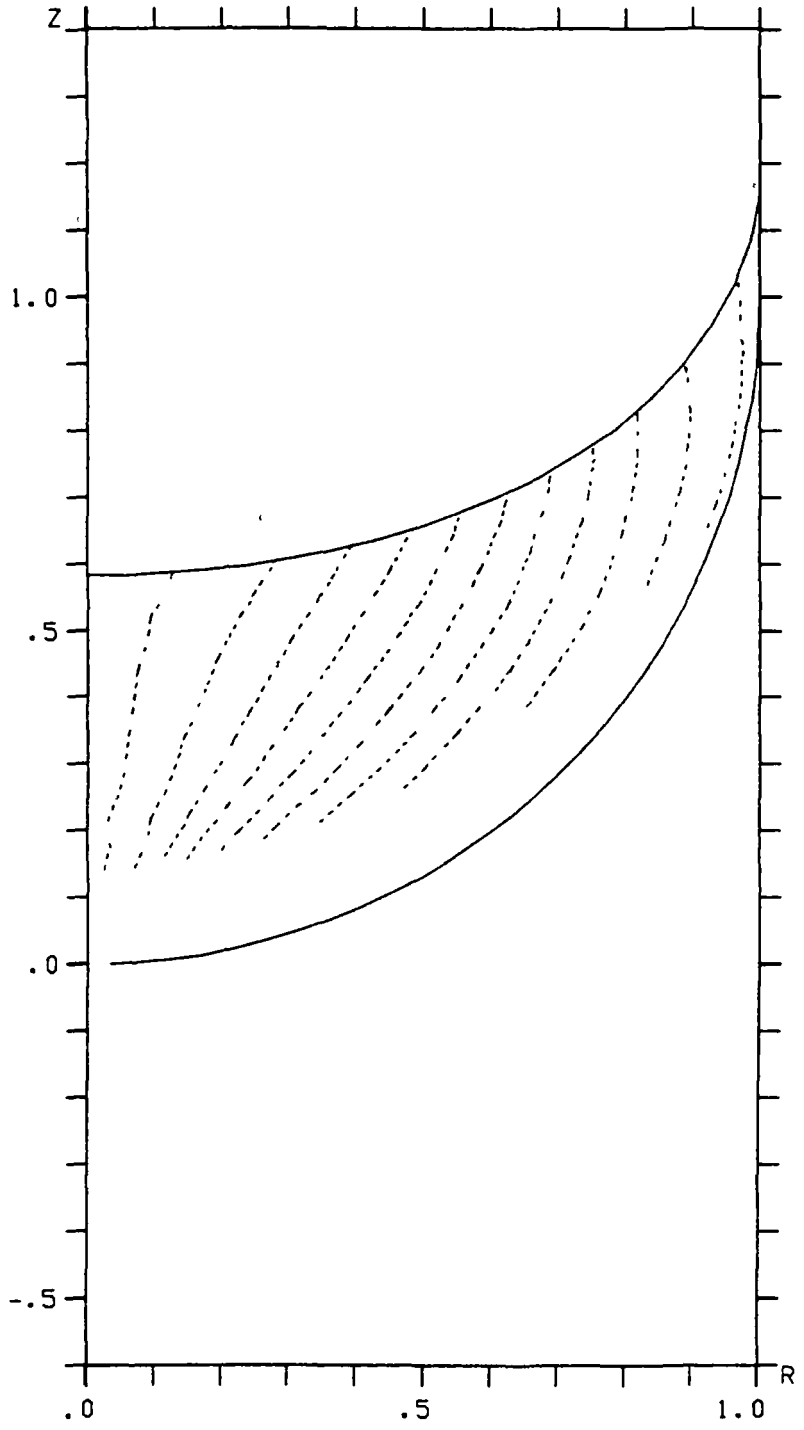

(f) Streamlines at t=1.2264 near beginning of wave with amplitude enhanced by approach to hemispherical bottom.

Figure 10 (cont). Draining characteristics for Case 29; $(B, W, r_o, V_o)=(5, .01, 1/30, 5\pi/3)$.

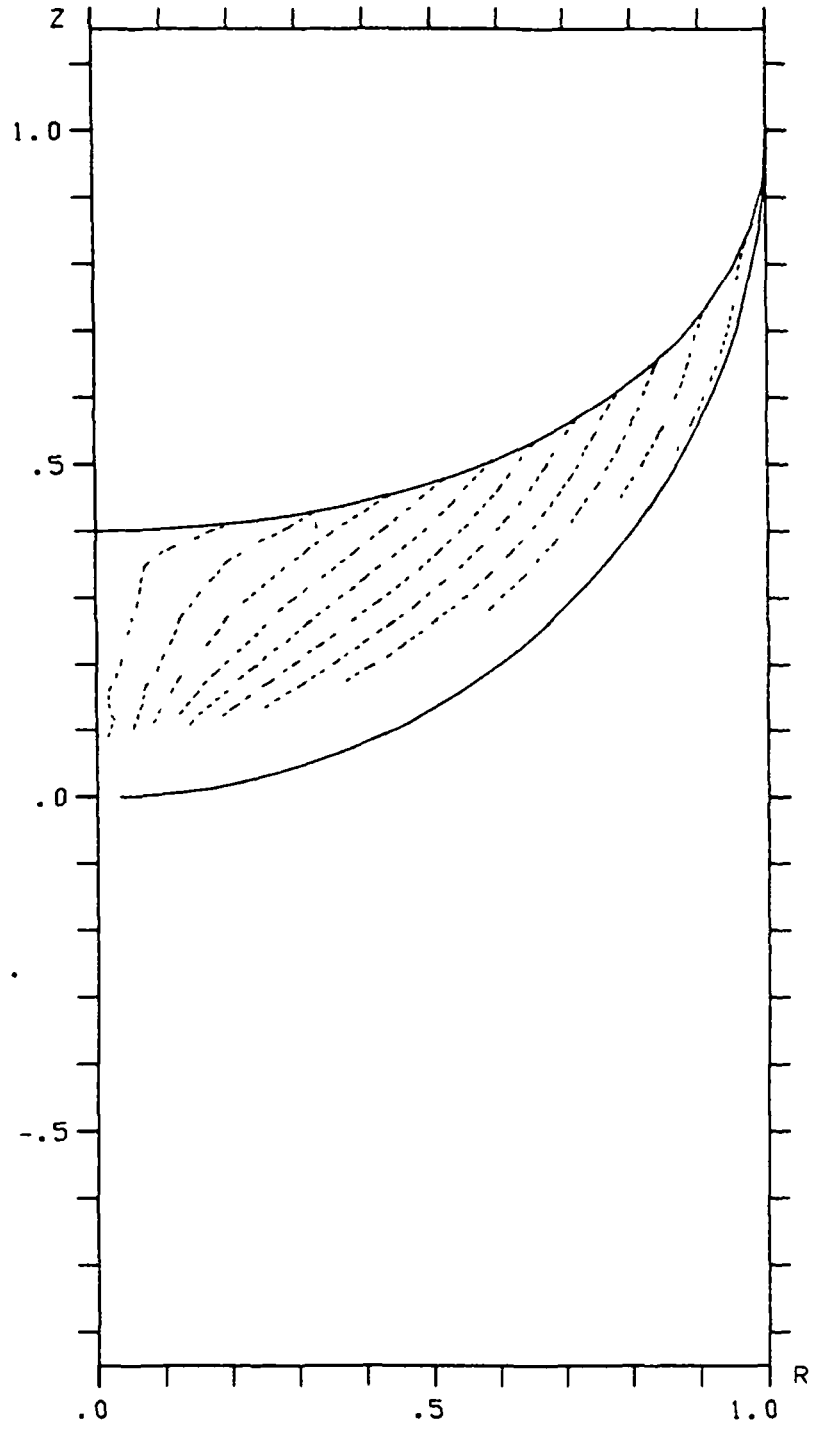

(g) Streamlines at t=1.4174 showing beginning of wave with diminished amplitude in hemisphere.

Figure 10 (cont). Draining characteristics for Case 29; $(B, W, r_o, V_o)=(5, .01, 1/30, 5\pi/3)$.

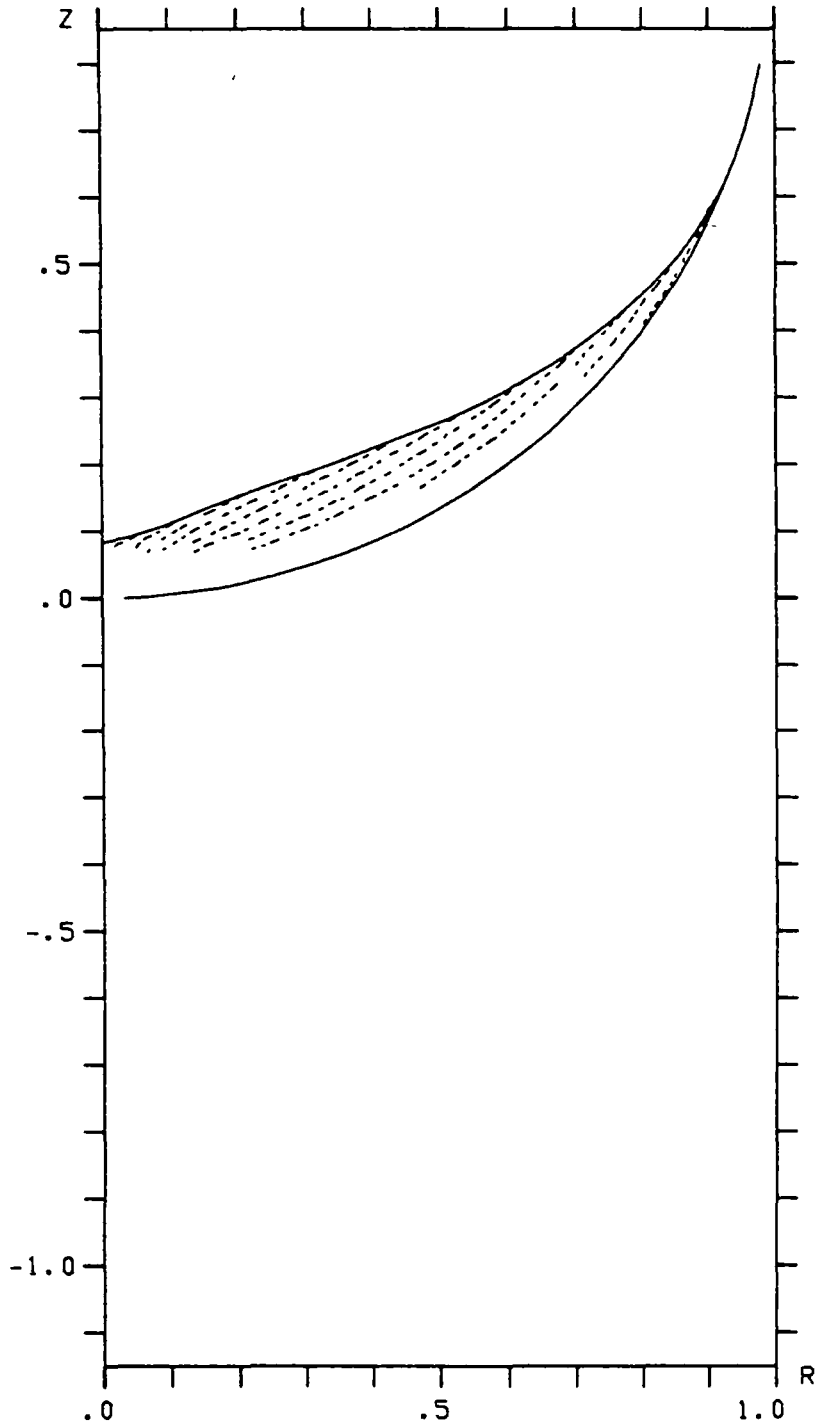

(h) Terminal streamline pattern at t=1.5912.

Figure 10 (cont). Draining characteristics for Case 29; $(B, W, r_o, V_o)=(5, .01, 1/30, 5\pi/3)$.

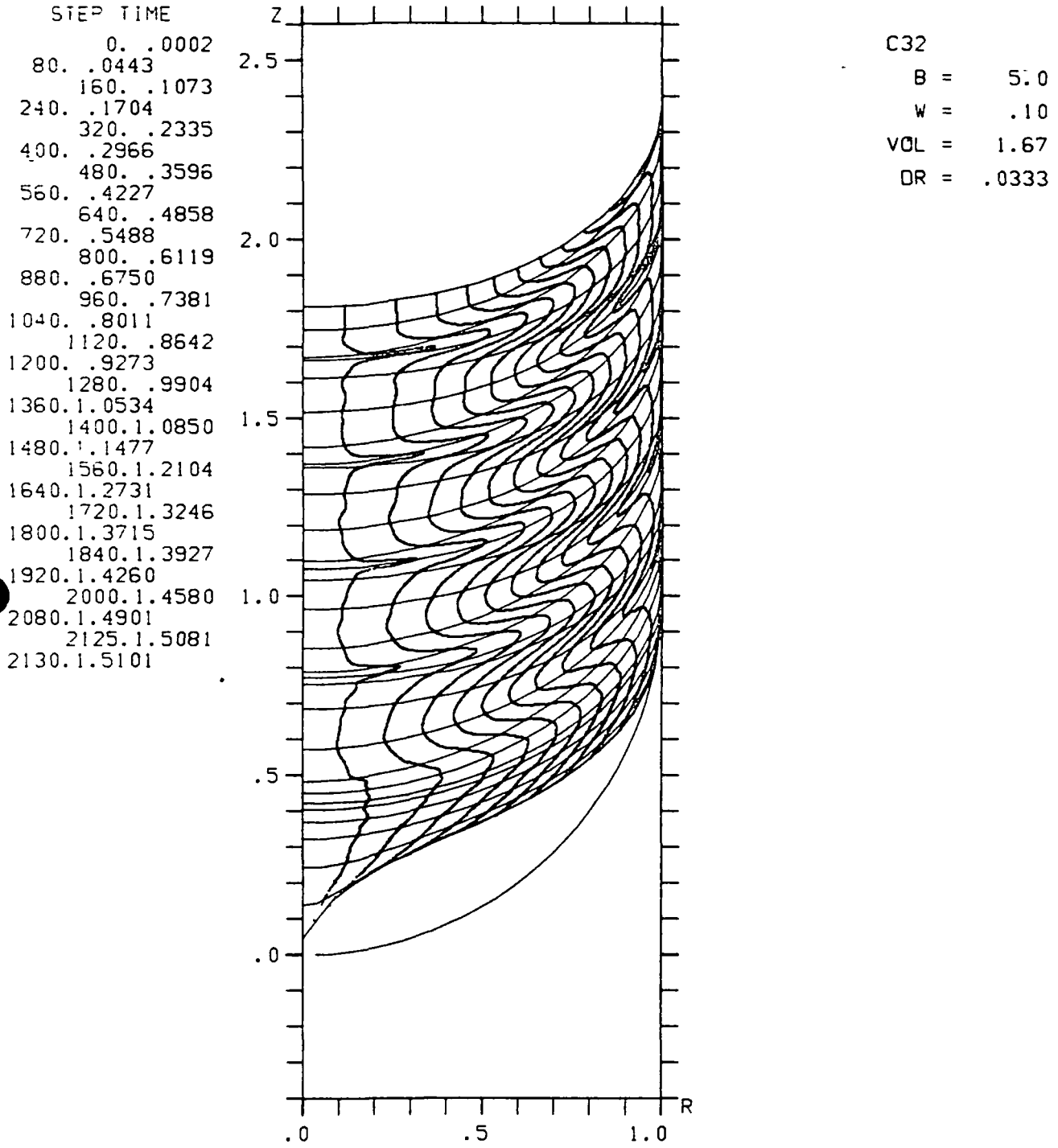

(a) Free surfaces and trajectories of free surfaces and streamline intersections.

Figure 11. Draining characteristics for Case 32; $(B, W, r_o, V_o) = (5, .1, 1/30, 5\pi/3)$.

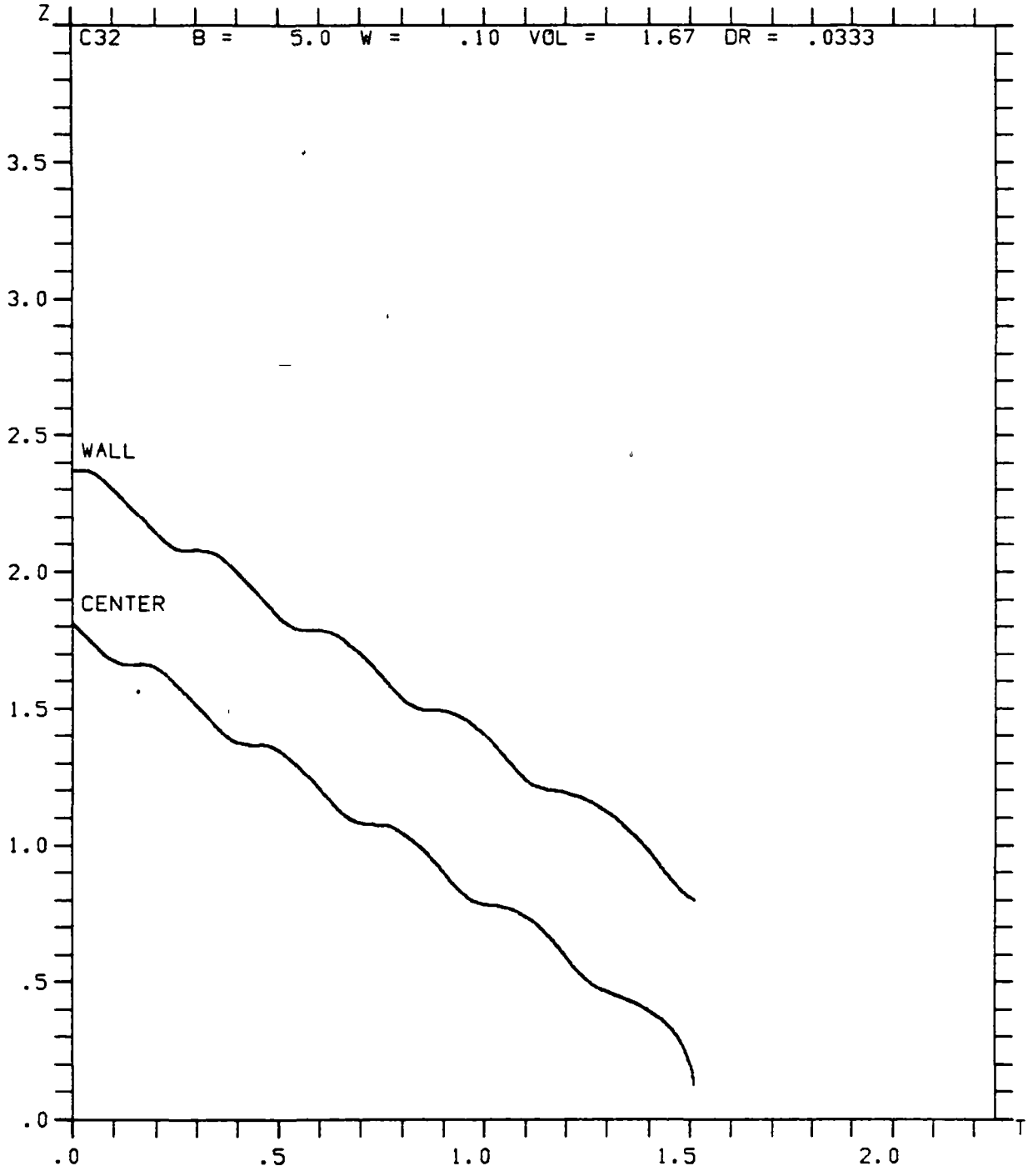

(b) Histories of free surface points at centerline and wall.

Figure 11 (cont). Draining characteristics for Case 32; $(B, W, r_o, V_o)=(5, .1, 1/30, 5\pi/3)$.

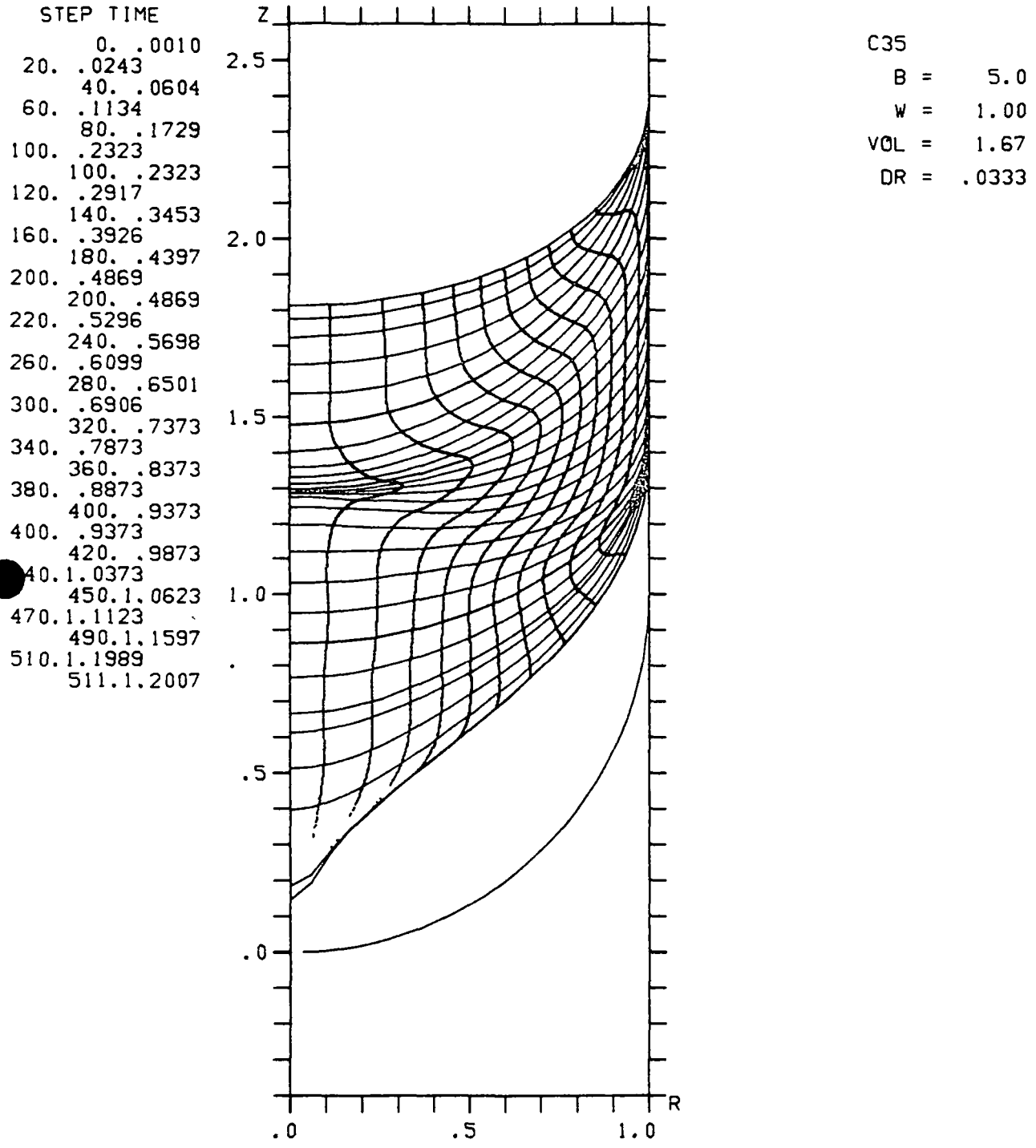

(a) Free surfaces and trajectories of free surfaces and streamline intersections.

Figure 12. Draining characteristics for Case 35; $(B, W, r_o, V_o)=(5, 1, 1/30, 5\pi/3)$.

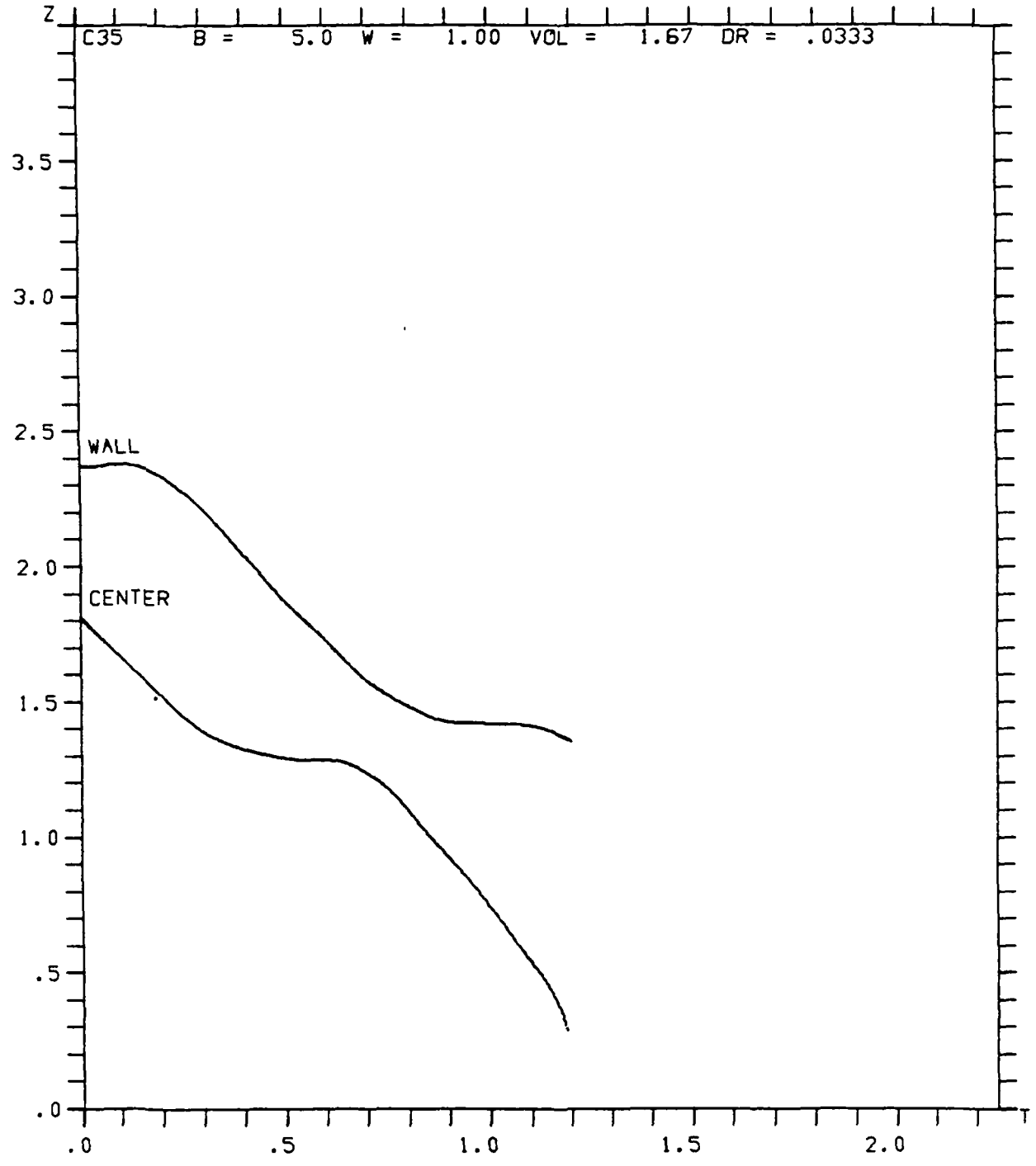

(b) Histories of free surface points at centerline and wall.

Figure 12 (cont). Draining characteristics for Case 35; $(B, W, r_o, V_o) = (5, 1, 1/30, 5\pi/3)$.

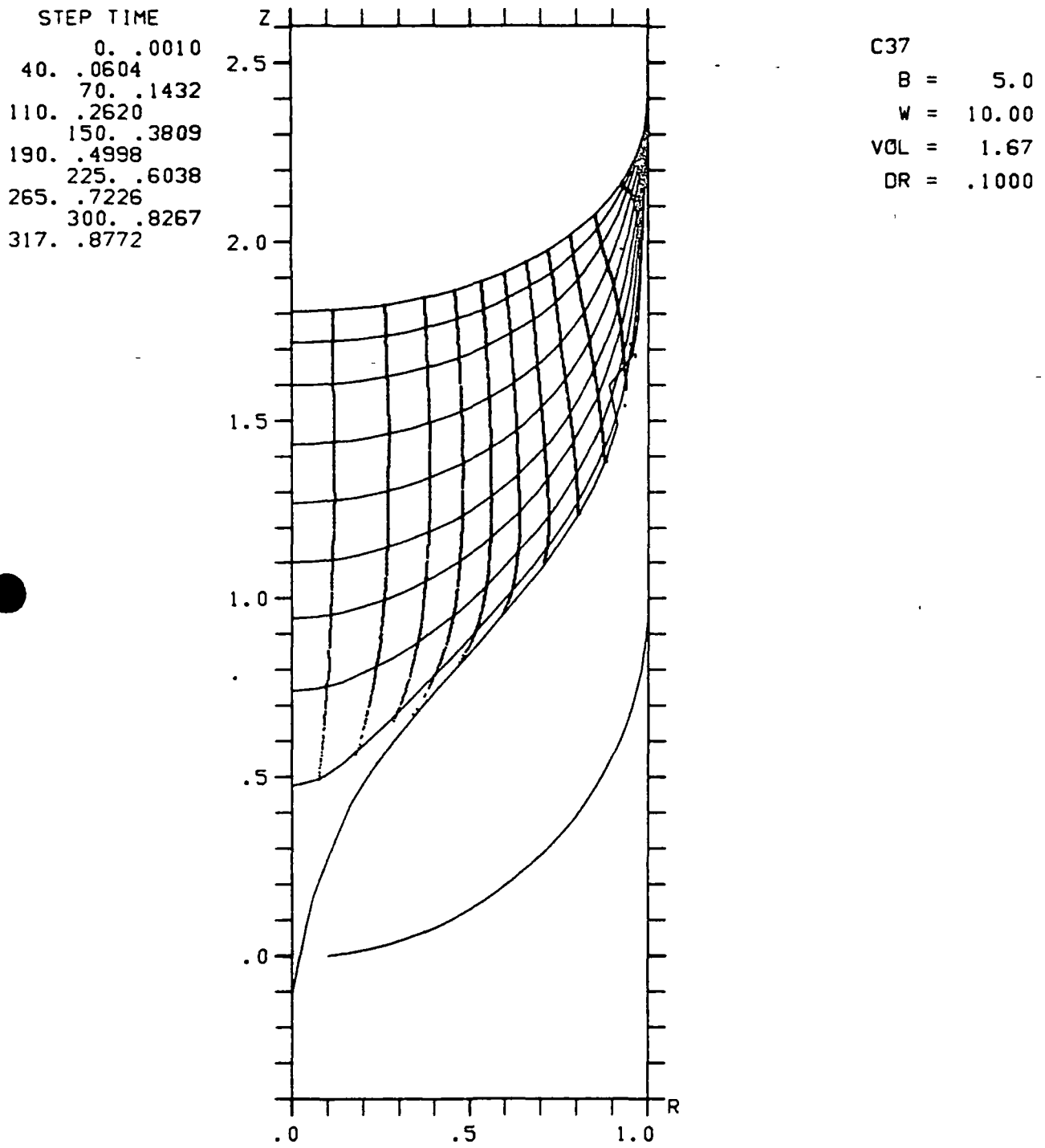

(a) Free surfaces and trajectories of free surface and streamline intersections.

Figure 13. Draining characteristics for Case 37; $(B, W, r_o, V_o) = (5, 10, 1/10, 5\pi/3)$.

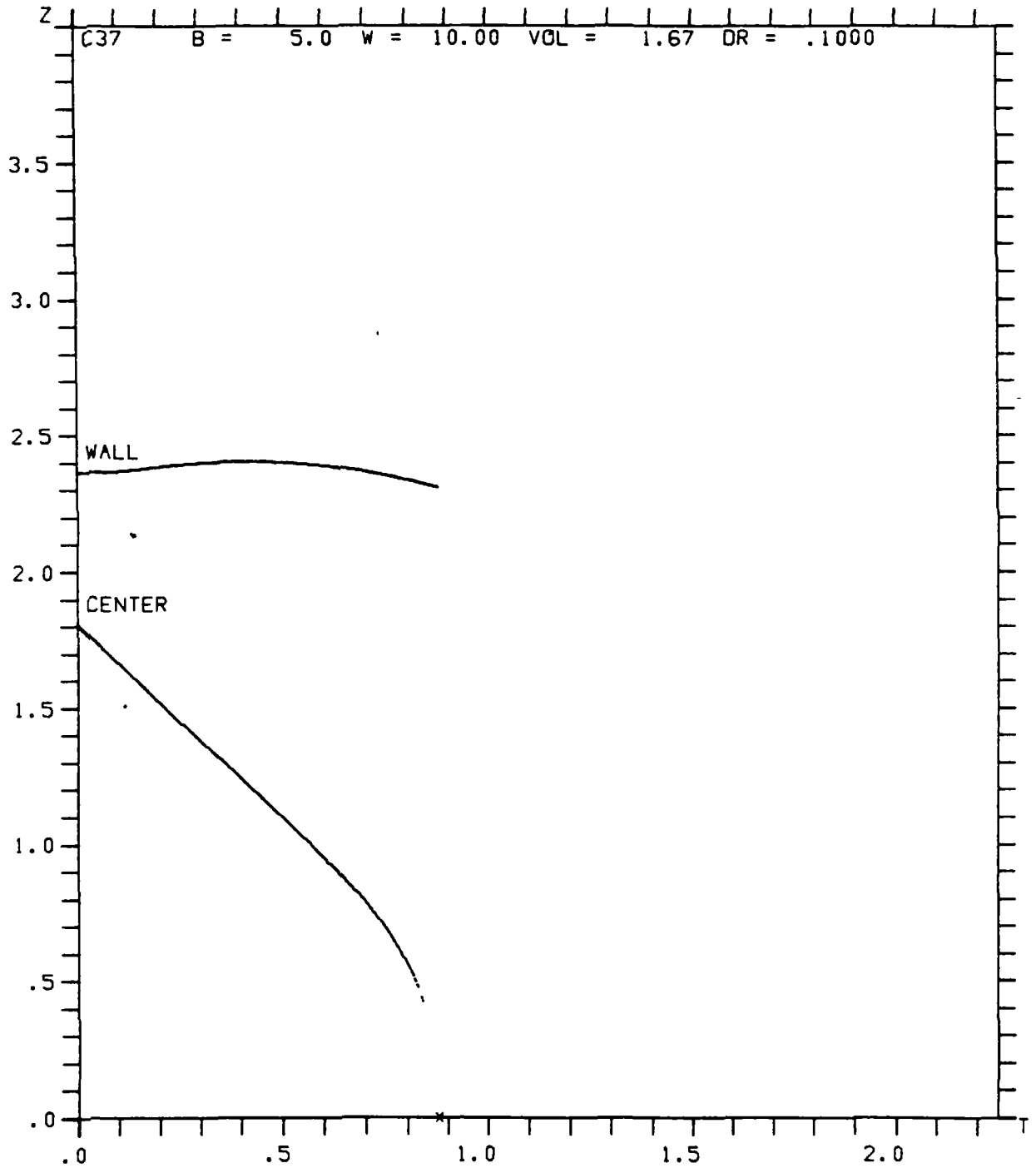

(b) Histories of free surface points at centerline and wall.

Figure 13 (cont). Draining characteristics for Case 37; $(B, W, r_o, V_o) = (5, 10, 1/10, 5\pi/3)$.

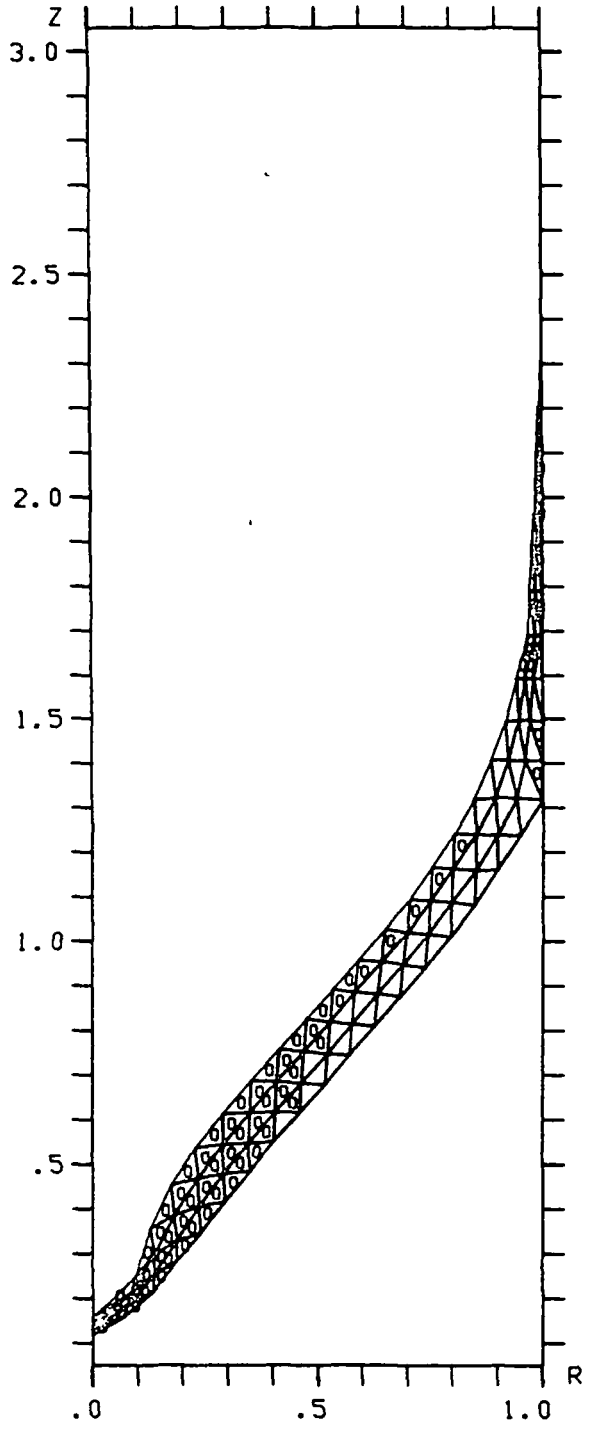

(c) Mesh and free surface at t=.8712 showing wave at base of wall sheet.

Figure 13 (cont). Draining characteristics for Case 37; $(B, W, r_o, V_o)=(5, 10, 1/10, 5\pi/3)$.

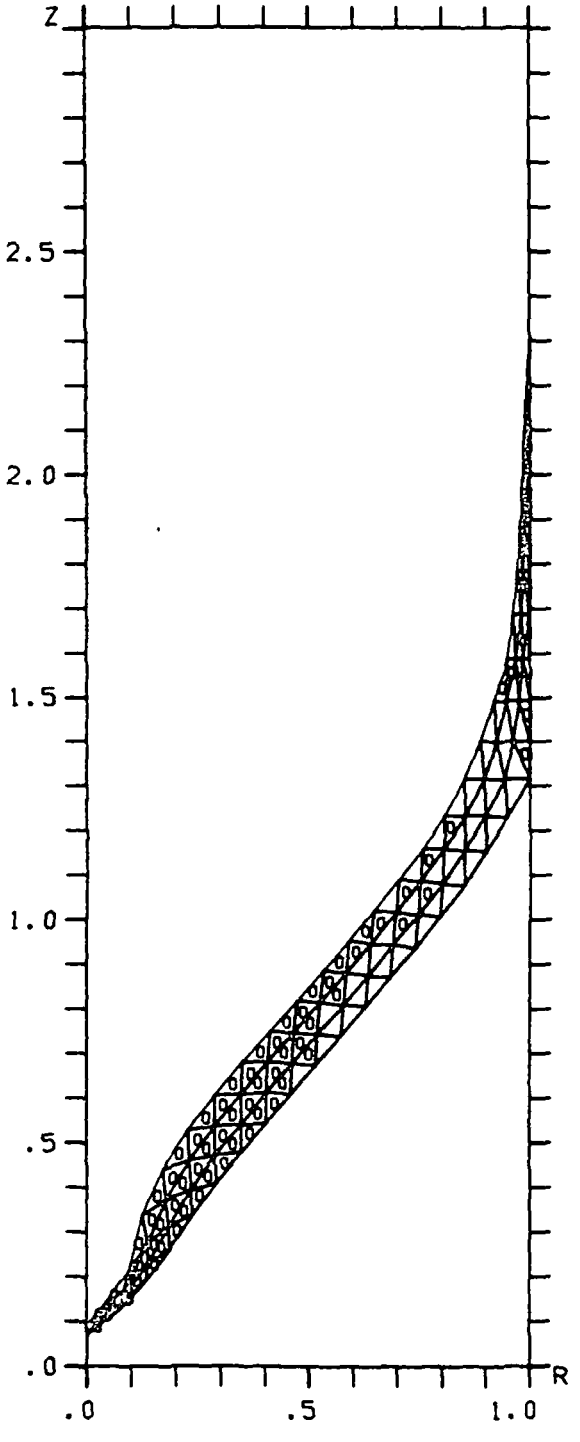

(d) Mesh and free surface at t=.8742 just before vapor ingestion.

Figure 13 (cont). Draining characteristics for Case 37; $(B,W,r_o,V_o)=(5,10,1/10,5\pi/3)$.

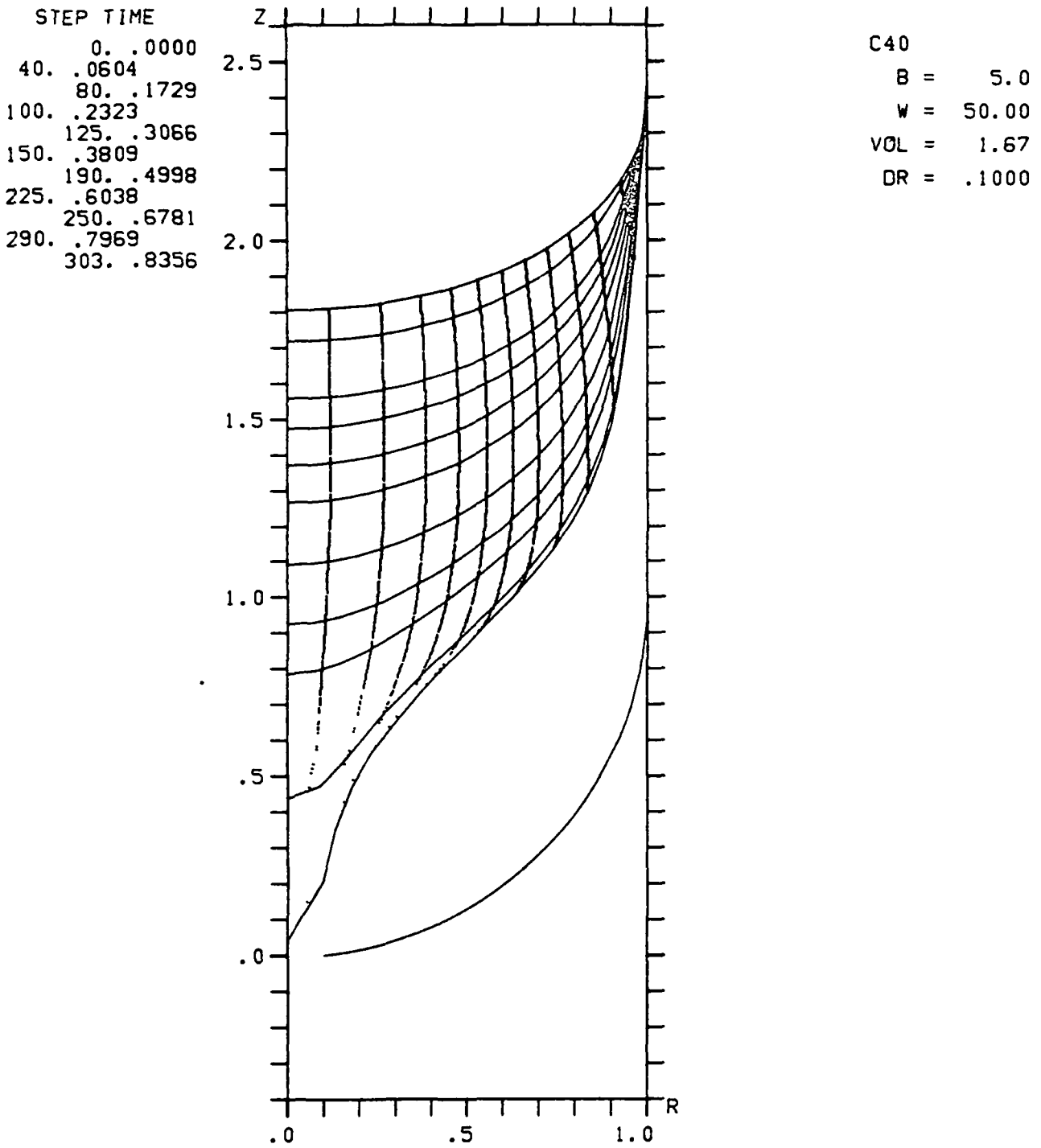

(a) Free surfaces and trajectories of free surfaces and streamline intersections.

Figure 14. Draining characteristics for Case 40; $(B, W, r_o, V_o) = (5, 50, 1/10, 5\pi/3)$.

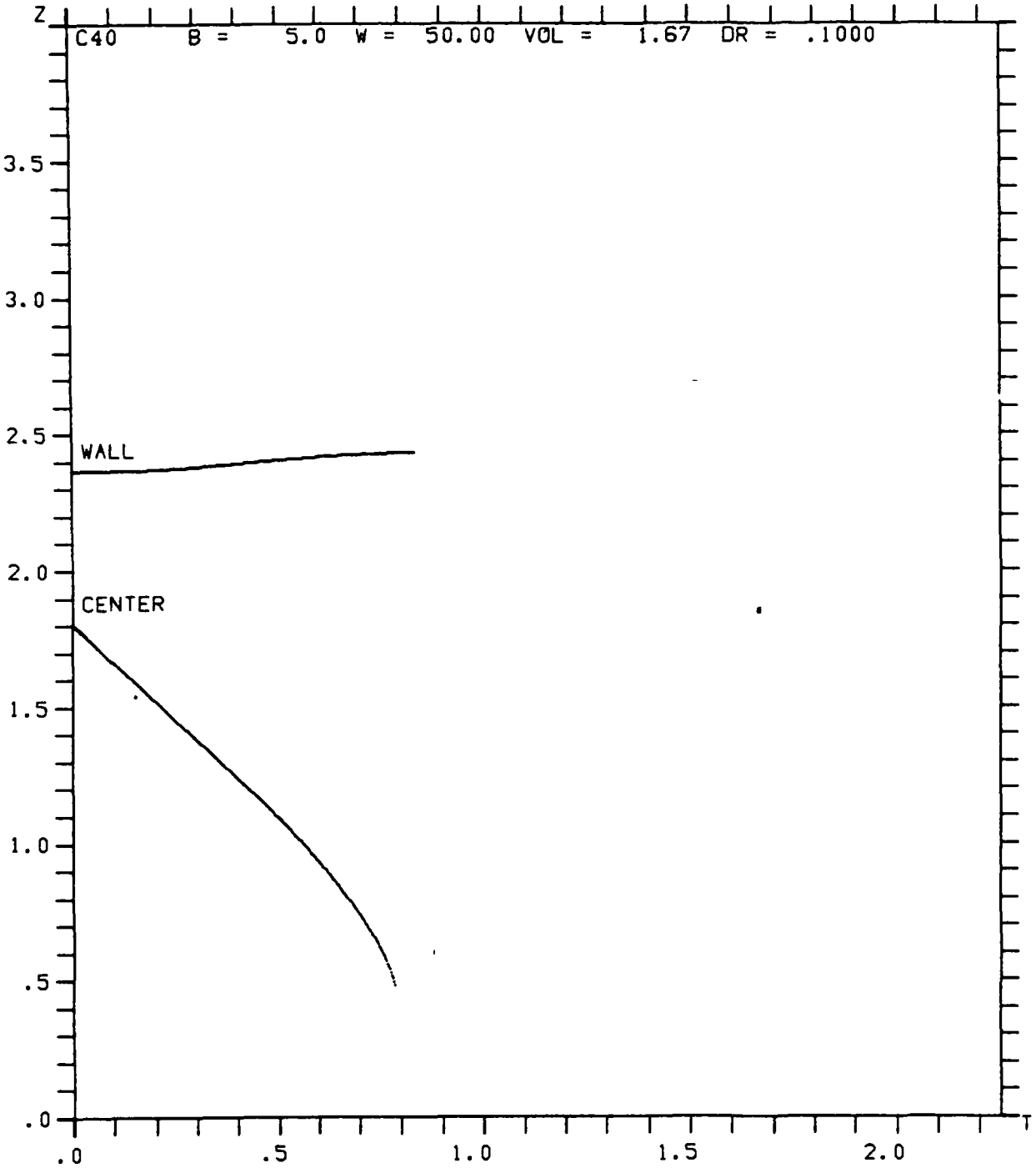

(b) Histories of free surface points at centerline and wall.

Figure 14 (cont). Draining characteristics for Case 40; $(B, W, r_o, V_o)=(5, 50, 1/10, 5\pi/3)$.

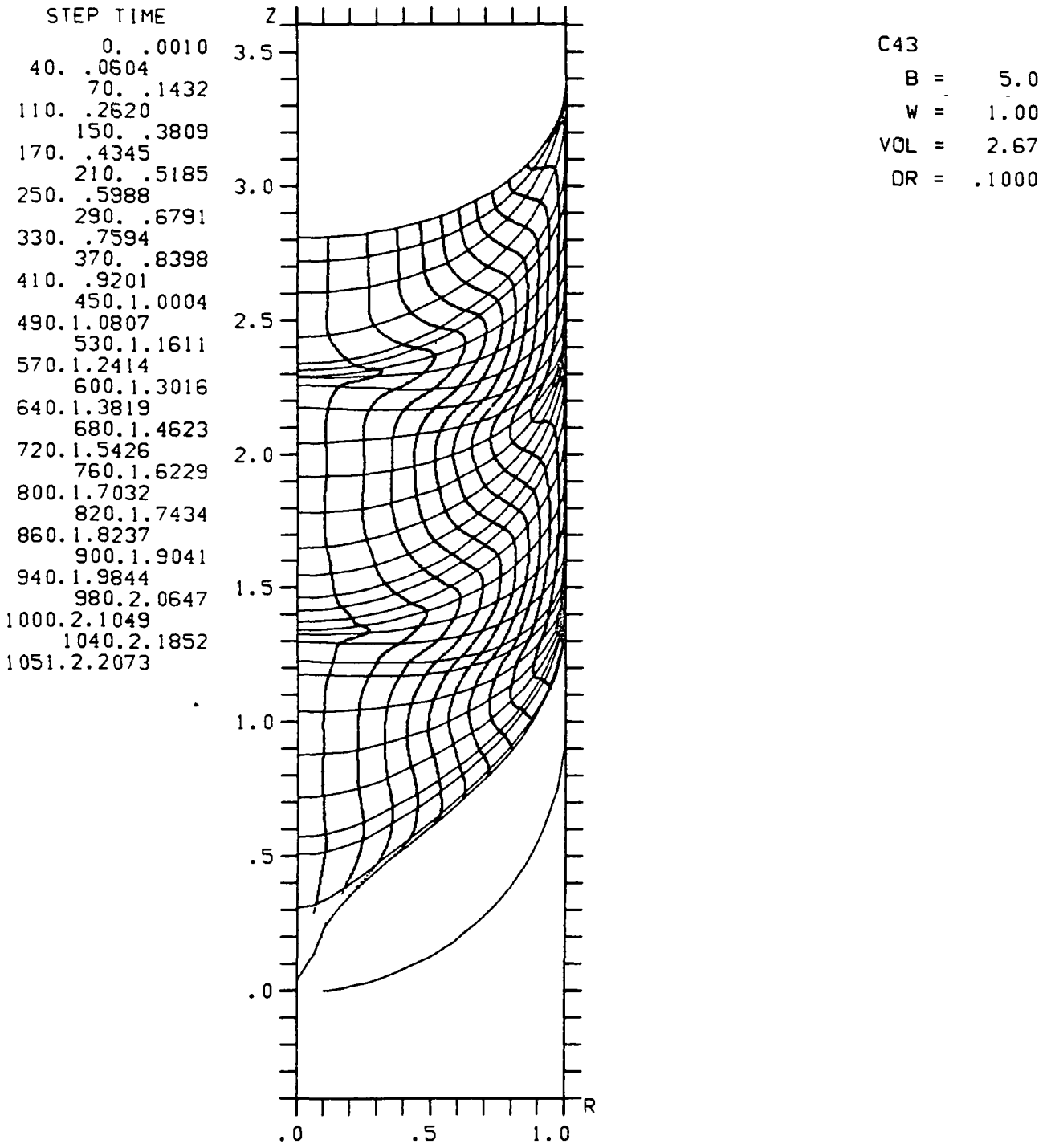

(a) Free surfaces and trajectories of free surface and streamline intersections.

Figure 15. Draining characteristics for Case 43; $(B, W, r_o, V_o)=(5, 1, 1/10, 8\pi/3)$.

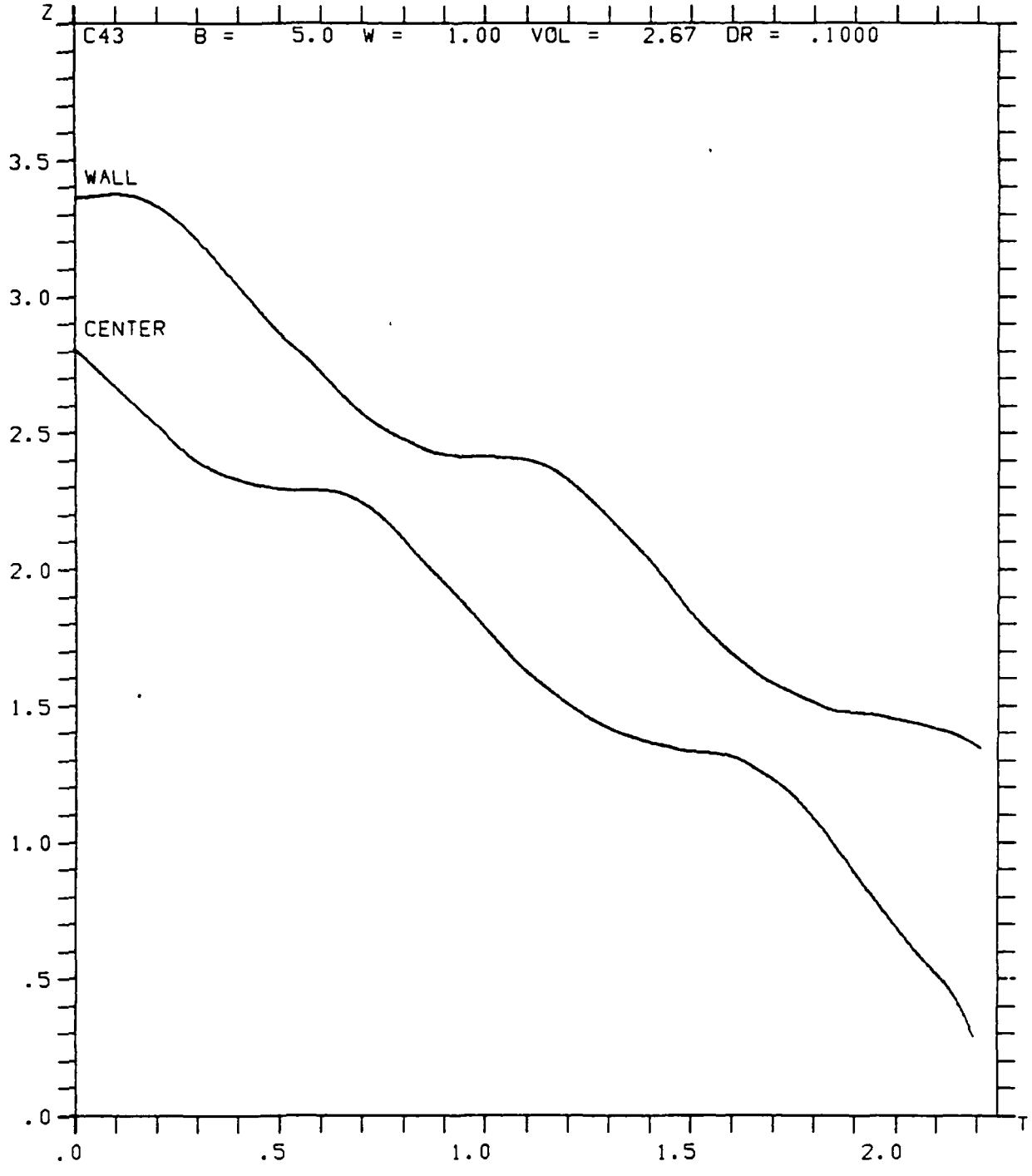

(b) Histories of free surface points at centerline and wall.

Figure 15 (cont). Draining characteristics for Case 43; $(B, W, r_o, V_o)=(5, 1, 1/10, 8\pi/3)$.

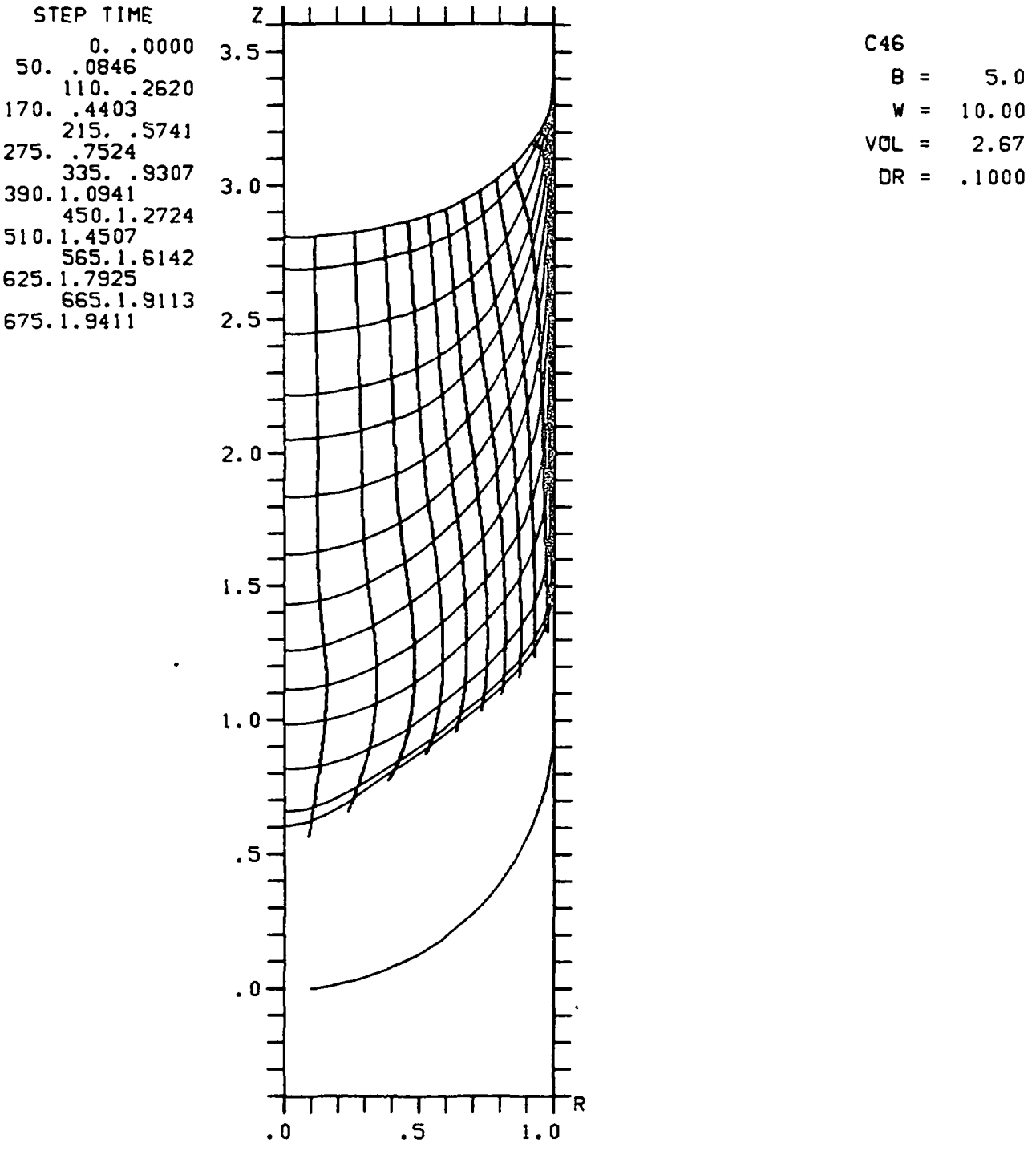

(a) Free surfaces and trajectories of free surface and streamline intersections.

Figure 16. Draining characteristics for Case 46; $(B, W, r_o, V_o)=(5, 10, 1/10, 8\pi/3)$.

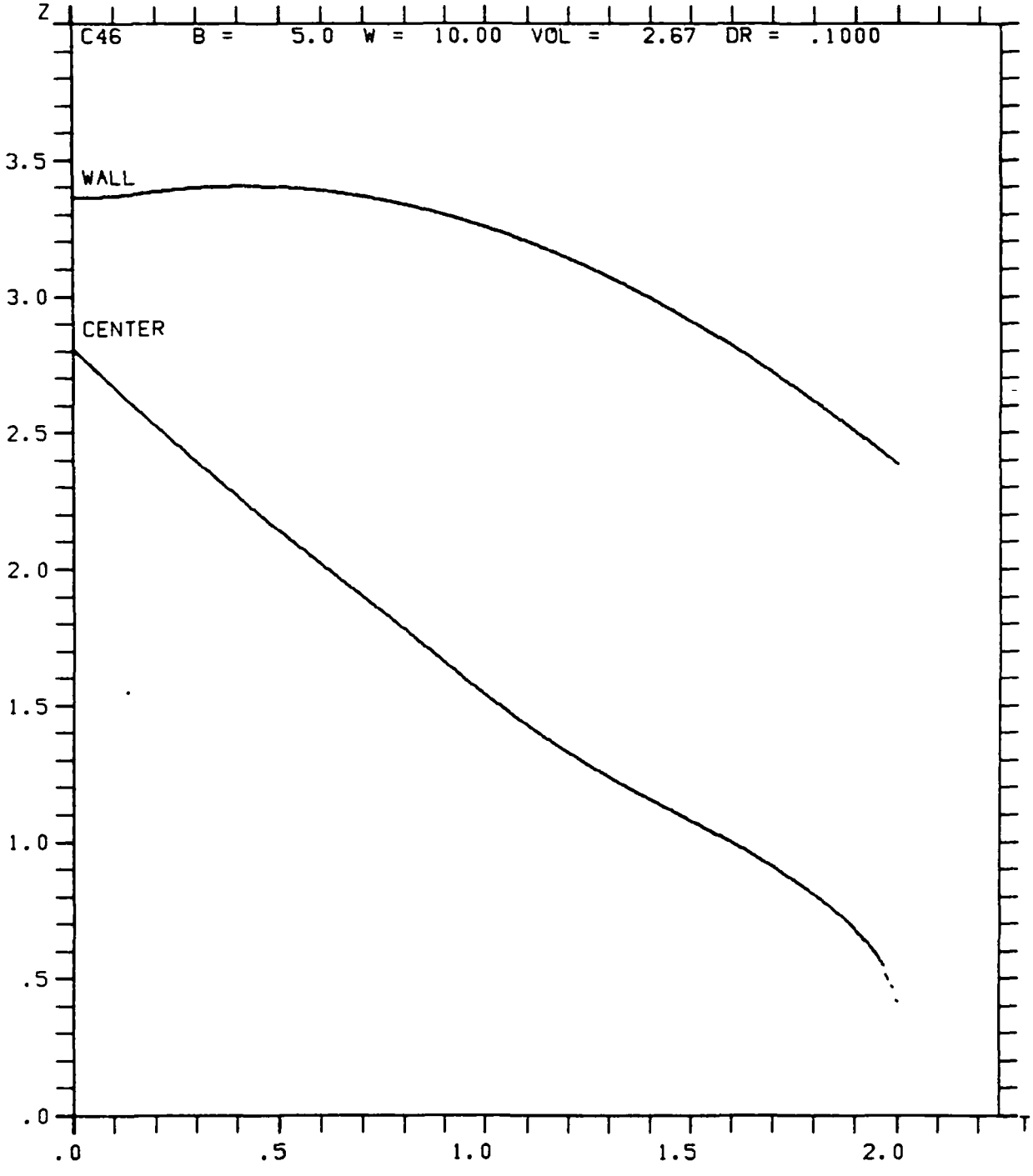

(b) Histories of free surface points at centerline and wall. (Computation in doubt beyond t=1.9678.)

Figure 16 (cont). Draining characteristics for Case 46; $(B, W, r_o, V_o)=(5, 10, 1/10, 8\pi/3)$.

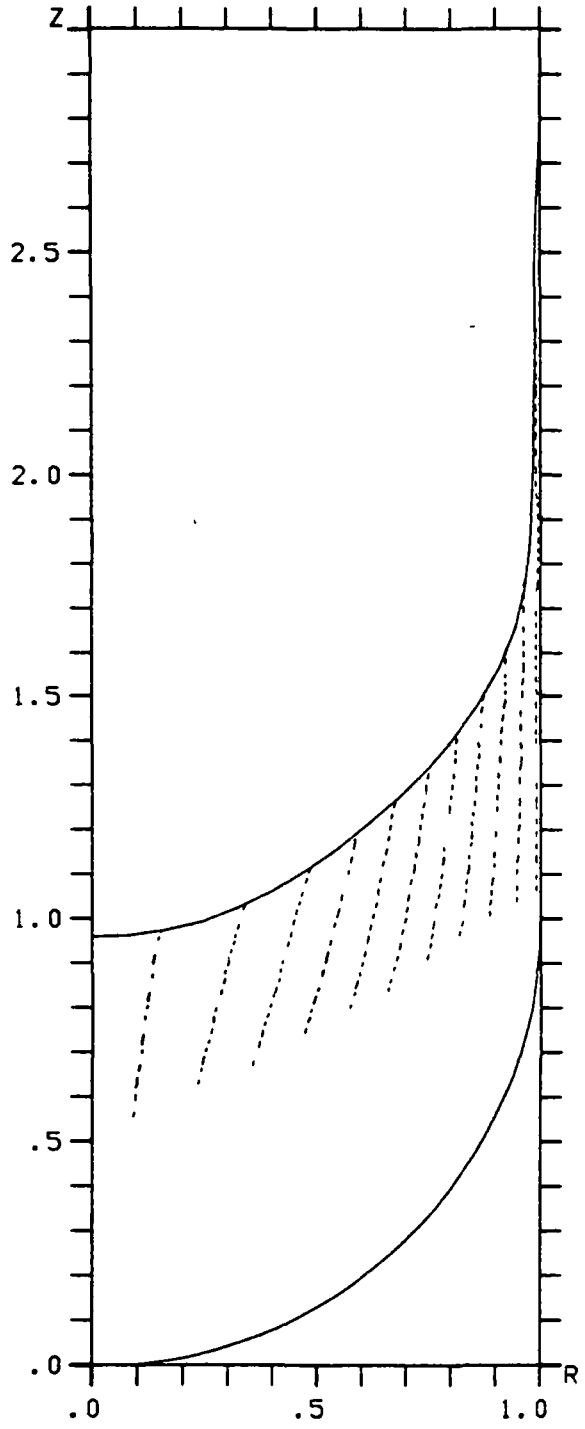

(c) Streamlines at t=1.6439 near maximum of wave.

Figure 16 (cont). Draining characteristics for Case 46; $(B, W, r_o, V_o)=(5, 10, 1/10, 8\pi/3)$.

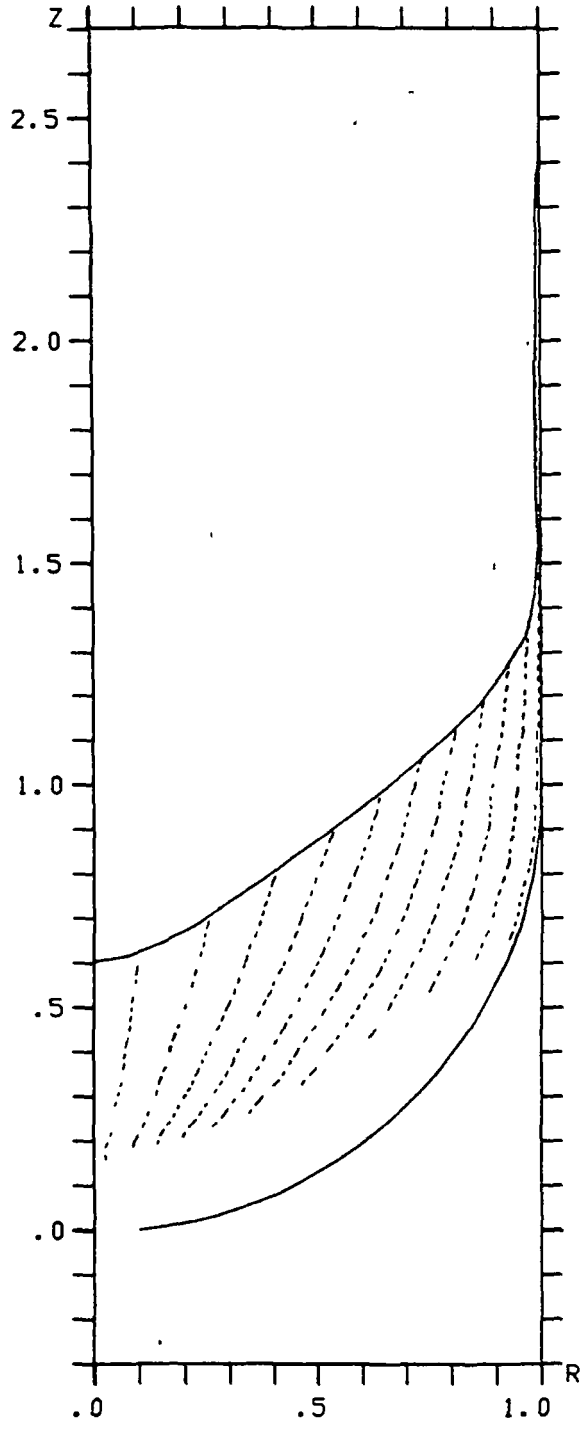

(d) Streamlines at t=1.9411 showing necking at bottom of wall sheet.

Figure 16 (cont). Draining characteristics for Case 46; $(B, W, r_o, V_o)=(5, 10, 1/10, 8\pi/3)$.

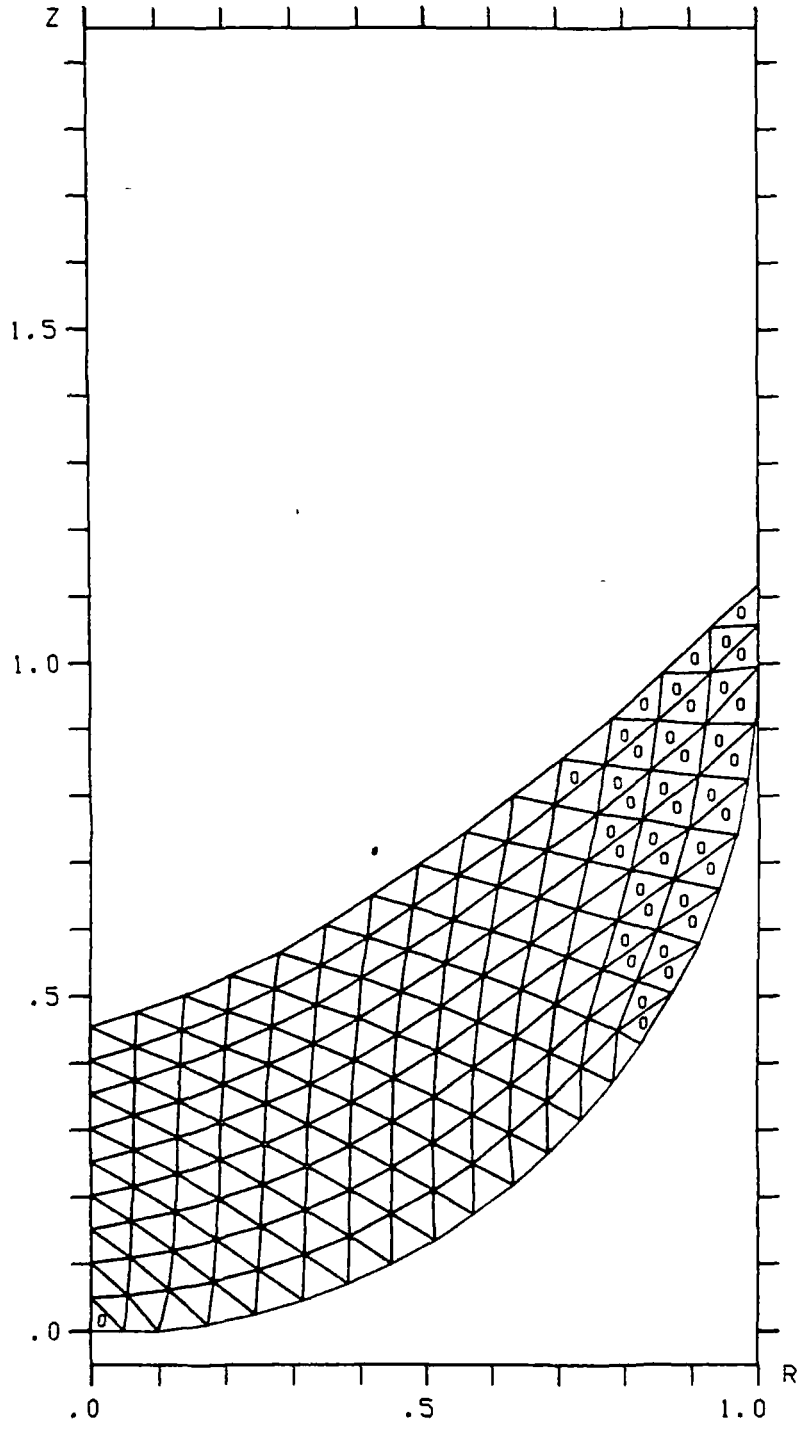

(e) Bottom of mesh at t=1.9411.

Figure 16 (cont). Draining characteristics for Case 46; $(B, W, r_o, V_o) = (5, 10, 1/10, 8\pi/3)$.

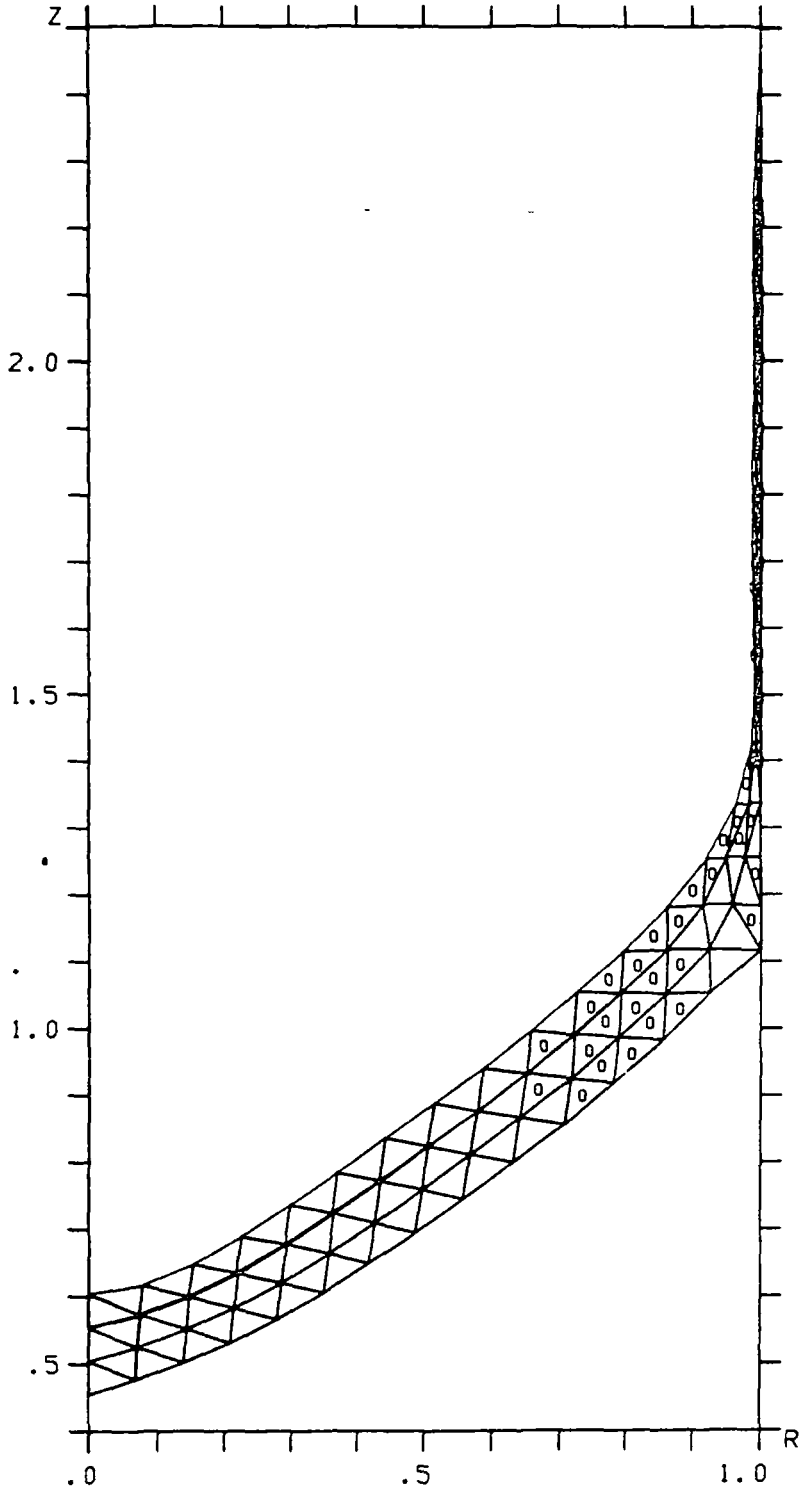

(f) Top of wall sheet at t=1.9411.

Figure 16 (cont). Draining characteristics for Case 46; $(B, W, r_o, V_o)=(5, 10, 1/10, 8\pi/3)$.

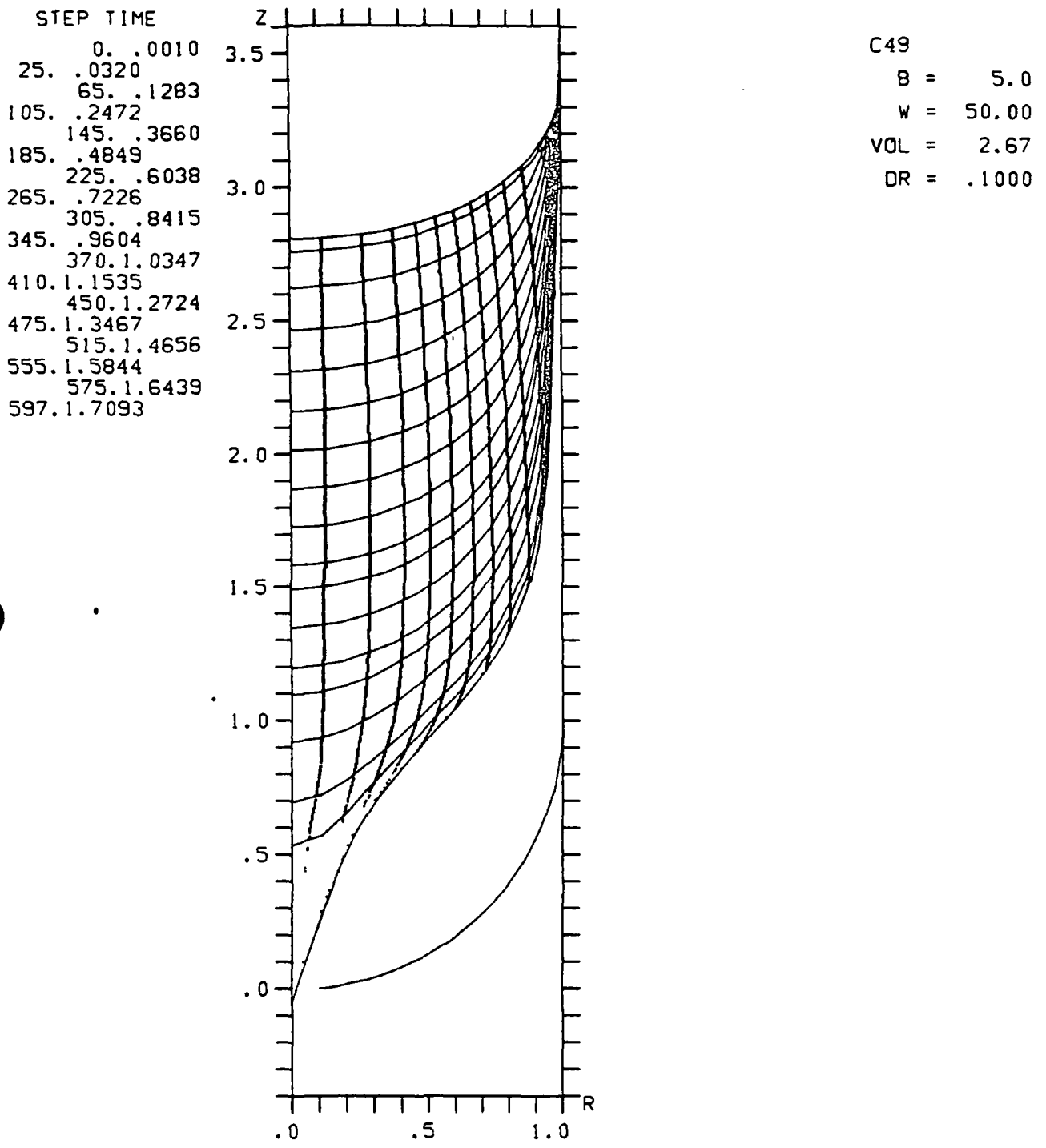

(a) Free surfaces and trajectories of free surface and streamline intersections.

Figure 17. Draining characteristics for Case 49; $(B, W, r_o, V_o)=(5, 50, 1/10, 8\pi/3)$.

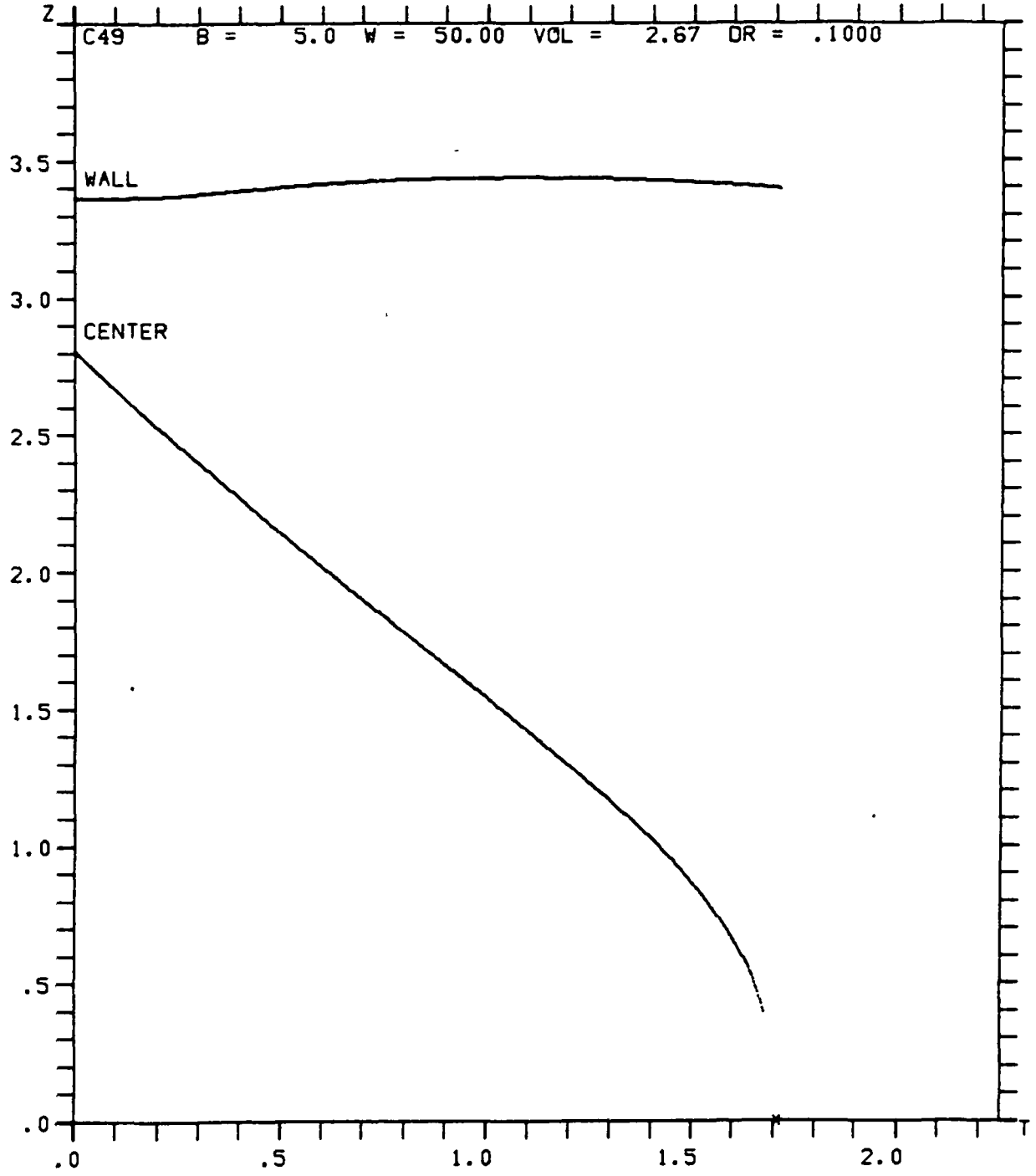

(b) Histories of free surface points at centerline and wall.

Figure 17 (cont). Draining characteristics for Case 49; $(B, W, r_o, V_o)=(5, 50, 1/10, 8\pi/3)$.

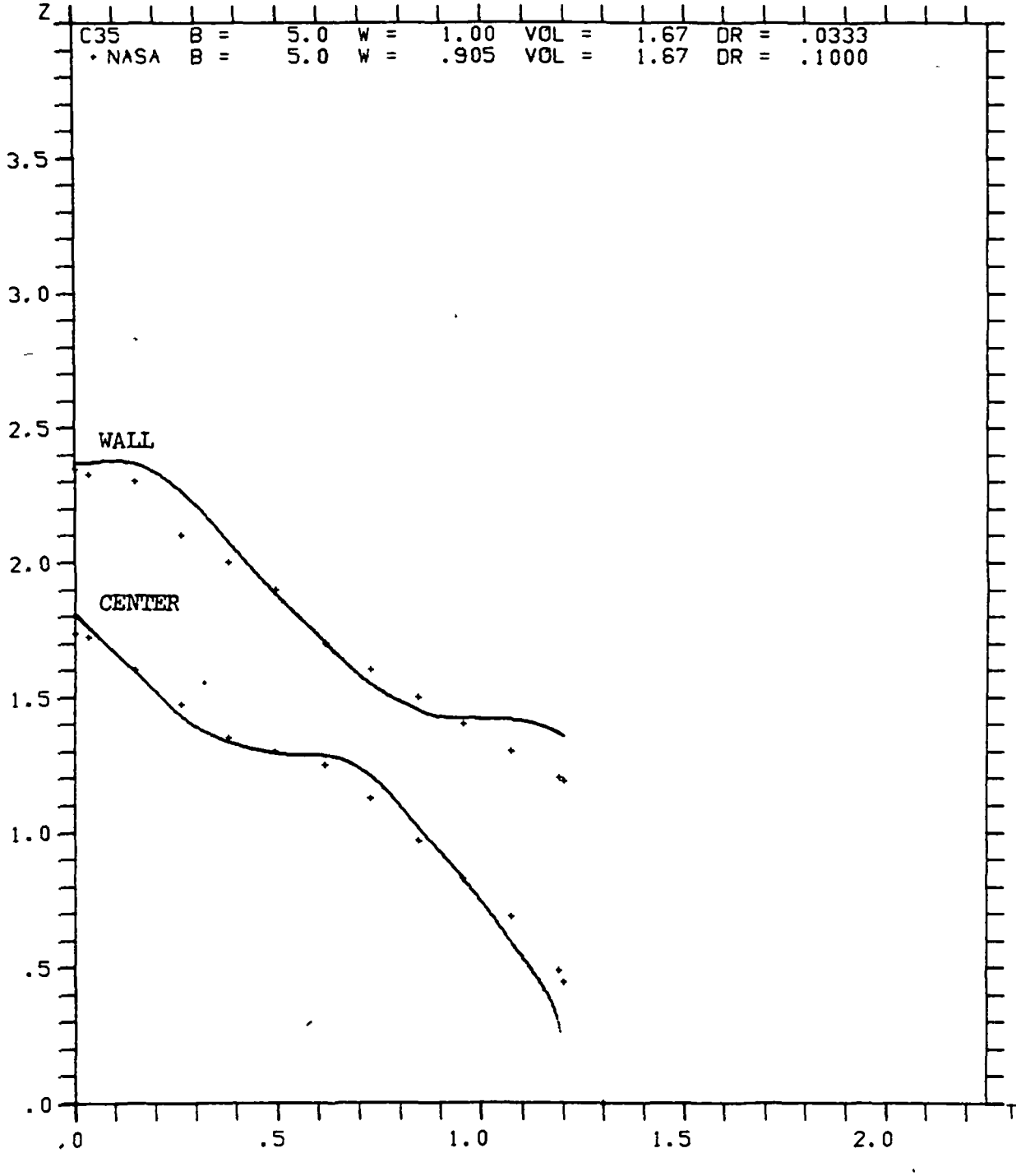

Figure 18. Comparison of computed and experimental data for Case 35; $(B, W, r_o, V_o) = (5, 1, 1/30, 5\pi/3)$.
NASA parameters are $(5.0, .905, .10, 1.67\pi)$.

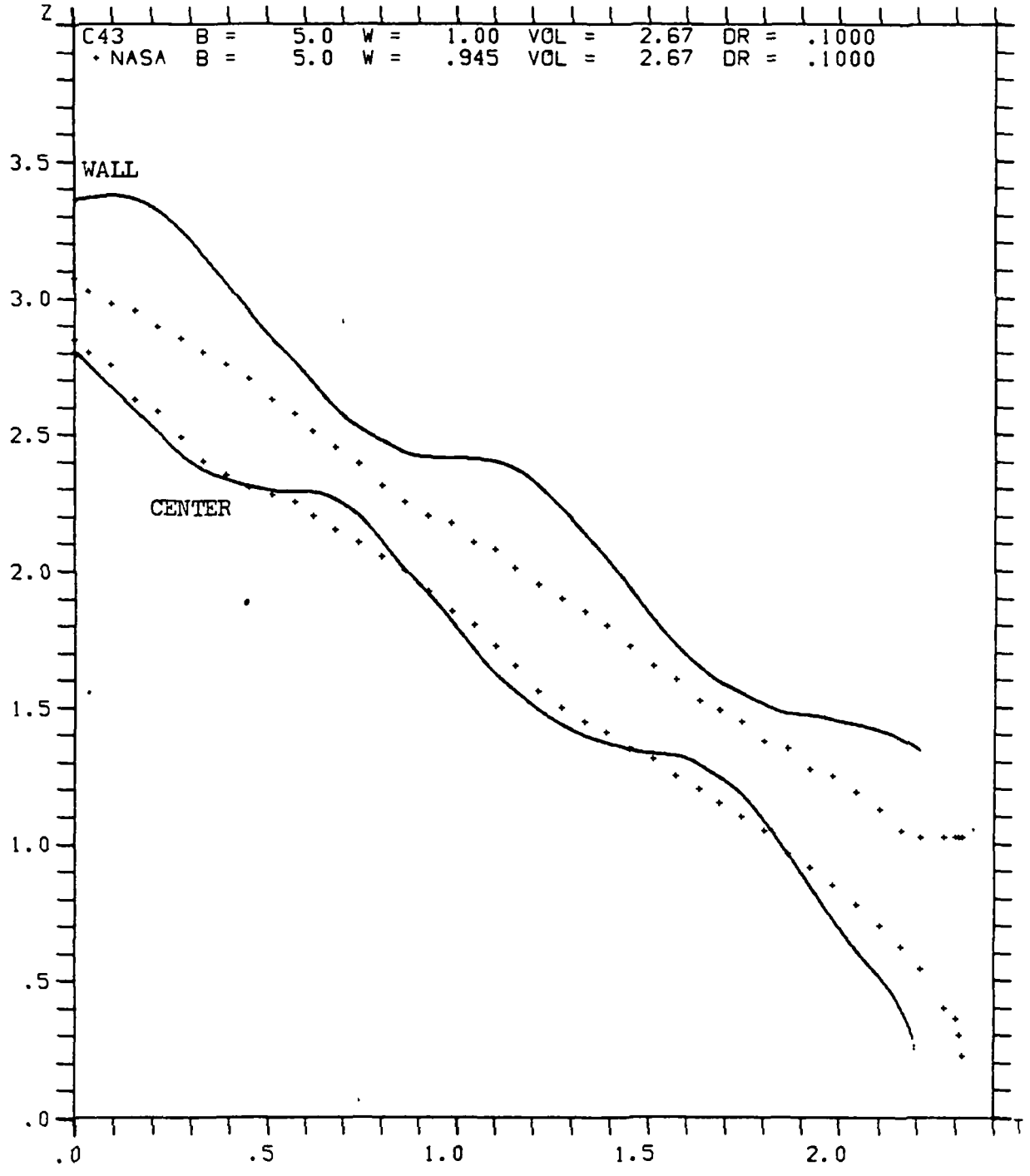

Figure 19. Comparison of computed and experimental data for Case 43; $(B, W, r_o, V_o) = (5, 1, 1/10, 8\pi/3)$.
NASA parameters are $(5.0, .945, .10, 2.67\pi)$.

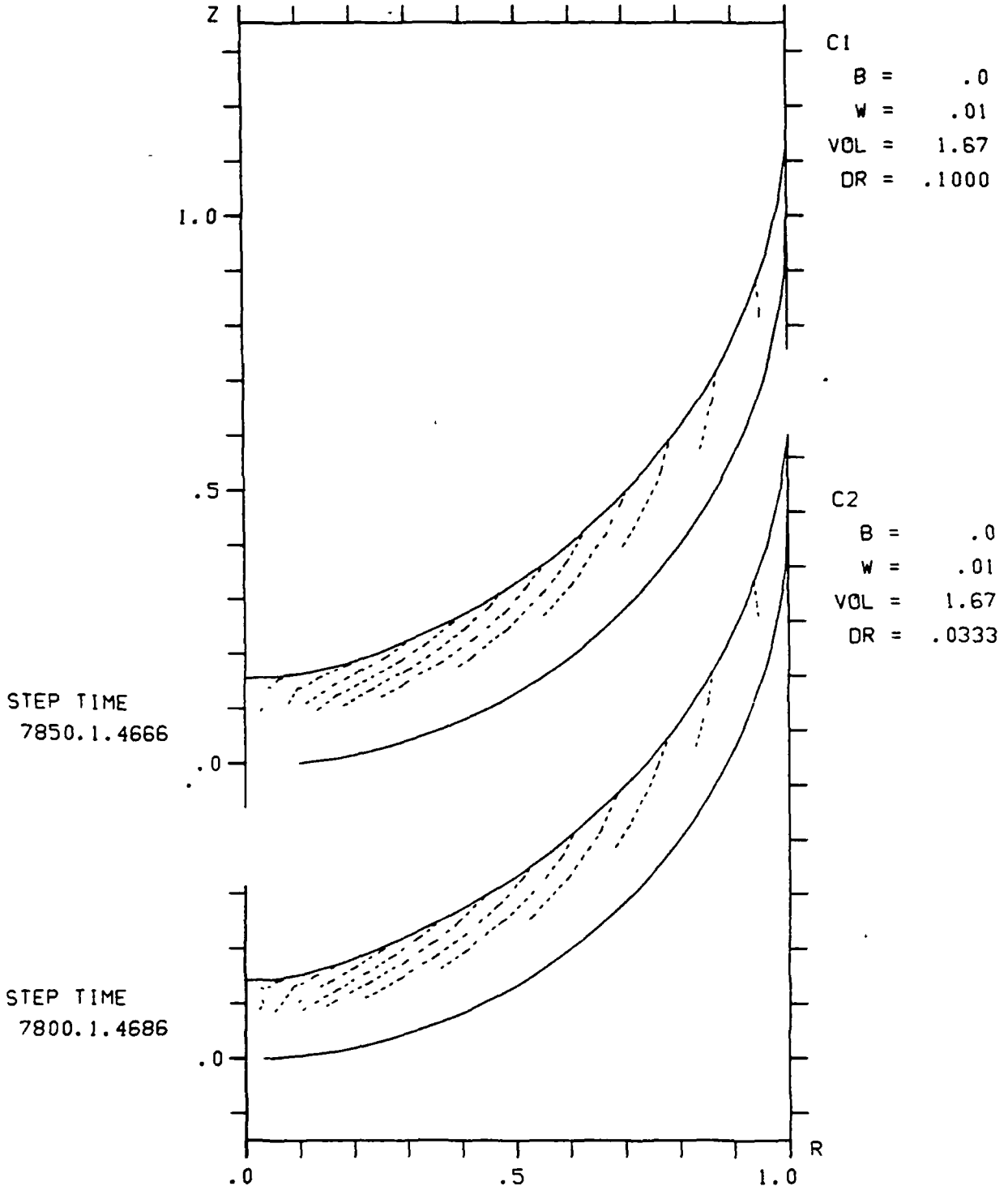

(a) Pattern for r_o=1/10 lies to right of that for r_o=1/30 when free surface is near drain.

Figure 20. Comparison of streamline patterns for large and small drain radii.

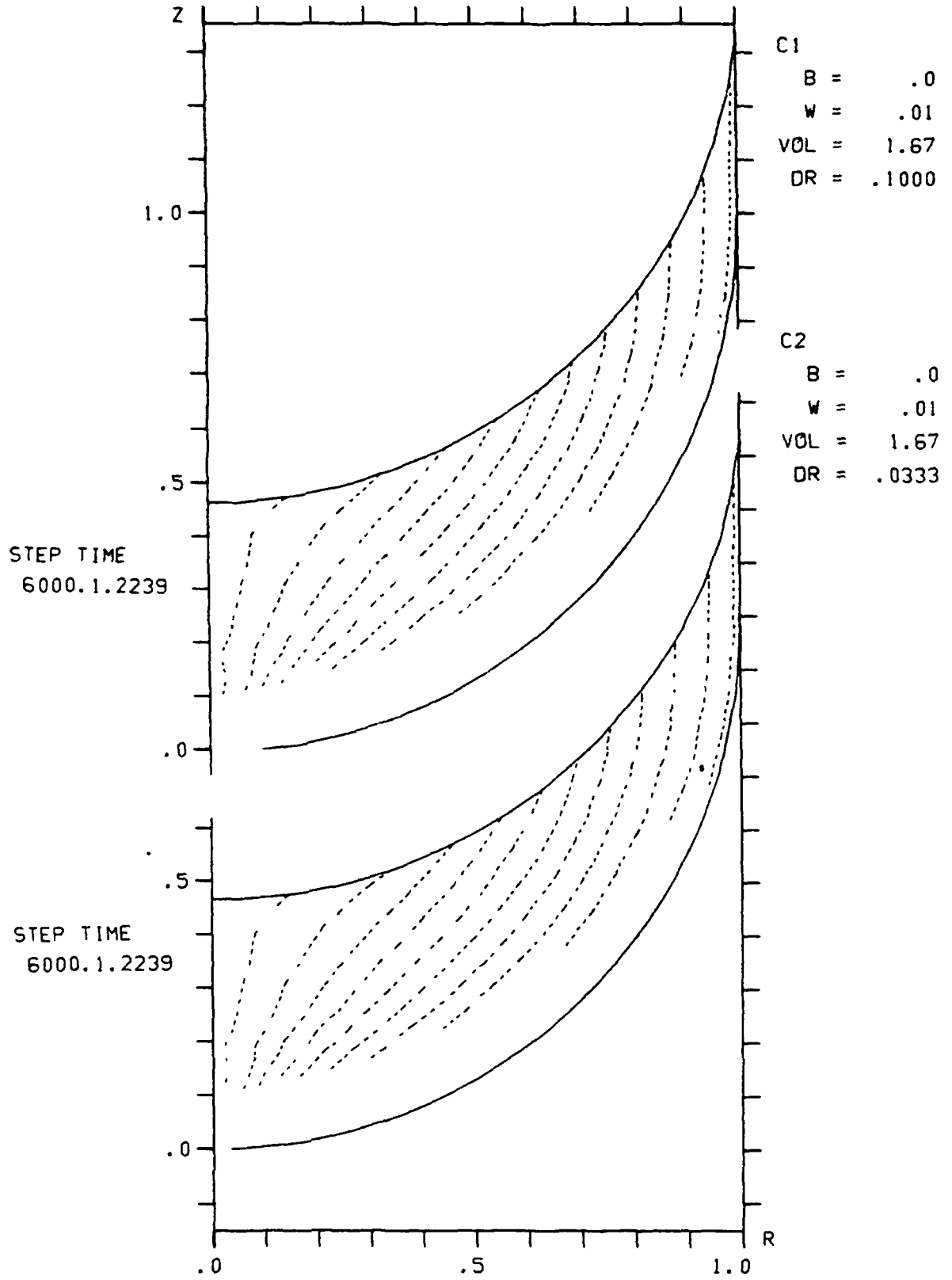

(b) Patterns coincide except near drain when free surface is well above drain.

Figure 20 (cont). Comparison of streamline patterns for large and small drain radii.

TABLE I SUMMARY OF COMPUTED DATA
(All quantities are dimensionless)

Case number	Problem parameters (B, W, r_o, V_o)[a]	Residual volume (V_r)	Vapor ingestion time (t_{vi})	Wall height at vapor ingestion $(h_{w,vi})$
1	$(0, .01, 1/10, 5\pi/3)$	.28752	1.4789	1.131
2	$(0, .01, 1/30, 5\pi/3)$	.29203	1.4761	1.136
5	$(0, .1, 1/30, 5\pi/3)$	.57148	1.2888	1.433
8	$(0, 1, 1/30, 5\pi/3)$	1.00629	.9958	2.653
10	$(0, 10, 1/10, 5\pi/3)$	1.45462	.6967	2.676
19	$(0, 10, 1/10, 8\pi/3)$	1.67175	1.5523	3.856
29	$(5, .01, 1/30, 5\pi/3)$	.11374	1.5919	.614
32	$(5, .1, 1/30, 5\pi/3)$	.24067	1.5097	.798
35	$(5, 1, 1/30, 5\pi/3)$	.70750	1.1989	1.356
37	$(5, 10, 1/10, 5\pi/3)$	1.18648	.8742	2.308
40	$(5, 50, 1/10, 5\pi/3)$	1.25088	.8326	2.430
43	$(5, 1, 1/10, 8\pi/3)$	.70353	2.2053	1.346
46	$(5, 10, 1/10, 8\pi/3)$	.96555	2.0213	2.360
49	$(5, 50, 1/10, 8\pi/3)$	1.44102	1.7063	3.399

[a] (B, W, r_o, V_o) = (Bond number, Weber number, drain radius, initial liquid volume)

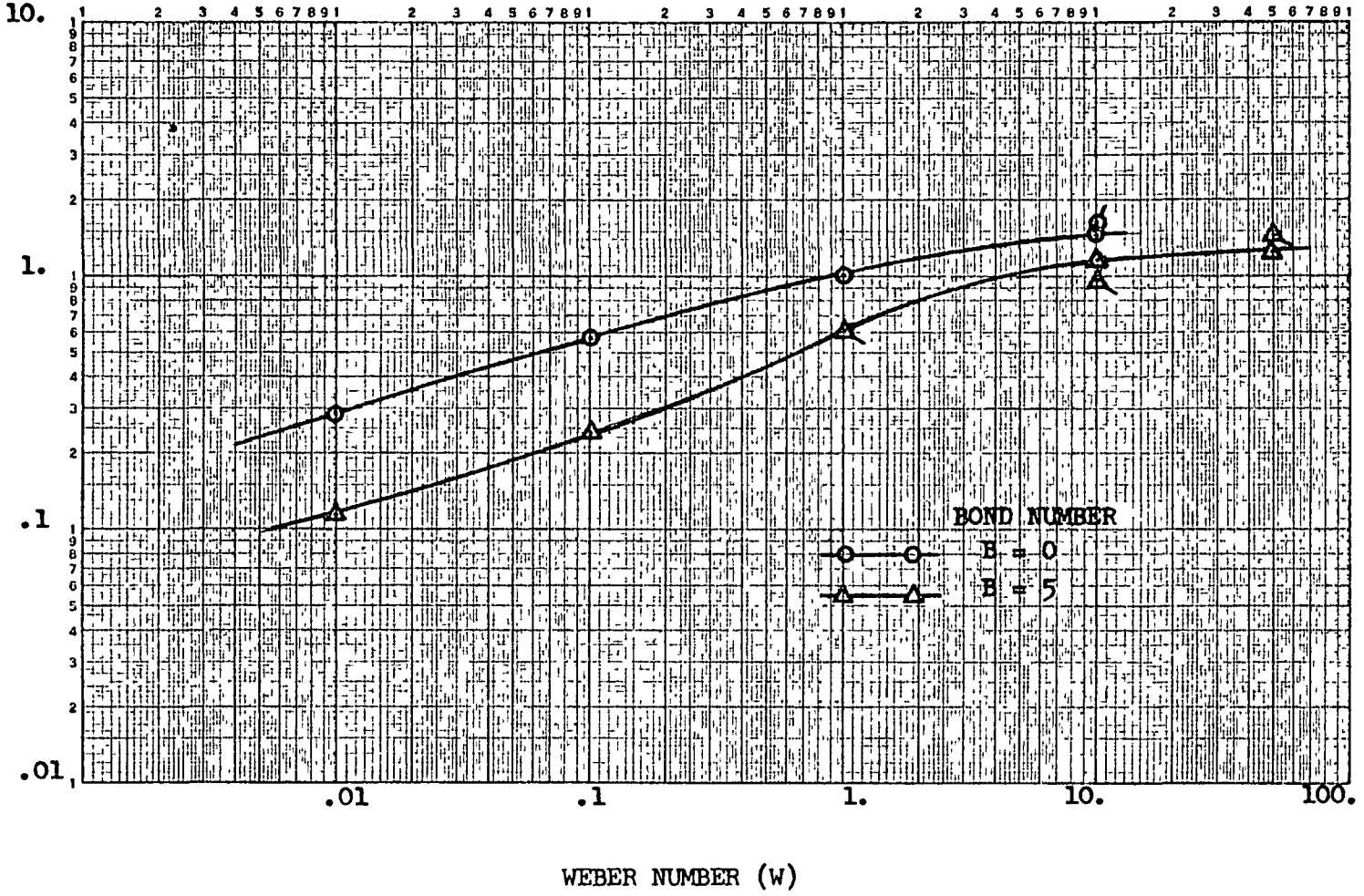

Figure 21. Computed values of residual volume for low gravity draining of hemispherically bottomed, cylindrical tanks. (Data for initial fillings of 5 $\pi/3$; dashed symbols for initial fillings of 8 $\pi/3$.)

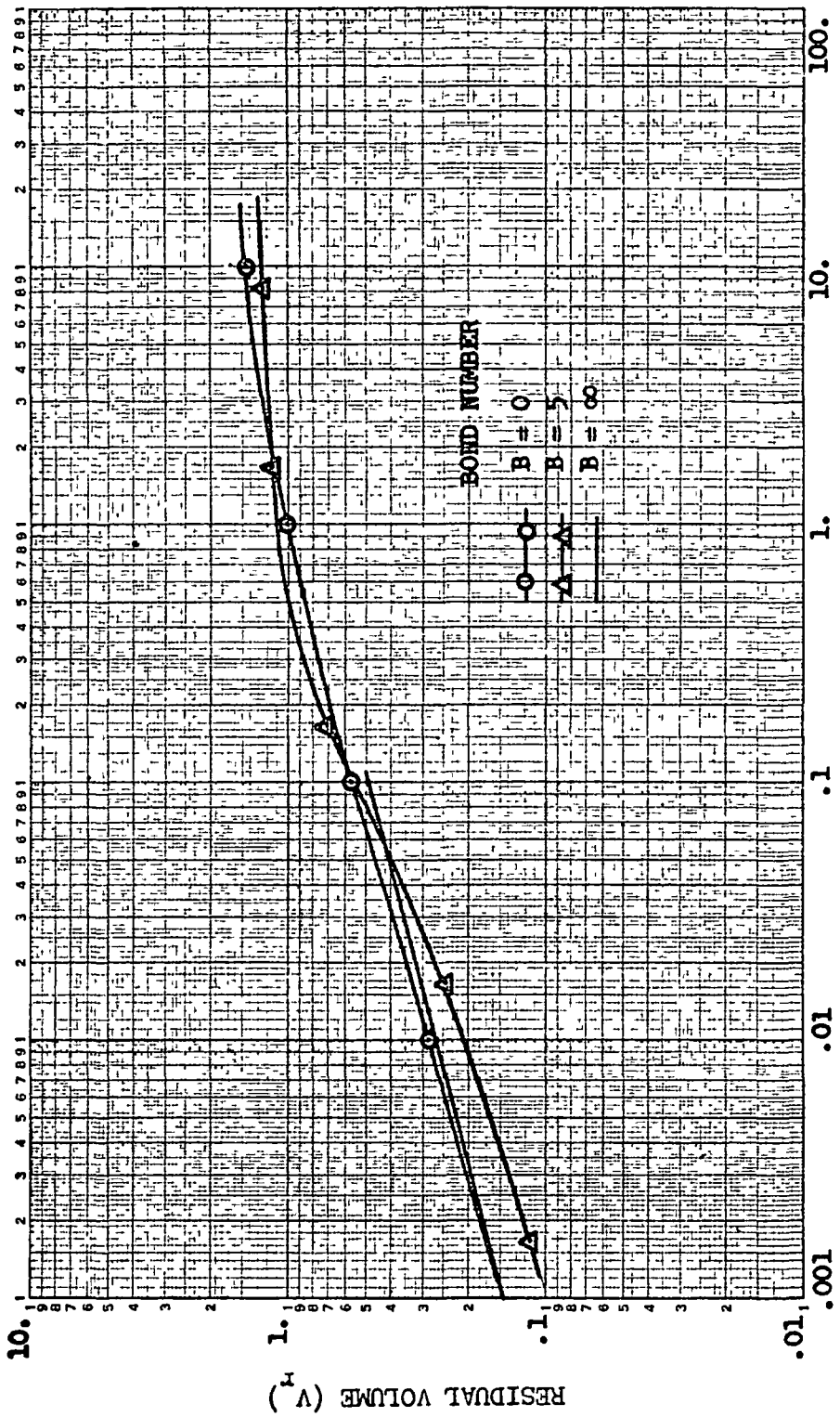

Figure 22. Computed values of residual volumes for low gravity draining of hemispherically bottomed, cylindrical tanks. (Data for $B = \infty$ taken from [2].

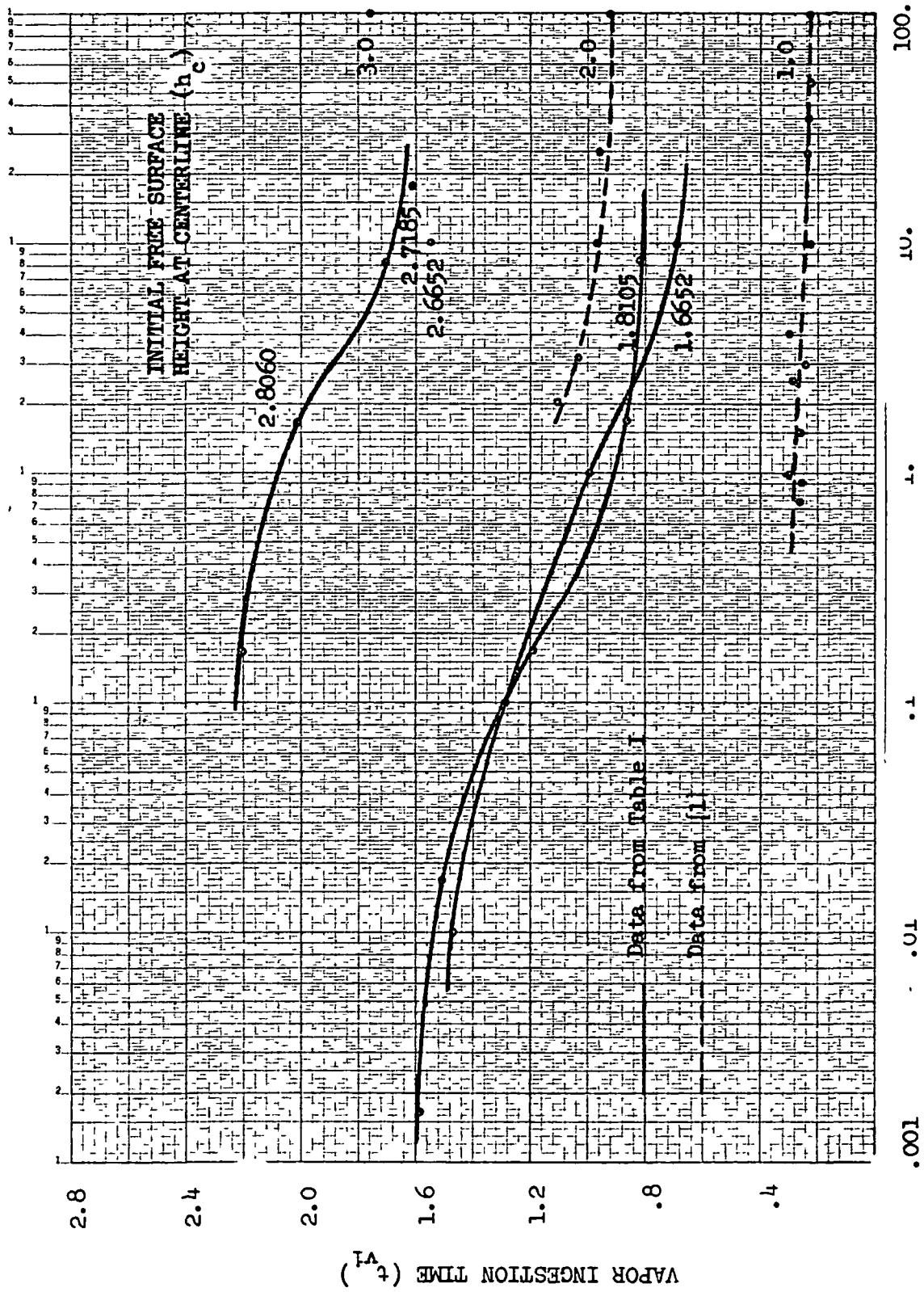

Figure 23. Computed vapor ingestion times for low gravity draining of hemispherically bottomed, cylindrical tanks. (Data for h_c = 1.0, 2.0, 2.6652, 2.7185, and 3.0 taken from [1], Table I.)

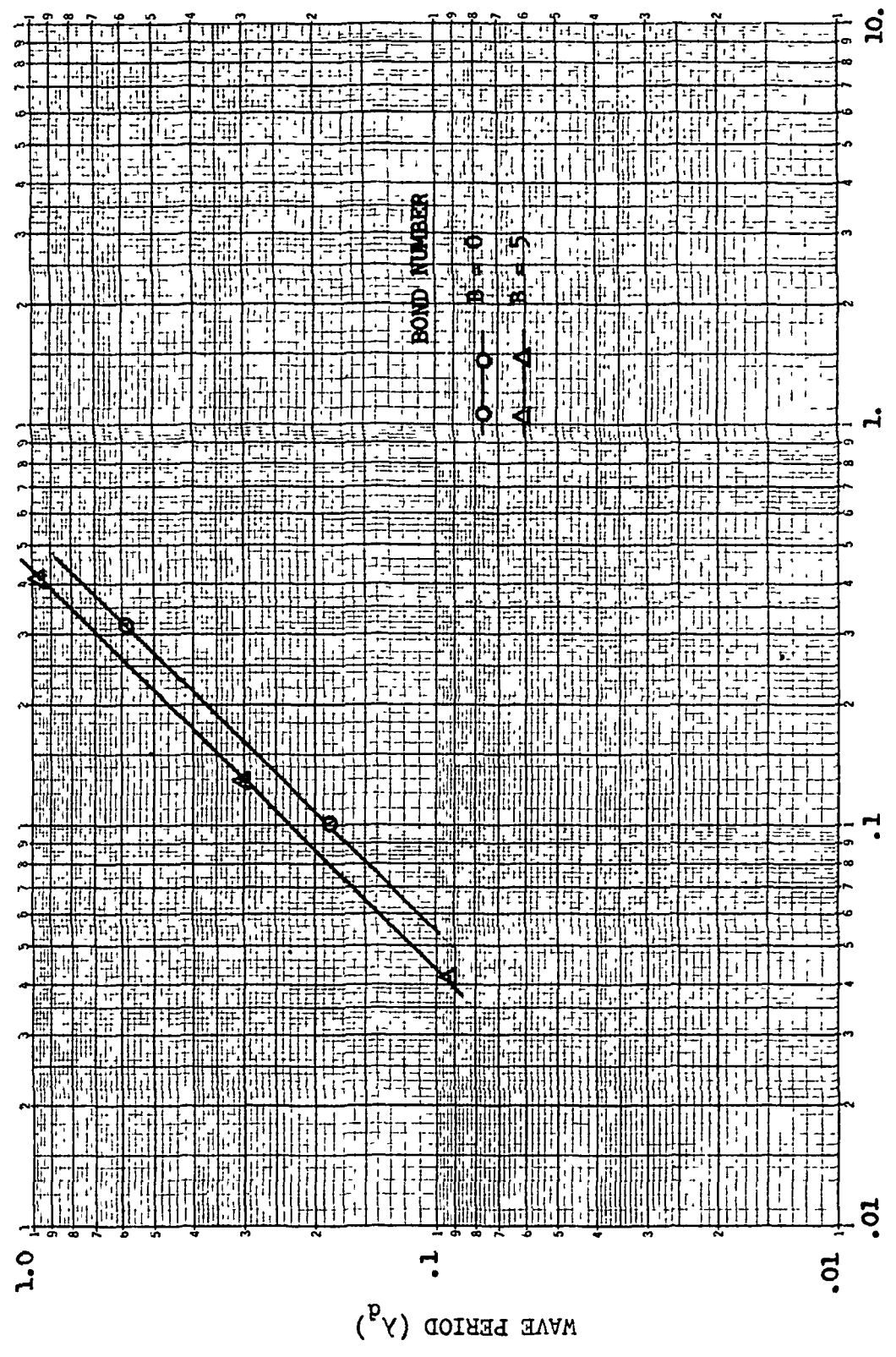

Figure 24. Period of free surface waves produced by draining at low Weber numbers.

TABLE II ESTIMATED WAVE PERIODS
(All quantities are dimensionless)

Case number	Weber number (W)	Bond number (B)	$(W/(1+B))^{\frac{1}{2}}$ [a]	Wave period (λ_d)	Wave period (λ^*) [b]
1	.01	0	.1	.18	1.8
2	.01	0	.1	.18	1.8
5	.1	0	.316	.59	1.9
29	.01	5	.0408	.094	2.3
32	.10	5	.1291	.30	2.4
43	1.	5	.408	.96	2.4

[a] Ratio of sloshing and draining time scales.

[b] $\lambda^* = \lambda_d((1+B)/W)^{\frac{1}{2}}$.

APPENDIX A

SYMBOL LIST

Quantities are nondimensional unless otherwise designated. When appropriate, the relation between a dimensionless variable and the physical dimensional one, which is topped by a bar, is given. Underlined variables are generally vectors. Spatial and temporal variables appearing as subscripts to R, Z, N, S, and φ indicate partial differentiation.

English Alphabet

a	-Dimensional radius of container. The characteristic length with respect to which the variables are made nondimensional.
	-Arbitrary constant.
B	-Bond number = $\rho g a^2/\sigma$.
b	-Arbitrary constant.
c	-Additive constant.
C(t)	-Additive function of time.
DR	-r_o on plotted output.
f	-Height of point on instantaneous free surface meridian = $\bar{f}/a$.
f_w	-Value of f on container wall = $\bar{f}_w/a$.
F	-Height of point on equilibrium free surface meridian = $\bar{F}/a$.
g	-Dimensional acceleration due to gravity.
h_c	-Height of equilibrium free surface at the container axis = $\bar{h}_c/a$.
	-Height of instantaneous free surface at container axis = $\bar{h}_c/a$.

h_w -Height of instantaneous free surface at tank wall = $\bar{h}_w/a$.

$h_{w,vi}$ -Value of h_w at vapor ingestion.

h_o -Thickness of viscous film = $\bar{h}_o/a$.

H -Mean curvature of free surface = $a\bar{H}$.

H_o -Mean curvature of equilibrium free surface at the container axis = $a\bar{H}_o$.

$j_{1,m}$ -m^{th} zero of J_1 .

J_0, J_1 -Bessel functions of first kind.

K -Ratio of nondimensional draining time to nondimensional sloshing time = $\{W/(1 + B)\}^{1/2}$.

m -Summation index.

n -Exterior normal direction.

N -Normal coordinate of point on free surface meridian in local normal-surface coordinates = $\bar{N}/a$.

Q -Dimensional volumetric drain rate.

r -Radial coordinate = $\bar{r}/a$.

r_o -Drain radius = $\bar{r}_o/a$.

r_w -Value of r at intersection of free surface and container wall = $\bar{r}_w/a$.

R -Radial coordinate of point on free surface meridian = $\bar{R}/a$.

-Radial coordinate on computer plots = $\bar{r}/a$.

-Reynolds number = $\rho Q/\pi a\mu$.

s -Arc length along free surface or a mesh line "parallel" to the free surface.

S -Surface coordinate of point on free surface meridian in local normal-surface coordinates = $\bar{S}/a$.

t	-Time = $Q\bar{t}/\pi a^3$ (nondimensional draining time).
T	-Time on computer plots = $Q\bar{t}/\pi a^3$.
t^*	-Time = $\bar{t}\{(1 + B)\sigma/\rho a^3\}^{-1/2}$ (nondimensional sloshing time).
t_{vi}	-Time at vapor ingestion.
u	-Auxiliary velocity in s-direction for mesh control.
U	-Periodic function.
U'	-Derivative of U with respect to time.
v_c	-Velocity along container axis.
v_w	-Velocity along container wall.
$\bar{v}_o$	-Dimensional average bulk speed of liquid = $Q/\pi a^2$.
V	-Liquid volume in tank = $\bar{V}/a^3$.
V_r	-Residual volume measured in hemispherical volumes.
V_s	-Volume of right cylinder of radius 1 below the hemispherical bottom of tank with drain of radius r_o .
V_o .	-Initial liquid volume in tank = $\bar{V}_o/a^3$.
VOL	-Initial tank volume on computer plots = V_o/π .
W	-Weber number = $\rho Q^2/\pi^2 \sigma a^3$.
X	-Generic spatial variable = $\bar{X}/a$.
z	-Axial coordinate = $\bar{z}/a$.
Z	-Axial coordinate of point on free surface meridian = $\bar{Z}/a$.
	-Axial coordinate on computer plot = $\bar{z}/a$.

Greek Alphabet

θ	-Azimuthal angle in right cylindrical coordinates.
Θ	-Contact angle (= 5° for numerical calculations).
λ	-Generic period of wave.

λ_d -Period of wave = $\bar{\lambda}Q/\pi a^3$.

λ^* -Period of wave = $\bar{\lambda}((1 + B)\sigma/\rho a^3)^{1/2}$.

μ -Dimensional liquid viscosity.

ρ -Dimensional liquid density.

σ -Dimensional surface tension.

φ -Velocity potential = $\pi a\ \bar{\varphi}/Q$ (nondimensional draining potential).

φ_1 -Auxiliary velocity potential.

φ_2 -$\varphi_2 = \varphi - \varphi_1$ (residual velocity potential).

φ^* -Velocity potential = $\bar{\varphi}\{(1 + B)\sigma a/\rho\}^{-\frac{1}{2}}$ (nondimensional sloshing potential).

φ_n -Exterior normal derivative of φ .

φ_s -Tangential derivative of φ, positive to left of φ_n .

Miscellaneous

$\underline{\nabla}$ -Gradient operator = $a\underline{\bar{\nabla}}$.

REFERENCES

1. Bizzell, G. D.; Concus, P.; Crane, G. E.; and Satterlee, H. M.: Low Gravity Draining from Hemispherically Bottomed Cylindrical Tanks. LMSC-A903128, Lockheed Missiles and Space Co. (NASA CR-72718), June 1, 1970.

2. Berenyi, Steven G.; and Abdalla, Kaleel L.: Vapor Ingestion Phenomenon in Hemispherically Bottomed Tanks in Normal Gravity and in Weightlessness. NASA TN D-5704, April 1970.

3. Berenyi, Steven G.; and Abdalla, Kallel L.: The Liquid-Vapor Interface During Outflow in Weightlessness. NASA TM X-1811, June 1969.

4. Abdalla, Kaleel L.; and Berenyi, Steven G.: Vapor Ingestion Phenomenon in Weightlessness. NASA TN D-5210, May 1969.

5. Derdul, Joseph D.; Grubb, Lynn S.; and Petrash, Donald A.: Experimental Investigation of Liquid Outflow from Cylindrical Tanks During Weightlessness. NASA TN D-3746, December 1966.

6. Moore, R. E.; and Perko, L. M.: Inviscid Fluid Flow in an Accelerating Cylindrical Container. J. Fluid Mech., vol. 22, part 2, June 1965, pp. 305-320.

7. Symons, Eugene P.: Effect of Throttling on Interface Behavior and Liquid Residuals in Weightlessness. NASA TM X-3034, May 1974.

8. Symons, Eugene P.: Outlet Baffles - Effect on Liquid Residuals from Zero-Gravity Draining of Hemispherically Ended Cylinders. NASA TM X-2631, September 1972.

9. Bradshaw, R. D.; and Kramer, J. L.: An Analytical Study of Reduced-Gravity Propellant Settling. CASD-NAS-74-005, General Dynamics Convair Aerospace Division (NASA CR-134593), February 1974.

10. Saad, Michel A.; and Oliver, David A.: Linearized Time Dependent Free Surface Flow in Rectangular and Cylindrical Tanks. Proceedings of the 1964 Heat Transfer and Fluid Mechanics Institute, Warren H. Giedt and Solomon Levy, editors, Stanford University Press, 1964.

11. Lamb, H.: Hydrodynamics. Dover Publications, New York, N.Y., Sixth Edition, 1932 (Chapter 1, Sec. 11), pp. 10-11.

12. Isaacson, E.; and Keller, H.B.: Analysis of Numerical Methods. John Wiley & Sons, Inc., New York, N.Y., 1966.

13. Winslow, A.M.: Numerical Solution of the Quasilinear Poisson Equation in a Nonuniform Triangle Mesh. J. Comp. Physics, vol. 1, no. 2, November 1966, pp. 149-172.

14. Varga, R. S.: Matrix Iterative Analysis. Prentice-Hall, Inc., Englewood Cliffs, N.J., 1962.

15. Ahlberg, J. H.; Nilson, E. N.; and Walsh, J. L.: The Theory of Splines and Their Applications. Academic Press, New York, N.Y., 1967.

16. Concus, P.; Crane, G. E.; and Satterlee, H. M.: Small Amplitude Lateral Sloshing in Spheroidal Containers under Low Gravitational Conditions. LMSC-A944673, Lockheed Missiles and Space Co. (NASA CR-72500), February 4, 1969.

17. Concus, P.; Crane, G. E.; and Satterlee, H. M.: Small Amplitude Lateral Sloshing in a Cylindrical Tank with a Hemispherical Bottom under Low Gravitational Conditions. LMSC-A852007, Lockheed Missiles and Space Co. (NASA CR-54700), January 20, 1967.

18. Lubin, Barry, T.; and Hurwitz, Matthew: Vapor Pull-Through at a Tank Drain With and Without Dielectrophonetic Baffling. Proceedings of the Conference on Long-Term Cryo-Propellant Storage in Space, NASA Marshall Space Flight Center, Huntsville, Ala., October 1966, pp. 173-180.

19. Lubin, Barry T.; and Springer, George S.: The Formation of a Dip in the Surface of a Liquid Draining from a Tank. J. Fluid Mech., vol. 29, part 2, August 1967, pp. 385-390.

DISTRIBUTION FOR FINAL REPORT

CONTRACT NAS3-17798

Name		No. of Copies
National Aeronautics & Space Administration Lewis Research Center 21000 Brookpark Road Cleveland, Ohio 44135		
Attn:	A. Jones, MS 500-313	1
	E. A. Bourke, MS 500-205	5
	Technical Utilization Office, MS 3-19	1
	Technical Report Control Office, MS 5-5	1
	AFSC Liaison Office, MS 501-3	2
	Library, MS 60-3	2
	Office of Reliability & Quality Assurance, MS 500-211	1
	E. P. Symons, Project Manager, MS 500-204	20
	T. H. Cochran, MS 500-204	1
	J. C. Aydelott, MS 500-204	1
National Aeronautics & Space Administration Headquarters Washington, D. C. 20546		
Attn:	RS/Director, Manned Space Technology	1
	RP/Director, Space Propulsion & Power	1
	RT/Director, Technology Utilization Division	1
	RPI/F. W. Stephenson	1
	RS/P. N. Herr	1
	MIE/H. Schaefer	1
National Aeronautics & Space Administration Goddard Space Flight Center Greenbelt, Maryland 20771		
Attn:	Library	1
National Aeronautics & Space Administration John F. Kennedy Space Center Cocoa Beach, Florida 32931		
Attn:	Library	1
	DD-SED-32/F. S. Howard	1
	DD-SED-4/W. H. Boggs	1

Name	No. of Copies
National Aeronautics & Space Administration Ames Research Center Moffett Field, California 94035	
Attn: Library	1
National Aeronautics & Space Administration Langley Research Center Hampton, Virginia 23365	
Attn: Library	1
C. T. D'Aiutolo, MS 249-A	1
National Aeronautics & Space Administration Johnson Space Center Houston, Texas 77001	
Attn: Library	1
EP2/Z. D. Kirkland	1
EP5/W. Chandler	1
National Aeronautics & Space Administration George C. Marshall Space Flight Center Huntsville, Alabama 35812	
Attn: Library	1
EP 43/L. Hastings	1
EP 43/G. Young	1
EP 45/Dr. Wayne Littles	1
EP 24/K. B. Chandler	1
ES 24/E. W. Urban	1
Jet Propulsion Laboratory 4800 Oak Grove Drive Pasadena, California 91103	
Attn: Library	1
Don Young, MS 125-224	1

Name	No. of Copies
NASA Scientific & Technical Information Facility Post Office Box 8757 Baltimore/Washington International Airport, Maryland 21240	
Attn: Accessioning Department	10
Defense Documentation Center Cameron Station - Bldg. 5 5010 Duke Street Alexandria, Virginia 22314	
Attn: TISIA	1
National Aeronautics & Space Administration Flight Research Center Post Office Box 273 Edwards, California 93523	
Attn: Library	1
Air Force Rocket Propulsion Laboratory Edwards, California 93523	
Attn: LKCC/J. E. Brannigan	1
LKDS/R. L. Wiswell	1
Aeronautical Systems Division Air Force Systems Command Wright Patterson Air Force Base Dayton, Ohio 45433	
Attn: Library	1
Air Force Office of Scientific Research Washington, D. C. 20333	
Attn: Library	1

Name	No. of Copies
Aerospace Corporation 2400 East El Segundo Blvd. Los Angeles, California 90045	
Attn: Library - Documents	1
Arthur D. Little, Inc. 20 Acorn Park Cambridge, Massachusetts 02140	
Attn: Library	1
Beech Aircraft Corporation Boulder Facility Box 631 Boulder, Colorado 80302	
Attn: Library	1
Bell Aerosystems, Inc. Box 1 Buffalo, New York 14240	
Attn: Library	1
L. Thompson	1
Boeing Company Space Division Post Office Box 868 Seattle, Washington 98124	
Attn: Library	1
Chrysler Corporation Space Division Post Office Box 29200 New Orleans, Louisiana 70129	
Attn: Library	1

Name	No. of Copies
McDonnell Douglas Astronautics Co. 5301 Bolsa Avenue Huntington Beach, California 92647	
Attn: Library	1
E. C. Cady	1
General Dynamics/Convair Post Office Box 1128 San Diego, California 92112	
Attn: Library	1
R. Tatro	1
M. Blatt	1
J. Stark	1
Missiles and Space Systems Center General Electric Company Valley Forge Space Technology Center Post Office Box 8555 Philadelphia, Pennsylvania 19101	
Attn: Library	1
Grumman Aircraft Engineering Corporation Bethpage, Long Island, New York	
Attn: Library	1
IIT Research Institute Technology Center Chicago, Illinois 60616	
Attn: Library	1
Lockheed Missiles & Space Company, Inc. Post Office Box 504 Sunnyvale, California 94087	
Attn: Library	1
G. D. Bizzell	1
S. G. DeBrock	1

Name	No. of Copies
Linde, Division of Union Carbide Post Office Box 44 Tonawanda, New York 11450	
Attn: G. Nies	1
Denver Division Martin-Marietta Corporation Post Office Box 179 Denver, Colorado 80201	
Attn: Library	1
D. Fester	1
A. Villars	1
J. Tegart	1
Space Division Rockwell International Corporation 12214 Lakewood Blvd. Downey, California 90242	
Attn: D. Gluck	1
J. Nichols	1
Northrop Space Laboratories 3401 West Broadway Hawthorne, California 90250	
Attn: Library	1
TRW Systems, Inc. 1 Space Park Redondo Beach, California 90278	
Attn: Technical Library Doc. Acquisitions	1
National Science Foundation, Engineering Division 1800 G Street, NW Washington, D. C. 20540	
Attn: Library	1

Name	No. of Copies
Florida Institute of Technology Space Technology Department Melbourne, Florida 32901	
Attn: Dr. T. E. Bowman	1
Heat Transfer & Thermodynamic Laboratory University of Michigan Ann Arbor, Michigan 48107	
Attn: Dr. John A. Clark	1
Dr. Edward B. Igenbergs 8000 Muchen 80 Rauchstrasse 3 Germany	1
Office National D/Etudes Et De Recherches Aerospatiales 29, Avenue de la Division LeClerc 92 Chatillon France .	
Par Jean Maulard	1
Michel Delattre	1
RCA/AED Post Office Box 800 Princeton, New Jersey 08540	
Attn: Mr. Daniel Balzer	1
4043 Cody Road Sherman Oaks, California 91403	
Attn: Dr. Marvin Adelberg	1
Southwest Research Institute Department of Mechanical Sciences Post Office Drawer 28510 San Antonio, Texas 78284	
Attn: H. Norman Abramson	1
Franklin Dodge	1

Name	No. of Copies
Tufts University Mechanical Engineering Department Medford, Massachusetts 02155	
Attn: Dr. Lloyd Trefethen	1